THESIS FOR THE DEGREE OF DOCTOR OF PHILOSOPHY

Protein Stability Across Length and Time Scales

An Investigation of Disaccharides Effect on Protein Structure, Dynamics, and Amyloid Formation

Kajsa Ahlgren

Department of Physics and Astronomy
Division of Nano- Biophysics
Chalmers University of Technology
Gothenburg, Sweden 2026

Protein Stability Across Length and Time Scales
An Investigation of Disaccharides Effect on Protein Structure, Dynamics, and Amyloid Formation

KAJSA AHLGREN
ISBN 978-91-8103-428-8

Acknowledgements, dedications, and similar personal statements in this thesis, reflect the author's own views.

© Kajsa Ahlgren, 2026

Doktorsavhandlingar vid Chalmers tekniska högskola
Ny serie nr. 5885
ISSN 0346-718X
https://doi.org/10.63959/chalmers.dt/5885

Department of Physics and Astronomy
Division of Nano- and Biophysics
Chalmers University of Technology
SE-412 96 Gothenburg, Sweden
Telephone +46 (0)31 772 10 00

Cover: An illustration of a preferentially hydrated protein monomer in solution together with amyloid fibrils.

Chalmers Digitaltryck
Gothenburg, Sweden 2026

Protein Stability Across Length and Time Scales
An Investigation of Disaccharides Effect on Protein Structure, Dynamics, and Amyloid Formation
KAJSA AHLGREN
Department of Physics and Astronomy
Chalmers University of Technology
Gothenburg, Sweden 2026

Abstract

Proteins are fundamental to all living organisms, and their correct folding is vital for many biological processes. A group of diseases collectively known as amyloidosis is characterised by the formation of amyloid fibrils, highly ordered protein aggregates that can accumulate in various tissues. Disaccharides, particularly trehalose, are known to stabilise proteins partly by elevating their denaturation temperature, thereby reducing unfolding and aggregation, yet the underlying mechanisms remain incompletely understood. Improving our understanding of protein misfolding and the role of sugars in inhibiting amyloid fibril formation is therefore of great importance.

This thesis investigates how the disaccharides trehalose and sucrose influence protein stability, dynamics, and aggregation through their interactions with proteins and the surrounding aqueous environment. Neutron and X-ray scattering show that proteins remain preferentially hydrated in the presence of both sugars, with little direct interaction with the surface of the protein. Despite their structural similarity, trehalose reduces the protein dynamics to a greater extent than sucrose, consistent with a more pronounced coupling to the hydration water. Differential scanning calorimetry demonstrates that both disaccharides enhance protein thermal stability by increasing the denaturation temperature.

In addition to stabilisation of the native state, the role of disaccharides in protein aggregation is examined. Small- and wide-angle X-ray scattering show that both trehalose and sucrose suppress aggregation and inhibit the formation of mature fibrils. Amyloid fibrils are commonly described as highly ordered and rigid structures. However, neutron spin echo and dielectric spectroscopy reveal that lysozyme amyloid fibrils retain internal dynamics similar in strength and time scale to those of the native protein, and that these dynamics, as in the monomers, are governed by the surrounding solvent. Furthermore, the fibrils display flexible, polymer-like segmental dynamics in solution, revealing a pronounced multiscale dynamical behaviour, which may be important for understanding their role in neurodegenerative diseases.

Keywords: trehalose, sucrose, myoglobin, lysozyme, amyloid fibrils, protein denaturation, glass transition, neutron scattering, DSC, DS.

List of Publications

I **New insights into the protein stabilizing effects of trehalose by comparing with sucrose**
Kajsa Ahlgren, Christoffer Olsson, Inna Ermilova, and Jan Swenson
Phys. Chem. Chem. Phys., 2023, ***25****, 21215–21226*

II **The nature of trehalose–protein interactions in aqueous solution revealed by neutron scattering**
Kajsa Ahlgren, Christoffer Olsson, Tristan Youngs, and Jan Swenson
Nanoscale, 2026, ***18****, 8609–8621*

III **The inhibition of fibril formation of lysozyme by sucrose and trehalose**
Kajsa Ahlgren, Fritjof Havemeister, Julia Andersson, Elin K. Esbjörner, and Jan Swenson
RSC Advances, 2024, ***14****, 11921–11931*

IV **Comparison of Sucrose and Trehalose for Protein Stabilization Using Differential Scanning Calorimetry**
Olivia Jonsson, Agnes Lundell, John Rosell, Sophie You, Kajsa Ahlgren, Jan Swenson
J. Phys. Chem. B, 2024, ***128****, 20, 4922–4930*

V **Multiscale Dynamics of Lysozyme Amyloid Fibrils Probed by Neutron Spin-Echo and Dielectric Spectroscopy**
Kajsa Ahlgren, Achilleas Pipertzis, Ingo Hoffmann, and Jan Swenson
Submitted and under review at Communications Chemistry

VI **The Effect of Trehalose and Sucrose on the Formation of Amyloid Fibrils of Lysozyme — A Neutron Diffraction Study**
Kajsa Ahlgren, Inna Ermilova, Tristan Youngs, Tom Headen, and Jan Swenson
In Manuscript

Contribution to Papers

I I performed the analysis of the neutron and X-ray scattering data and EPSR modelling together with C.O. I did not perform the molecular dynamics simulations. All authors contributed to the writing of the paper. Shared main author of the publication.

II I performed the analysis of the neutron scattering data and Dissolve modelling. I wrote the first draft of the manuscript.

III I prepared all samples and performed all measurements. I performed the AFM imaging together with F.H. I wrote the first draft of the manuscript.

IV I supervised the project together with J.S. I did not prepare the samples or perform the measurements. All authors contributed to the writing of the paper.

V I prepared all samples. I performed all spectroscopy measurements together with the co-authors. I performed the X-ray diffraction measurements. I performed the AFM imaging together with F.H. I performed the analysis of the neutron spin-echo and X-ray diffraction data as well as processed the AFM images. I did not perform the analysis of the dielectric spectroscopy data. All authors contributed to the writing of the paper.

VI I prepared all samples. I performed all measurements together with the co-authors. I performed the analysis of the neutron diffraction data as well as the Dissolve modelling. I wrote the first draft of the manuscript together with J.S.

Publications not included in the thesis

Lyotropic liquid crystal elastomers for drug delivery
Annija Stepulane, Kajsa Ahlgren, Adrian Rodriguez-Palomo, Anand Kumar Rajasekharan, and Martin Andersson
*Colloids and Surfaces B: Biointerfaces 2023, **226**, 113304*

Declaration of Transparency

This thesis is partially based on the work published in the licentiate thesis ”Sweet Stability – An Investigation of Disaccharides as Protein Stabilisers and Amyloid Fibril Inhibitors” By Kajsa Ahlgren, Chalmers University of Technology, 2024.[1] Chapters have been added and developed to reflect the final results of the project.

Acknowledgements

To Jan Swenson, my supervisor. I would like to extend a big thank you for being such a present and understanding supervisor. Without your guidance and expertise in the subject, this would not have been possible.

I would also like to thank my co-supervisors: Inna Ermilova, for all your help with the simulations and for guiding me through working on the supercomputer; Helén Janson, for your expertise in DSC and DS; Elin Esbjörner, whose insights into proteins and amyloid fibrils have been invaluable.

I would like to thank my examiner Fredrik Höök for the engaging discussions and for your perspective on science.

To Christoffer Olsson, thank you for your generosity, your time, and your willingness to share your expertise over the years. Even though you are not a formal co-supervisor, you certainly acted the part.

I would like to direct a big thanks to my collaborators who have made this thesis possible. I would especially like to thank Fritjof Havemeiser for your help with the AFM measurements and for interesting discussions, and Tristan Youngs for your patience with me during the work with Dissolve and for always helping me when things did not go according to plan.

I would like to thank Julia, for making me laugh during long days in the office and for letting me ventilate. A big thank you to everyone in the biophysics lab, both past and present: Simon, Petteri, Nima, Björn, Julie, Janko, Diana, Nastaran, Mattias, Achilleas, and the many bachelor students who have passed through. You have made the daily rhythm of lab life genuinely enjoyable. Julia, Nima, Achilleas, and Helén deserve a separate thank you for taking on the task of proofreading this thesis. I would also like to thank the lunching women of physics and MC2, Pantea, Mirna, Ariadna, Rebecka, Laura, Adriana, Hanna, Yashna, Erika, Juliette and Finja for all the great conversations and for creating a safe and relatable community.

I would like to express my gratitude to the Swedish research council for their financial support of this project. I am also grateful to Chalmers Materials Analysis Laboratory (CMAL) for providing the SAXS instrument, and to ISIS Pulsed Neutron and Muon Source, STFC Rutherford Appleton Laboratory in UK and Institut Laue-Langevin (ILL) in Grenoble, France, for the allocated beam time. A special thanks goes to the amazing people at these neutron sources for their help and collaboration throughout. Finally, I would also like to thank the National Academic Infrastructure for Supercomputing in Sweden (NAISS) for allocating computational time at the National Supercomputer Center (NSC) Tetralith cluster.

To Emelie, I don't know where to start. Thank you for always being there, ready with insightful wisdom and hysterical laughter in equal measure. Going through this journey with you has made all the difference. To Frida, Johan, Amir, Ale, Sanna, Ester, Sebastian, Sofia, Emil, and all my other friends — thank you for the long evenings, the ridiculous conversations, and for showing up again and again. I honestly don't know what I would do without you.

My deepest thanks go to my parents, my brother Måns and Nicole, for cheering me on at every step and for never letting me doubt that I could do this. I also want to thank my second family in India, the Induchoodan family, for welcoming me with open arms and for all the mangos.

Govin, I could not and would not want to do this without you. No one can make me laugh as much as you. Thank you for being so understanding, patient and caring. Thank you for being you, I love you.

Kajsa Ahlgren

Kajsa Ahlgren

Abbreviations

AFM	Atomic Force Microscopy
CHARMM	Chemistry at HARvard of Molecular Mechanics
DS	Dielectric Spectroscopy
DSC	Differential Scanning Calorimetry
EP	Empirical Potential
EPSR	Empirical Potential Structure Refinement
GAFF	General Amber Force Field
HCl	Hydrochloric acid
HEWL	Hen Egg White Lysozyme
KWW	Kohlrausch-Williams-Watts
LJ	Lennard-Jones
LNCS	Liquid Nitrogen Cooling System
Mb	Myoglobin
MD	Molecular Dynamics
MQ	Milli-Q
NIMROD	Near to Intermediate Range Order Diffractometer
NSE	Neutron Spin Echo
OPLS-AA	Optimised Parameters for Liquid Simulations All Atom
PDB	Protein Data Bank
QENS	Quasielastic Neutron Scattering
RMC	Reverse Monte Carlo
RP	Reference Potential
SAXS	Small-Angle X-ray Scattering
WAXS	Wide-Angle X-ray Scattering

Contents

List of Figures

1

Introduction

It was 170 years ago that the term amyloid was coined.[2] A term that much later became highly associated with what is now the most prevalent neurodegenerative disease worldwide, Alzheimer's disease.[3] In 2020, approximately 50 million individuals were reported to be living with Alzheimer's disease globally.[4] The first documented case was described in the early 1900s by Alois Alzheimer, after whom the disease later got its name.[2] Since then, extensive research has revealed that Alzheimer's disease is related to the formation of long thread-like protein aggregates in the brain known as amyloid fibrils.[5,6] Importantly, amyloid fibrils are not exclusively associated with Alzheimer's disease but are part of a broader group of amyloid-related disorders, all characterised by the formation of amyloid fibrils from distinct precursor proteins.[7–9] More generally, amyloid fibrils are implicated in a wide range of pathological conditions collectively referred to as amyloidoses.[10] The formation of amyloid fibrils typically requires proteins to adopt unfolded or partially unfolded conformations, which expose aggregation-prone regions that are otherwise buried in the native state. Stabilising the native structure of the protein can reduce the population of such aggregation-competent intermediates and thereby inhibit amyloid formation.

Since neurodegenerative diseases, such as Alzheimer's, are associated with protein folding and misfolding, numerous studies have investigated the stabilisation of the native fold across a wide range of proteins, employing various experimental approaches and stabilising agents,[11–14] one of which is the disaccharide trehalose. Trehalose occurs naturally in a variety of organisms capable of surviving conditions typically considered lethal, including severe desiccation and extreme temperature stress.[15–18] One such organism is the microscopic water-living animal known as the tardigrade, named for its slow-moving pace.[19] Tardigrades are tiny animals first described 250 years ago by the German zoologist Goeze.[19,20] They are well known for their extraordinary ability to survive in extreme conditions, including desiccation and freezing.[21]

With nature as inspiration, trehalose has been employed as a stabilising agent in several biopharmaceuticals such as the antibody-based cancer treatments Herceptin® and

Avastin®.[22] Biopharmaceuticals are medical drugs derived from biological sources such as cells, tissues or microorganisms. They are usually formulated in liquid form, in which proteins and other biomolecules are prone to aggregation and chemical degradation at ambient temperatures.[23] Such formulations therefore require cold-chain storage, which is logistically demanding and costly. One strategy to circumvent this is freezing or freeze-drying. However, a central challenge is the management of ice formation, which can damage biomolecules through multiple mechanisms: ice crystals cause mechanical damage, and the rising solute concentration in the unfrozen fraction induces osmotic stress, both of which can force biomolecules into non-native, inactive conformations.[24] Despite this, research has shown that freeze-drying biopharmaceuticals with trehalose as a cryoprotectant enables stable storage at ambient temperatures, removing the need for cold-chain storage.[25–28] In addition to pharmaceutical applications, trehalose is also used in food and cosmetics to enhance product shelf life.[22]

The stabilising effect of trehalose on proteins and other biomolecules is a remarkable property that remains incompletely understood, and has consequently been the subject of extensive study over the past few decades.[17,22,29–36] Efforts to elucidate the underlying mechanism have increasingly focused on its physicochemical characteristics. In particular, trehalose has been reported to be an excellent glass former, exhibiting higher glass transition temperature than other common disaccharides.[37–39] This property motivated the formulation of the *vitrification hypothesis*, first proposed by Green and Angell,[31] which suggests that during drying, trehalose and the associated biomolecule enter a glassy state that stabilises the biomolecule by suppressing molecular mobility. However, comparative studies have shown that trehalose can provide superior bioprotection relative to other glass formers, including some with higher glass transition temperatures.[37,38] These findings indicate that, although vitrification contributes significantly to stabilisation, the glass forming ability of trehalose alone does not fully account for its protective effects.[37] In 1984, Crowe et al.[30] proposed that trehalose stabilises membranes by forming hydrogen bonds with the head groups of phospholipids, thereby replacing the hydrogen bonds normally formed between the phosphate groups and water. This hypothesis later became known as the *water replacement model.* In 1998, this conceptual framework was extended to protein stabilisation during drying, suggesting that trehalose can form hydrogen bonds with polar residues and substitute for water–protein interactions.[37] The water replacement model was primarily suggested for systems with low water content. However, this model was challenged in 1994, by Belton and Gil,[40] who suggested that trehalose concentrates and traps water molecules close to the surface of the protein by the formation of a cage of trehalose molecules. Additional studies have been conducted with the purpose of understanding the stabilising properties of disaccharides.[41–45] These studies observed protein-water-sugar structures in systems at low water content, which supports the *water entrapment model.* Arakawa and Timasheff[29,46] proposed an alternative mechanism for more diluted systems, in which a layer of hydration water surrounding the protein is essential for stabilisation. This framework later became known as the *preferential hydration model* and has since then received substantial support in research.[33, 40, 45, 47–50] Similarly to the water entrapment model, the protein remains preferentially hydrated by water molecules. However, co-solutes such as trehalose are suggested to be excluded from the immediate protein surface. The preferential hydration model have been suggested also for diluted protein systems. Additional support for the preferential hydration model can be found in papers I,[51] II,[52] IV[53] and VI included in this thesis.

This thesis aims to investigate protein stability and how it is influenced by the presence of disaccharides, specifically trehalose and sucrose, across different time and length scales. It further seeks to clarify the broad concept of protein stabilisation and to elucidate the relationship between structural organisation and molecular dynamics. The research involves a combination of experimental and computational approaches to characterise the structure and dynamics of systems containing either native or fibrillated proteins, and to observe how these properties are affected by the presence of disaccharides.

1.1 Structure of the Thesis

The structure of the thesis is as follows.

1.1.1 Chapter 2: Background

This chapter includes a theoretical background of the materials used. Initially, the structure and properties of liquids and amorphous materials are described more generally, followed by a more detailed description of the different molecules included in the investigated systems. In this chapter the definition of protein stability and how its connection the dynamics is also included.

1.1.2 Chapter 3: Theory of Experimental Methods

This chapter provides essential theory concerning the experimental techniques used to characterise the structure and dynamics of the investigated systems. In addition, a description of the structural modelling and simulation methods is also included in this chapter.

1.1.3 Chapter 4: Sample Preparations

The preparation of the different samples that were analysed in each paper is presented in this chapter.

1.1.4 Chapter 5: Summary of Results

This thesis is based on the work presented in six papers that collectively investigate the thermodynamic and dynamic stability of proteins and how it is affected by the presence of disaccharides. Chapter 5 includes a summary of the results in the appended papers.

1.1.5 Chapter 6: Conclusion and Future Perspectives

The final chapter concludes the thesis with a reflection on the appended results and an outlook on future research.

2

Background

2.1 Liquids and Amorphous Materials

Liquids and amorphous materials are examples of physical forms that lack any form of long range order.[54] The only physical form in which the molecules are neatly arranged in a repeating pattern is the crystalline state. If one only considers the ordering of molecules, one could say that liquids and amorphous solids are the same. However, one important difference is the viscosity of the material, where the viscosity of a liquid is low and that of an amorphous solid is high. Despite the lack of long range order, certain amorphous materials contain short-range periodicity.[54] This thesis includes studies of both liquid and amorphous materials as well as the transition from liquid to glass which will be described in the following section.

2.1.1 The Transition from Liquid to Glass

When a liquid is cooled, its viscosity typically increases, a phenomenon largely due to a decrease in the kinetic motion of the individual particles and an increase in density. When a material is cooled below its point of freezing, it becomes more energetically favourable for the particles to form structured lattices; this phenomenon is known as crystals. The crystallisation event is characterised in Figure 2.1 as an abrupt drop in volume at the point of the melting temperature, T_m. The crystallisation is a first-order phase transition. When a liquid is cooled below its T_m, there is another possible outcome; the liquid can become supercooled, leading to an increase in viscosity as the temperature decreases, eventually resulting in the formation of a glass.[55] A glass is an amorphous solid which exhibits glass transition. As oppose to crystallisation, the glass transition can be considered as a second-order phase transition. This means that no heat is transferred between the sample and its surroundings. However, there is a change in heat capacity. By monitoring the volume of a liquid as a function of temperature, as in Figure 2.1, the phase transitions can easily be displayed.

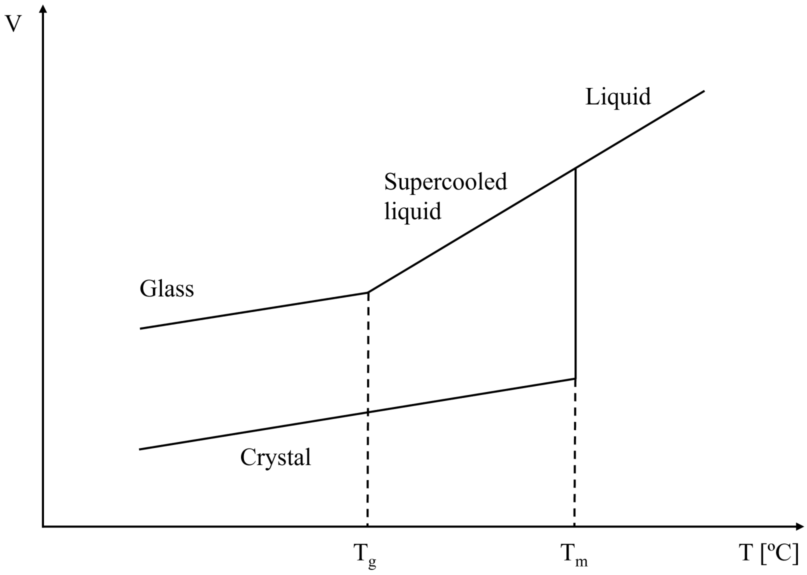

Figure 2.1: Illustration of how the volume of a substance varies with temperature during phase transitions from liquid to crystal or glass.

For the supercooled liquid, the volume is decreased linearly until a point where the slope changes and a glass is formed. This is commonly referred to as the glass transition and the temperature at which it occurs is called the glass transition temperature, T_{g}. The different phases are highly dependent on the cooling rate, where a slower rate enables the liquid to stay supercooled longer, resulting in a lower T_{g}. Thus, the T_{g} partly depends on the thermal history of the material[55] and therefore it is not a true second-order thermodynamic phase transition. A convenient way to measure the glass transition event is via differential scanning calorimetry (DSC), which will be presented in more detail in section 3.3. The thermal events are then detected as changes in heat flow as the temperature is varied.

2.1.2 Structure of Liquids and Glasses

The most common and simple way to characterise the structure of liquids and glasses is through the pair correlation function, $g(\mathbf{r})$[a], which provides a statistical description of the local packing and particle density of the system. A complete structural description of any material requires a hierarchy of correlation functions, ranging from the one-body correlation function (which describes the local density) to many-body correlations involving all atoms. For crystalline materials, the one-body correlation function is well-defined and varies periodically, reflecting the ordered atomic arrangement. In

---

[a] The pair correlation function is sometimes referred to as the radial distribution function or the pair distribution function. However, these terms are not strictly equivalent. The radial distribution function, $g(r)$, is obtained by averaging the pair correlation function, $g(\mathbf{r})$, over all directions: $g(r) = \langle g(\mathbf{r})\rangle_{\Omega}$[56]

contrast, for liquids and glasses, the one-body correlation function is featureless and flat since atoms can occupy any position with equal probability. Consequently, the first meaningful correlation function for liquids and glasses is the two-body (pair) correlation function, which describes how the position of one atom correlates with another as a function of their separation.[57] Figure 2.2 shows a schematic illustration of the pair correlation function in a liquid. At short distances the pair correlation function is zero since atoms cannot overlap; it becomes non-zero at larger separations. Sharp peaks in $g(\mathbf{r})$ indicate strong atomic bonding at specific distances, whereas weak, slowly-varying behaviour indicates repulsive interactions between atoms. This pair correlation function can be directly probed by neutron and X-ray diffraction experiments, making them the primary experimental tools for characterising liquid and amorphous structures.

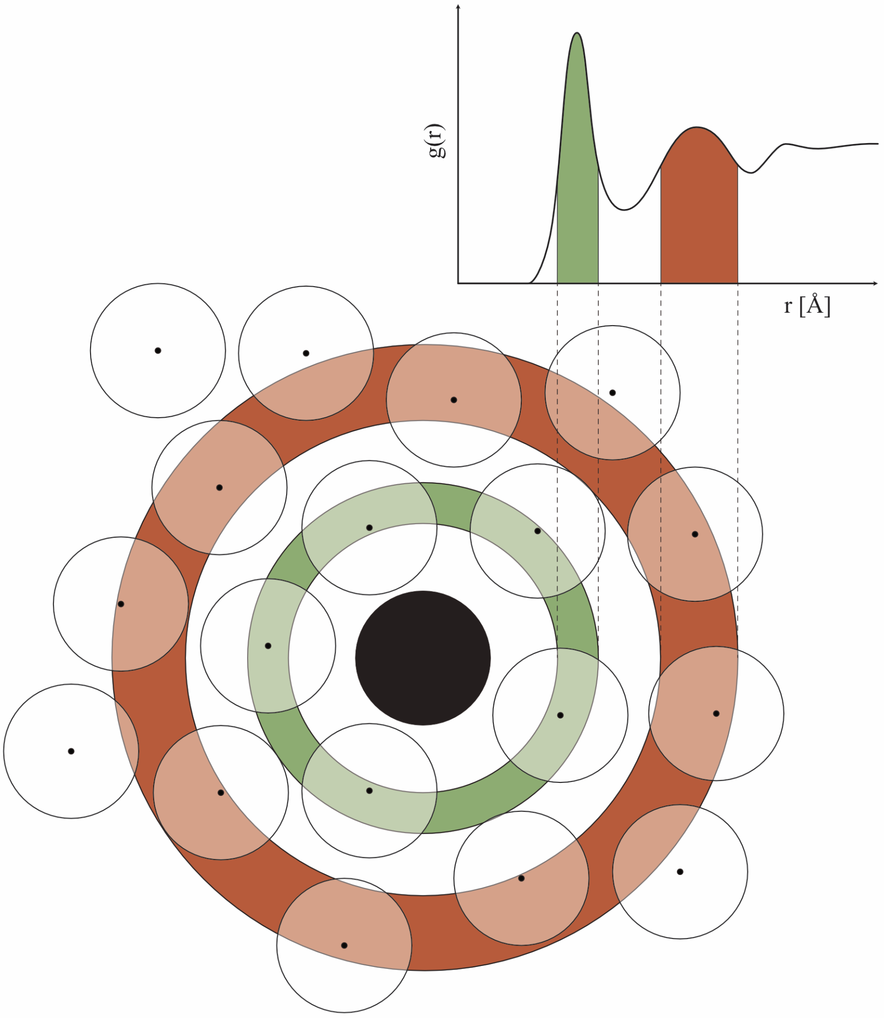

Figure 2.2: Schematic illustration of the pair correlation function. The black circle represents the an atom at position i and the surrounding white circles adjacent atoms. The green and red area around the centre atom correspond to the area of the first and second coordination shells.

The derivation of the pair correlation function can be found in several textbooks and for more details the reader is referred to Refs. 58–60. To derive the pair correlation function, we begin with the local number density in an amorphous material

$$\rho(\mathbf{r},t) = \sum_{i=1}^{N} \delta(\mathbf{r} - \mathbf{r}_i(t)), \tag{2.1}$$

where $\mathbf{r}_i(t)$ is the position of atom i at time t and N is the number of particles. The pair correlation function can be obtained by performing an autocorrelation of this density distribution:

$$G(\mathbf{r},t) = \frac{1}{N}\int \rho(\mathbf{r},t)\rho(0,0)d\mathbf{r} = \frac{1}{N}\sum_{ij}^{N} \delta(\mathbf{r} + \mathbf{r}_j(0) - \mathbf{r}_i(t)). \tag{2.2}$$

Distinguishing between the self-correlation ($i = j$) and distinct-pair correlation ($i \neq j$), allows us to rewrite Equation (2.2) as

$$G(\mathbf{r},t) = \delta(\mathbf{r},t) + \frac{1}{N}\sum_{i\neq j}^{N} \delta(\mathbf{r} + \mathbf{r}_j(0) - \mathbf{r}_i(t)) = \delta(\mathbf{r},t) + \rho g(\mathbf{r},t), \tag{2.3}$$

where ρ is the average number density. The first term describes an atom's correlations with itself, while the second term describes correlations between distinct atoms. At $t = 0$:

$$G(\mathbf{r},0) = \delta(\mathbf{r}) + \rho g(\mathbf{r}), \tag{2.4}$$

the self-correlation function becomes the Dirac delta function, $\delta(\mathbf{r})$.

The pair correlation function quantifies the local atomic environment. Integration of $4\pi\rho g(r)r^2dr$ up to the first minimum of $g(r)$ yields the coordination number, which represents the average number of nearest neighbours surrounding a particle and provides information on the spatial distribution of one atom relative to one another.

Until now, only the spatial distribution of the atoms has been considered. However, to understand the dynamics, it is often useful to include the displacements of time, which is done in the dynamic pair correlation function, referred to as the van Hove function:[61]

$$G(\mathbf{r},t) = \frac{1}{N}\sum_{i,j}^{N} \delta(\mathbf{r} + \mathbf{r}_i(0) - \mathbf{r}_j(t)). \tag{2.5}$$

Similarly to the static case, $G(\mathbf{r},t)$ can be interpreted as the probability density to find a particle i at position $\mathbf{r}$ at time t, and it is assumed that particle j is at the origin at $t = 0$.[62] By distinguishing between the cases $i = j$ and $i \neq j$, Equation (2.5) can be separated into $G(\mathbf{r},t) = G_\mathrm{s}(\mathbf{r},t) + G_\mathrm{d}(\mathbf{r},t)$, where

$$G_{\mathrm{s}}(\mathbf{r},t) = \frac{1}{N}\sum_{i}^{N}\delta(\mathbf{r}+\mathbf{r}_i(0)-\mathbf{r}_i(t)) \tag{2.6}$$

and

$$G_{\mathrm{d}}(\mathbf{r},t) = \frac{1}{N}\sum_{i,j\neq i}^{N}\delta(\mathbf{r}+\mathbf{r}_i(0)-\mathbf{r}_j(t)), \tag{2.7}$$

correspond to the self-correlation, and the distinct part, respectively. The self-correlation and distinct-correlation part can be interpreted as the probability density of finding a particle i and $j \neq i$, respectively, at time t with the assumption that the particle i was at the origin at $t = 0$.[62]

2.2 Water

Water is a fundamental component of our planet, essential to all known forms of life. It is therefore understandable that a great number of studies have focused on understanding its properties at the molecular level.[63–68] To appreciate these properties, it is helpful to first recall the molecular structure of water, which consists of one oxygen and two hydrogen atoms forming a bent geometry with an angle of 105°.[69] This specific arrangement arises from the fact that oxygen and hydrogen differ significantly in their electronegativity; oxygen has an electronegativity value of 3.5,[69] while that of hydrogen is considerably lower at 2.1.[69] Electronegativity refers to an element's tendency to attract electrons. Because oxygen is more electronegative than hydrogen, it draws electron density away from the hydrogen atoms, resulting in an uneven distribution of electrical charge within the molecule. As a result, the oxygen carries a partial negative charge and the hydrogens a partial positive charge. This uneven charge distribution, combined with the bent geometry of the molecule, makes water a permanent dipole.

The difference in charge makes the water molecule a great subject to form hydrogen bonds. Hydrogen bonds are formed when covalently linked hydrogen atoms are attracted by an electronegative atom of a different molecule, in this case oxygen. In water, each molecule acts both as an acceptor (A) and a donor (D), enabling intermolecular hydrogen bonding.

At temperatures above the boiling point of water (100°C), water molecules exist as gas (water vapour). In this gaseous state, the molecules move rapidly, preventing the formation of intermolecular hydrogen bonds. As the temperature decreases, the water molecules slow down and transition into a liquid phase, allowing oxygen in one water molecule to form a hydrogen bond with a hydrogen atom in another molecule. However, in this liquid state, due to thermal fluctuation, the water molecules continuously translate and rotate, leading to the breaking of hydrogen bonds approximately once every picosecond at room temperature.[70] Further temperature reduction leads to the crystallisation of water, forming ice. In this solid phase, the molecules move even more slowly. Contrary to what might be expected, the molecules in solid ice are less densely packed compared to their arrangement in the liquid phase, showcasing one of water's many unique properties. On average, each water molecule forms a tetrahedral network by bonding with approximately four other water molecules.[71,72] Two oxygen atoms are generally separated by a distance of 2.8 Å.[73] However, this value is shifted with temperature[74,75] due to structural alterations and the density maximum of water can be found at 4°C.

2.3 Carbohydrates

Some of the most abundant biomolecules on Earth are the carbohydrates. The name "carbohydrates" originates from the belief that such substances were hydrates of carbon.[76] The general molecular formula can be expressed as $C_n(H_2O)_m$. Based on their level of polymerisation, carbohydrates can be categorised into four principal groups: mono-, di-, oligo-, and polysaccharides. Monosaccharides are the most simple forms of sugar and are seen as the building block of carbohydrates. One very important monosaccharide is glucose which is the primary source of energy in most organisms.[77] When two monosaccharides form a glycosidic bond, a disaccharide is produced, examples of which include sucrose and trehalose.

2.3.1 Sucrose and Trehalose

Sucrose, the most common disaccharide, is produced in nature by plants such as sugar beets and sugar cane and represents an important dietary carbohydrate. The structurally similar disaccharide, trehalose, is synthesised by some bacteria and fungi to be used as a source of energy. In addition, trehalose exists in various desiccation-tolerant organisms, such as the brine shrimp *Artemia*, where it serves as a means of protection from drying.[78] Trehalose is not the only disaccharide that increases the stability of proteins and other biomolecules, disaccharides in general have been seen to possess this ability.[50,79,80] For example, sucrose has been found to exist in desiccation-tolerant pollen and seeds.[81]

Sucrose and trehalose are two structurally similar disaccharides, sharing the same chemical formula ($C_{12}H_{22}O_{11}$) with a molecular weight of 342.3 g/mol. However, there is a major difference in their respective intramolecular structures, which gives rise to potentially crucial differences. Figures 2.3(a) and (b) show the structures of sucrose and trehalose, respectively. In sucrose, a glucose and a fructose unit are connected through an α-1, β-2-glycosidic bond, while trehalose consists of two glucose units linked via an α-(1-1)-glycosidic bond.[82] This structural difference has significant implications for their physical and chemical properties. The α-(1-1) linkage in trehalose promotes extensive intermolecular hydrogen bonding, contributing to its high stability and protective capacity, while the α-1, β-2 linkage in sucrose limits such interactions.[83] Consequently, sucrose is more susceptible to acid-catalysed hydrolysis, whereas trehalose is notably resistant and only hydrolysed under severe conditions.[84,85] The higher bond dissociation energy reported for sucrose (27 kcal mol^{-1}) compared to trehalose (1 kcal mol^{-1}) reflects this difference in structural stability.[85]

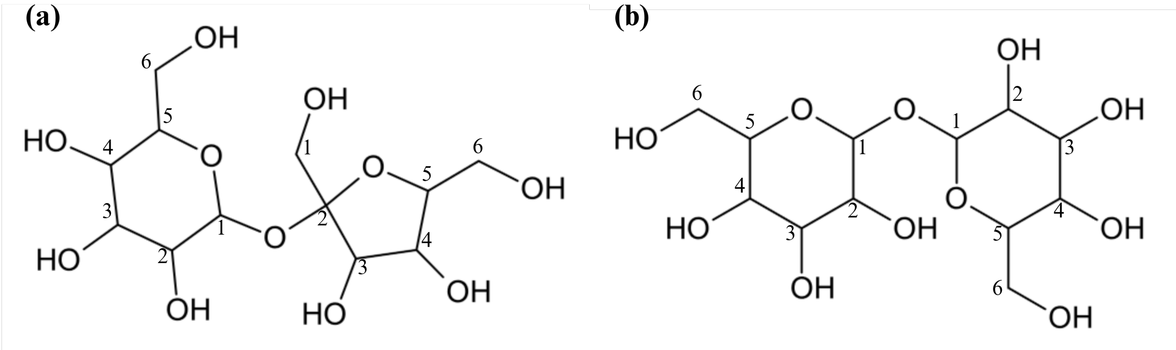

Figure 2.3: Chemical structure of (a) sucrose and (b) trehalose. In sucrose it is the first carbon of the glucose ring and the second carbon of the fructose ring that takes part in the glycosidic linkage, while in trehalose it is the first carbon in both of the glucose rings.

Disaccharides can be divided into reducing and non-reducing sugars depending on the chemical structure of the molecule. Reducing sugars, unlike non-reducing ones, have free aldehyde or ketone groups, which makes them more chemically reactive. Both sucrose and trehalose are non-reducing disaccharides[82] since the glycosidic bond is between their hemiacetal carbon atoms. This reduces the chemical reactivity of both sucrose and trehalose, which might be of great importance when it comes to their use as stabilising agents. However, it should be mentioned that upon hydrolysis, both disaccharides are reduced into two reducing monosaccharides, a process more likely for sucrose.[85]

These structural and chemical differences may seem small. However, they might be crucial when it comes to stabilising proteins, and other biomolecules, as they affect both how the disaccharides interact with the biomolecule itself and the surrounding water molecules. As mentioned in section 2.2, water forms a tetrahedral network via hydrogen bonding to other water molecules. The addition of disaccharides to water has been seen, in a vast number of studies, to disrupt the tetrahedral network.[86–90] These studies have also shown that, via extensive hydrogen bonding, trehalose possesses the ability to disrupt the water structure more efficiently compared to other disaccharides. This has been seen as a contribution to the superior stabilising effect of trehalose as it breaks up the structure of water, which would give rise to ice formation upon cooling.

Moreover, studies have shown that the dynamics of the disaccharides and water is strongly coupled and that the coupling strength in trehalose-water solutions is higher compared to other disaccharides, such as sucrose,[90] and that trehalose slows the dynamics of water to a greater extent compared to other disaccharides.[90] This will be discussed further in section 2.6.1.

2.4 Proteins

In 1838, the Swedish chemist Jöns Jakob Berzelius suggested to the Dutch chemist Gerardus Mulder that an unknown substance, vital for both animals and plants, should be named protein.[91] It originates from the Greek word *proteios* which means *of primary importance*.[91,92] This term captures the importance of proteins and the role they play. Their discovery has revolutionised our understanding of biological processes and led to significant advancements in health and medicine. The subsequent sections will emphasise the significance of functional proteins and explore the implications of their malfunction.

2.4.1 The Structure and Chemistry of Proteins

Amino acids linked together, by the means of covalent peptide bonds, form a long peptide chain which constitutes the macromolecules commonly referred to as proteins. The peptide bond is formed when two amino acids come together via the carboxylic and amino group, respectively, and release a water molecule. *In vivo* proteins are synthesised in the ribosome, which is an organelle in the cell consisting of both RNA and protein. It is the responsibility of the ribosome to translate the genetic code transcribed in mRNA into the amino acid sequence of each protein.[93] The amino acid sequence is unique for every protein and it defines the function of the protein. Almost all amino acids that have been found in proteins have the structure

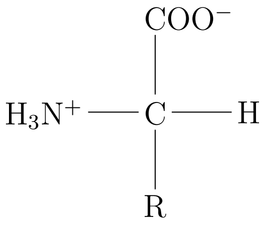

$$H_3N^+ - \underset{\displaystyle R}{\overset{\displaystyle COO^-}{C}} - H$$

where the central carbon is referred to as the α-carbon and has a hydrogen atom, a carboxyl group, and an amino group attached to it.[94,95] The R-group is referred to as an amino acid side chain specific for each amino acid.

The structure of protein molecules is organised in a structural hierarchy. It was the Danish biochemist Kai Linderstrøm-Lang who coined the terms *primary*, *secondary*, and *tertiary* structure,[96] which refer to the different structure levels that describe the structural hierarchy in proteins. The primary protein structure contains information about the number and sequence of amino acids. The secondary protein structure describes the local three-dimensional structure, where the two most common structures are α-helix and β-sheet. Figures 2.4(a) and (b) show a visualisation of α-helices and a β-sheet, respectively. In the former, a single polypeptide chain twists around itself to form an α-helical structure with 3.6 residues per turn.[96] β-sheets are β-strands connected laterally by hydrogen bonds, forming a pleated sheet structure. The strands can be arranged in parallel, antiparallel, or mixed orientations. Both α-helices and β-sheets are stabilised by hydrogen bonds between the amine groups and the carbonyl oxygen.[96] However, for α-helices the hydrogen bonds are formed within the polypeptide chain, whereas in β-sheets they are formed between adjacent polypeptide chains.

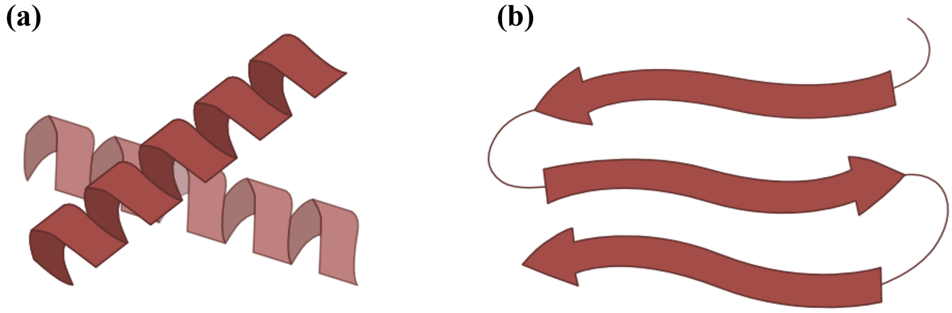

Figure 2.4: Visualisation of (a) polypeptide chains twisted around themself forming α-helices and (b) three β-stands connected together forming a β-sheet.

The three-dimensional fold is referred to as the tertiary protein structure and occurs primarily due to side chain interactions such as hydrogen bonding, hydrophobic effect, ionic bonding, dipole-dipole interactions, and London dispersion forces. Hydrophobic amino acids are generally buried inside the interior of the protein to minimise their contact with water. This burial, driven by the hydrophobic effect, is the dominant force stabilising the tertiary structure of globular proteins.[97] If a protein consists of more than one polypeptide chain it can form a fourth hierarchical structure referred to as the *quaternary* protein structure. The two proteins that have been studied in this thesis are myoglobin and hen egg white lysozyme (HEWL), both of which consist of a single polypeptide chain. More details about the structure and chemistry of proteins can be found in several textbooks such as Ref. 98.

2.4.2 Myoglobin and Lysozyme

The first protein to have its three-dimensional structure revealed was myoglobin. This discovery was made in 1958 by the British biochemist and crystallographer, John Kendrew, by the use of X-ray crystallography.[99] It is a significant milestone in the field of molecular biology and biochemistry as it provides deep insights into protein structure and function. Myoglobin is a single-chain, globular protein consisting of 153 amino acids and has a molecular weight of around 17 kDa.[100] The main function of myoglobin is to supply and store oxygen to the cells in our muscles. The myoglobin used in papers I and II comes from equine heart which has the same amount of amino acids and a similar molecular weight as myoglobin found in humans. Figure 2.5(a) shows the three-dimensional structure of myoglobin, from which it can be seen that the secondary structure consists of eight α-helices and a heme-group.

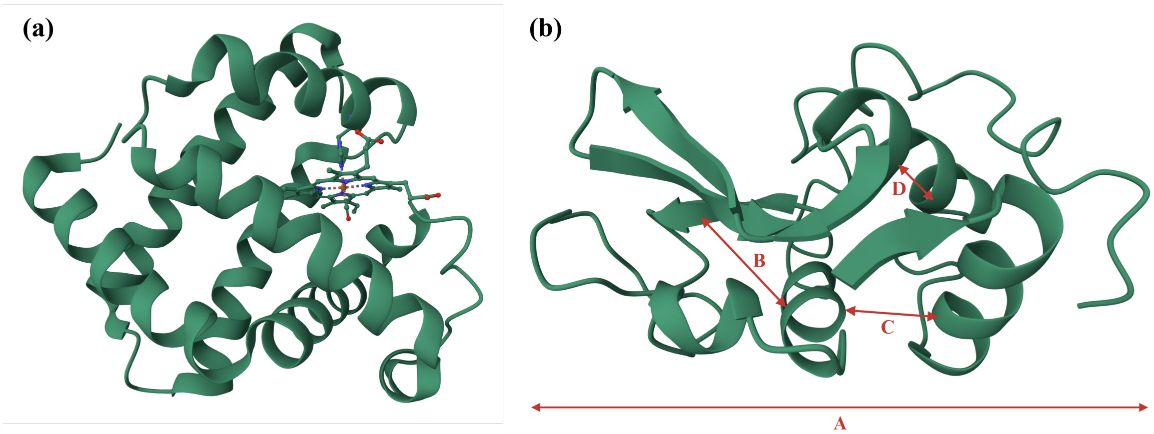

Figure 2.5: The three-dimensional structure of (a) myoglobin and (b) HEWL. Both structures were obtained from protein data bank, 1DWR[101] and 1LYS respectively.[102]

In 1922, Alexander Fleming discovered the protein lysozyme.[103] It is a small (14.3 kDa) globular enzyme, consisting of 130 amino acids,[104] and is commonly found in human tears, saliva[105] and nasal mucous.[106] The protein is essential as its main function is to hydrolyze the hydrocarbon chains in bacterial cell walls. However, human lysozyme is also related to the very rare disease hereditary lysozyme amyloidosis.[107] Hereditary lysozyme amyloidosis is a condition in which the protein lysozyme misfolds, aggregates and forms insoluble amyloid fibrils.[b] Such fibrils accumulate in various tissues in the body, disrupting their normal structure and function.[108, 109]

Hen egg white lysozyme (HEWL), an ortholog of human lysozyme,[110] is commonly used as a model protein for amyloid fibril analysis[111, 112] as it readily forms amyloid fibrils under appropriate destabilizing conditions.[113] Despite similar function, their amino acid sequences differ slightly; the amino acid sequence of HEWL consists of 129 amino acids and has a molecular weight of 13.9 kDa.[114] The three-dimensional structure of HEWL is shown in Figure 2.5(b), where it can be seen that its secondary structure consists of a mixture of five to seven α-helices and a three-stranded anti-parallel β-sheet. The protein has four stabilising disulfide bridges. *A*–*D* refer to different hierarchical structure levels

---

[b] The concept of amyloid fibrils will be explained in section 2.5.3.

of the protein. Firstly, A refers to the tertiary structure of the protein and B to the inter-domain correlation (the distance between the β-sheet and the α-helix). C refers to the intra-domain correlation, for example the distance separating two α-helices. Lastly, D refers to secondary structure, including the correlation between side-chains.[115]

2.5 Protein Stability

One focus of this thesis has been to investigate the stabilising effect the disaccharide trehalose has upon proteins and how this compares to the stabilising effect of sucrose, which leads to an important question: *What is protein stability?* In this thesis, two different aspects of protein stability have been considered: the classic thermodynamic and the dynamic stability. The thermodynamic stability is highly associated with protein folding and unfolding.

2.5.1 Protein folding and unfolding

To be able to function properly, most proteins need to be folded into their respective native state. A correctly folded protein is one where the amino acid chain forms the secondary structure, which then folds into the tertiary structure, as explained in section 2.4.1, resulting in the protein achieving its lowest energy state. A change in the physical and/or chemical environment of the protein can lead to protein denaturation (protein unfolding). Examples of such can be an increase of temperature, changing the pH, adding a chemical denaturant, or applying pressure.

The folding process of proteins is a complicated subject that has been studied for many years. The complexity of proteins, combined with their ability to assume their native state in a matter of seconds, suggests that proteins do not fold at random. This idea, later known as "Levinthal's paradox", was introduced by the American scientist Cyrus Levinthal in the 1960s.[116] According to Levinthal, protein folding should occur under kinetic control rather than thermodynamic control, which suggests that a protein must fold into the local energy minimum via the fastest folding pathway.[117,118] This observation has led scientists to explore alternative hypotheses that could explain the folding of proteins.

Different hypotheses for explaining the mechanism of protein folding have been proposed, one of which is called the *free energy landscape theory.* A visualisation of the protein folding funnel is shown in Figure 2.6. It visualises the free energy of each conformation in the folding process as a function of the degrees of freedom. The theory states that the protein can fold into intermediate states, which are meta-stable and from which the protein then quickly can fold into its native state.[117,119]

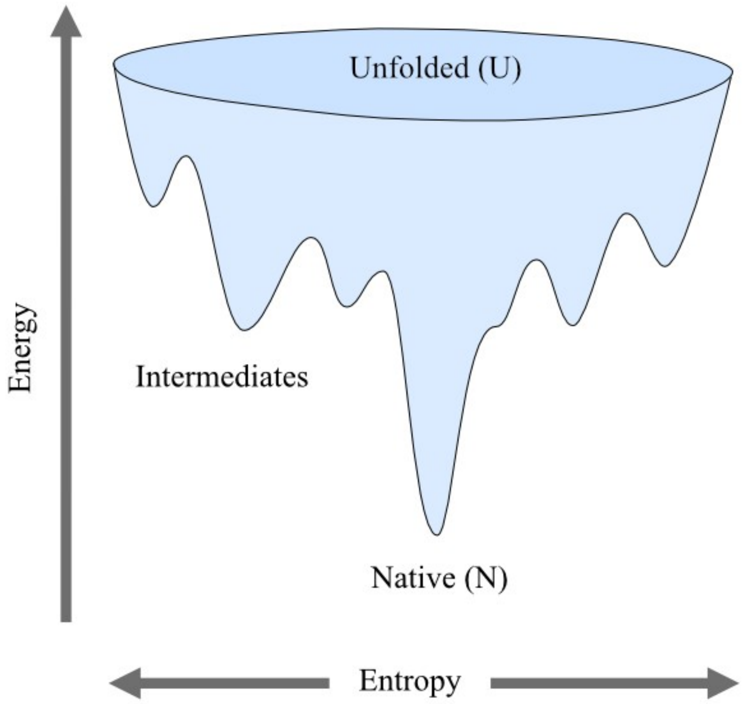

Figure 2.6: A simplified view of the ragged energy landscape of protein folding referred to as the "folding funnel". Higher positions in the landscape correspond to higher free-energy states in which the protein remains unfolded (U). As the protein folds, it may pass through intermediate, meta-stable conformations that occupy local minima, ultimately reaching the native (N) state at the bottom of the funnel. Vertical shifts illustrate changes in conformational entropy.

2.5.2 Thermodynamic Stability

In the classic thermodynamic treatment of protein stability, the focus is on the equilibrium between the native (folded) and denatured (unfolded) states. Most proteins need to be able to fold into their native state and remain there under physiological conditions in order to function.[120] The stability of a protein refers to its ability to maintain its native structure in the face of external stresses such as heat or chemical denaturants.[121] If a protein undergoes denaturation, its biological activity can be lost[c].

The thermodynamic stability of a protein is quantified by the difference in Gibbs free energy, ΔG, between the native and denatured states:

---

[c] Denaturation typically leads to lost of protein function, though some proteins can refold and regain function under mild conditions, and intrinsically disordered proteins, which lack stable structure yet remain functional, are exceptions to this rule.

$$\Delta G = -RT\ln K_{\mathrm{eq}} = \Delta H - T\Delta S, \tag{2.8}$$

where R is the universal gas constant, T the absolute temperature, K_{eq} the equilibrium constant, ΔH the change in enthalpy, and ΔS is the change in conformational entropy.[118] A negative ΔG indicates that the native state is thermodynamically favoured.

The balance between enthalpy and entropy determines which state is favoured. The dentured state has high conformational freedom and therefore high configurational entropy, whereas the native state is conformationally restricted. Since folding reduces the conformational entropy, it must be compensated by favourable enthalpy. This compensation arises primarily from the tight packing of side chains in the protein interior, including van der Waals interactions and hydrogen bonding.

The thermodynamic stability of a protein is strongly temperature-dependent. As temperature increases, the ordered hydration shell surrounding exposed hydrophobic side chains in the denatured state breaks down, increasing the enthalpy of the unfolded state. At the same time , the entropy of unfolding increases because fewer water molecules are ordered around the hydrophobic residues. Since the $T\Delta S$ term grows with temperature, the entropic contribution eventually dominates: when $|T\Delta S| > |\Delta H|$, the free energy favours the denatured state, and thermal denaturation occurs. In other words, thermal denaturation is driven by the entropy of the denatured state becoming dominant at high temperatures.[122] More details about the thermodynamics of protein folding can be found in Refs. 98, 122.

2.5.3 Misfolding and Aggregation

Most proteins need to be able to fold properly into its native state and remain there under physiological conditions, in order to function. When a protein is unable to fold correctly or maintain its proper structure, it can misfold or assume an alternative form. This is called misfolding and can lead to a destabilised protein and aggregation. Misfolding and aggregation can depend on a variety of different factors such as protein concentration, temperature, and pH, and can in some cases lead to the formation of amyloid fibrils. Amyloid fibrils are highly structured protein aggregates, which are associated with two of the most common neurodegenerative diseases: Alzheimer's and Parkinson's,[123–125] but also with non-neurodegenerative diseases such as hereditary lysozyme amyloidosis. Amorphous protein aggregates are protein aggregates that lack specific high-order structure.[126] In Figure 2.7 it can be seen that the stability of the amorphous aggregates and the amyloid fibrils is higher than for the native state of the protein.[127, 128]

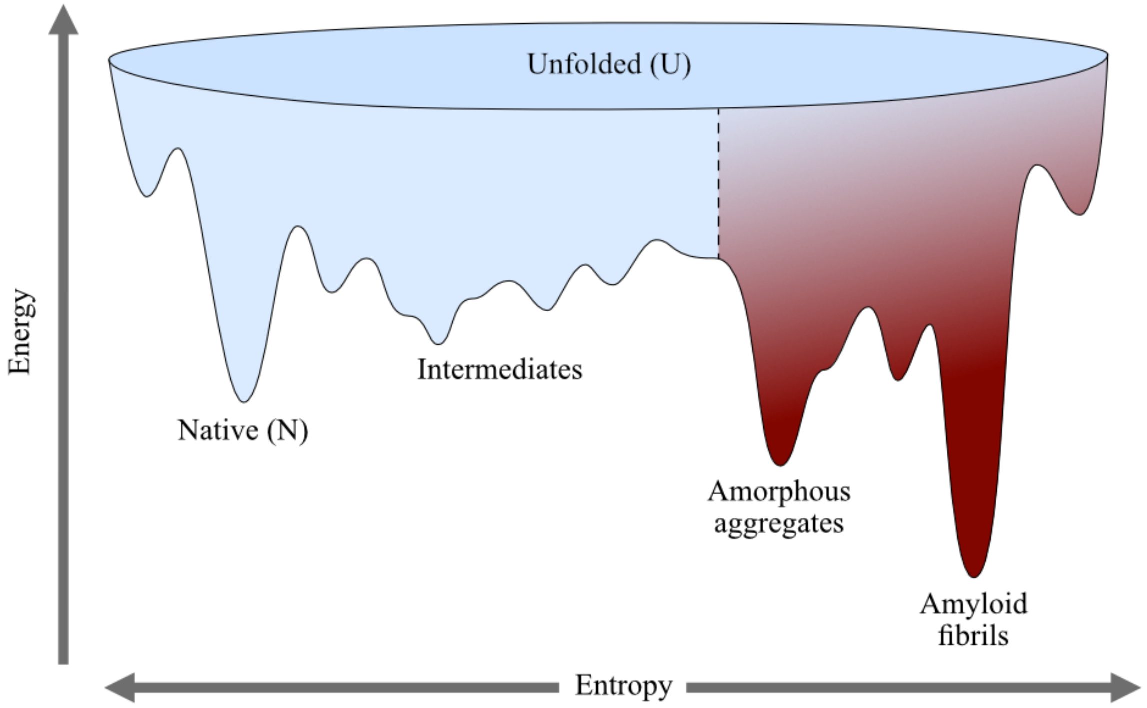

Figure 2.7: A simplified representation of the extended energy landscape of protein folding, often described as the "extended folding funnel". The extended region of the funnel (highlighted in red) depicts pathways leading to misfolding and aggregation. Amorphous aggregates reside in an energy minimum lower than that of the native state, amyloid fibrils occupy the lowest free-energy state.

2.5.3.1 Amyloid Fibrils

It was the German physician Rudolph Virchow who, in 1854, first introduced the term "amyloid" to describe a macroscopic tissue abnormality that exhibited a positive iodine staining reaction.[2] In 1859, Friedrich and Kekulé[129] uncovered the high nitrogen content in fibrils, leading to the classification of amyloid fibrils as proteins. Since then, extensive structural characterisation has revealed that amyloid fibrils are not disordered aggregates, but highly organised assemblies with a well-defined architecture.

Amyloid fibrils are highly structured, linear, protein aggregates, which consist of β-sheet structure oriented perpendicular to the long axis of the fibril. The structure of an amyloid fibril can be seen in Figure 2.8. Amyloid fibrils are characterised by the cross-β fold, which contains two main distances: 4.7 Å and 10 Å. The former is the intrastrand distance separating two adjacent monomers, and the latter is the intersheet spacing between two β-sheet layers.[130] This gives rise to characteristic anisotropic patterns within amyloid fibrils, which were discovered using X-ray diffraction.[7,131]

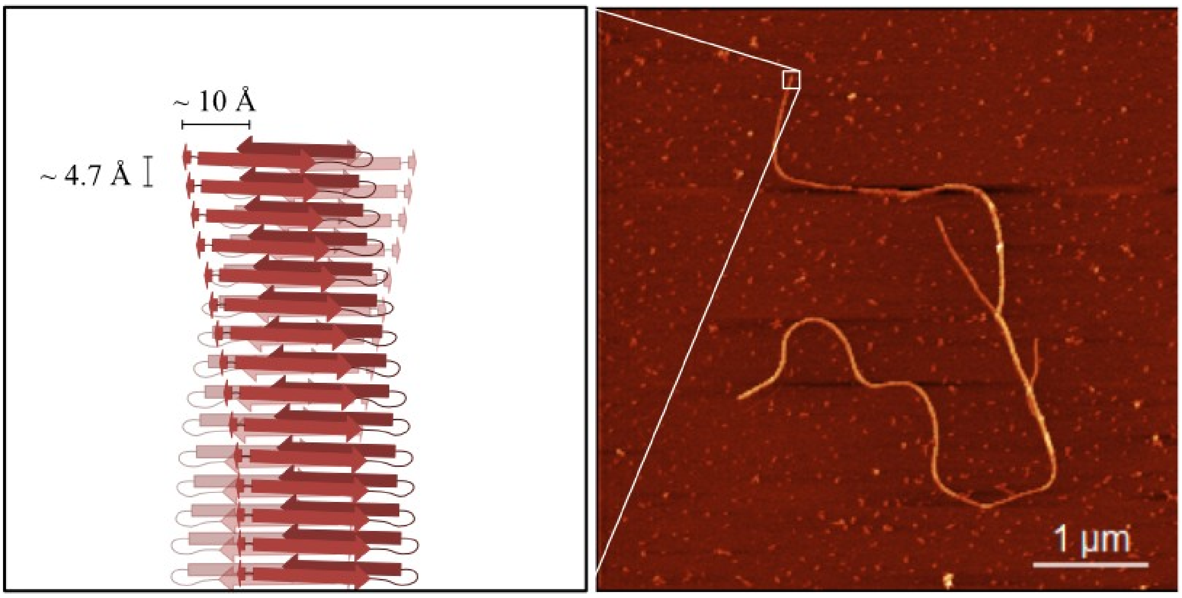

Figure 2.8: The left panel shows the characteristic structure of an amyloid fibril. The arrows represent β-strands, which are separated by $\sim$ 4.7 Å. The β-sheets are separated by $\sim$ 10 Å. The right panel is an amyloid fibril from HEWL imaged using AFM.

To be able to form amyloid fibrils, the protein needs to undergo partial unfolding or misfolding. This can be triggered by various factors such as mutations, changes in pH, temperature, ionic strength, or interaction with other molecules and is unique for each protein. The misfolded state exposes hydrophobic regions that are usually buried in the native state, making the protein more prone to aggregate. The formation of amyloid fibrils from lysozyme is suggested to start with nucleation, a critical step, which involves the formation of a small cluster of misfolded proteins. This step is a rate-limiting step referred to as primary nucleation and involves protein monomers only. Monomer-dependent secondary nucleation is when a new nuclei is formed on the surface of an already formed fibril, which accelerates the aggregation process.[132] Once a nucleus is formed, the structure is elongated by the addition of monomers to the ends of the fibrils. The elongation is a fast process compared to the nucleation. Mature lysozyme fibrils can undergo further association, leading to larger aggregates. This can result in the formation of insoluble amyloid deposits, which can be found in various tissues and organs in the case of amyloidoses.

2.6 Protein Dynamics

Protein dynamics are essential for several biological activities, such as enzyme catalysis, ligand binding, and signal transduction.[133] These dynamics are governed by the underlying energy landscape of the protein.[134] Like protein structure, protein dynamics are hierarchical, spanning multiple time and length scales.[133,135,136] Capturing the full dynamic spectrum therefore requires a combination of complementary techniques. Experimentally, these include nuclear magnetic resonance (NMR),[137] inelastic and quasielastic neutron scattering (INS/QENS)[138–140] and dielectric spectroscopy.[33,141–144] Molecular dynamics (MD) simulations[145] provide a complementary computational approach for characterising the dynamics of proteins at atomic resolution.

At the largest length scale, entire proteins undergo translational and rotational diffusion, governed by solvent properties and molecular crowding.[146] The largest internal motions are collective domain fluctuations, including hinge-bending[147] and domain rotations, occurring on time scales from tens of nanoseconds to milliseconds.[136,148] On shorter length scales of several Ångströms, localised motions dominate. These include backbone fluctuations, confined side-chain diffusion, and rotations of side groups such as methyl groups.[148,149] These local motions exhibit a broad distribution of relaxation times, reflecting the chemical and structural diversity of local environments, and are commonly referred to as β-relaxations.

The temperature dependence of protein dynamics is closely linked to the glass transition. Below the glass transition temperature (T_{g}), the system enters a glassy state in which only small-amplitude motions, such as vibrations, short-range fluctuations, and β-relaxations, can be observed.[150] In hydrated proteins, these local relaxations are thought to be slaved to the β-relaxation of the surrounding solvent. Above T_{g}, the β-relaxation of the solvent merges with the large-scale α-relaxation, enabling the protein to undergo large-scale conformational changes. Understanding how protein dynamics are influenced by the local environment, including hydration water and stabilising additives such as disaccharides, is essential for improving protein stability.

2.6.1 The Effect of Hydration Water and Disaccharides

Proteins require conformational flexibility to function[134] and are essentially inactive in their dehydrated state; water is therefore critical to protein function.[151] A protein is generally considered hydrated by a single layer of water molecules at hydration levels of 0.3–0.4 g water/g protein,[152] which is where protein function resumes. This hydration water behaves differently from bulk water: it does not participate in ice formation upon cooling and exhibits much slower dynamics.

The dynamics of proteins and their surrounding solvent are intimately coupled. Fluctuations of protein domains are slaved by those of the surrounding solvent,[153] a concept first introduced by Fenimore et al.[154] and since then confirmed by both experiments[139,141,144,155–157] and simulations.[158] Specifically, global conformational changes of a protein are governed by the α-relaxation of the bulk solvent.[155] This is the cooperative structural relaxation associated with the glass transition, involving large scale collective rearrangements of solvent molecules. More local protein motions are instead slaved by the β-relaxation of the hydration water,[155] a faster and more localised process involving reorientations of individual molecules that persists even below T_{g}. While the α-relaxation exhibits a non-Arrhenius temperature dependence, following a Vogel-Fulcher-Tammann (VFT) equation, and freezes out at T_g, the β-relaxation is approximately Arrhenius with a roughly constant activation energy. Dielectric spectroscopy measurements have shown that proteins exhibit their own distinct α-relaxation, corresponding to large-scale conformational motions, which is iteslf slaved by the solvent α-relaxation.[159]

This slaving behaviour has direct implications for protein stabilisation. While proteins need conformational flexibility to function, increasing temperature shifts the folding equilibrium toward the denatured state. One strategy for preserving protein stability is cryopreservation, a common method for long-term storage of biological materials such as proteins,[160] living cells[161] and tissues, using very low temperatures.[162] However, freezing can be lethal for most living organisms due to ice formation, which causes mechanical damage and osmotic stress as solutes become concentrated in the remaining unfrozen liquid.

To avoid ice formation, cryoprotectants such as trehalose are commonly added, allowing the system to supercool and subsequently vitrify into a glassy state. The T_g is often used as a measure of stability: as the protein approaches T_g, dynamics slow down and viscosity increases, so a higher T_g indicates that the system remains in a glassy state, thus stable, at higher temperatures. Additives that slow solvent relaxations also suppress the protein motions coupled to them. Trehalose slows the α-relaxation of the solvent more effectively than sucrose, and thereby also slows large-scale protein motions above T_g. Below T_g trehalose also slows down the water relaxation more than sucrose, resulting in more efficient suppression of protein motions.[159] However, T_g alone cannot explain trehalose's superior stabilising properties, as other stabilising agents with even higher T_g values do not achieve the same effect.

3

Theory of Methods

This thesis employs a combination of experimental techniques to investigate protein structure, dynamics, and stability across different time and length scales, and how these properties are affected by disaccharides. The complexity of such systems necessitates a multi-technique approach spanning scattering, calorimetry, spectroscopy, and microscopy. Neutron scattering has been a central technique. In papers I, II, and VI, neutron diffraction combined with empirical potential structure refinement (EPSR) or Dissolve modelling provided detailed structural information on protein–sugar–water systems. Quasielastic neutron scattering (QENS) probed the dynamics of disaccharides and water in papers I and II, complemented by molecular dynamics (MD) simulations in paper I. In paper V, neutron spin-echo (NSE) and dielectric spectroscopy (DS) were used to investigate internal and collective protein dynamics in amyloid fibrils. In paper I, X-ray diffraction provided a complementary dataset for the structural modelling, while small- and wide-angle X-ray scattering (SAXS/WAXS) were used in papers III and V to confirm the presence of amyloid fibrils and examine the inhibitory effects of trehalose and sucrose on fibril formation. Beyond scattering, differential scanning calorimetry (DSC) was used in papers III and IV to study thermally induced transitions, including protein denaturation, water crystallisation, and the glass transition. Finally, atomic force microscopy (AFM) was employed in papers III and V to confirm and characterise the fibrillar structures.

3.1 X-ray and Neutron Scattering

X-ray and neutron scattering have a long history in structural biology. One groundbreaking discovery was the first three-dimensional structure of the protein myoglobin, determined by the British biochemist John Kendrew using X-ray crystallography.[99] The structure of myoglobin was later studied using neutrons, which revealed the positions of the hydrogen atoms that were almost invisible to X-rays. This illustrates a key advantage of neutrons over X-rays: their sensitivity to light elements, in particular hydrogen, the most abundant element in biological matter.

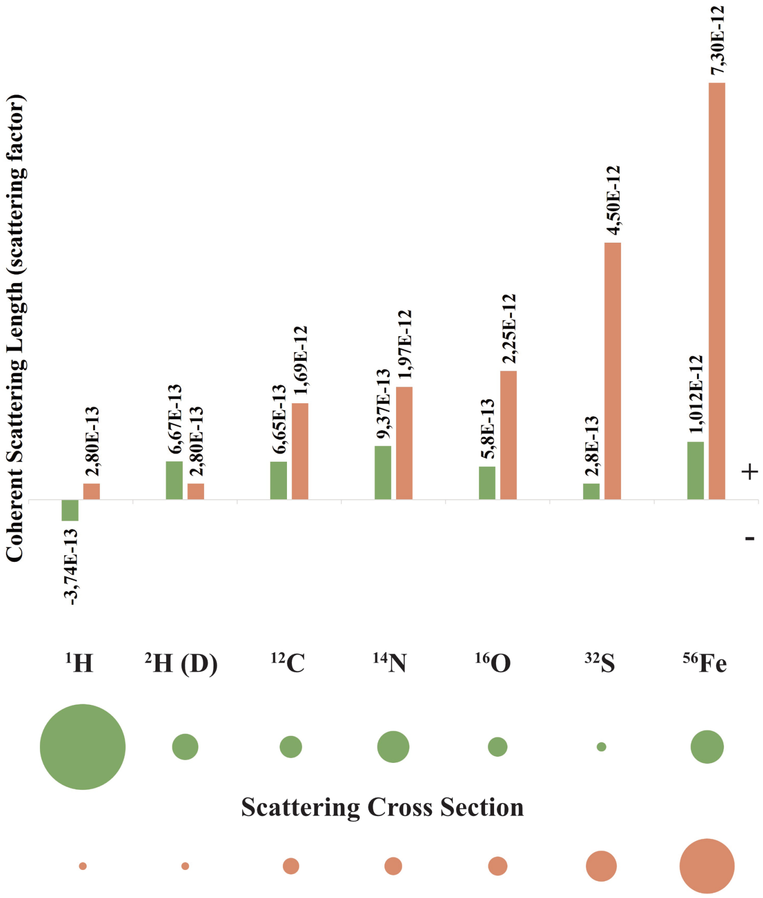

Figure 3.1: Coherent scattering lengths (top) and scattering cross sections (bottom) for some elements using neutrons (green) and X-rays (orange). Both the circles and bars are drawn to scale comparing that of neutrons and X-rays.[a]

This complementarity between the two techniques originates from the fundamentally different way each probe interacts with matter. X-ray and neutron scattering are fundamentally similar non-destructive techniques,[167] which can be used to investigate both amorphous and crystalline materials on a nanometre scale and although they are based on the same principle, the nature of the incoming particles differ. In X-ray scattering, photons interact with the electron cloud surrounding the atomic nuclei, so the scattering cross section scales with atomic number, and heavy elements dominate the signal while light elements such as hydrogen are nearly invisible. In neutron scattering, the neutrons interact directly with the atomic nuclei, and the scattering cross section varies non-symmetrically across the periodic table. As a result, light elements, hydrogen in particular, can scatter as strongly as, or even more strongly than heavy elements, making neutrons uniquely suited to study biological matter. The difference in contrast,

---

[a] The figure was inspired by Ref. 163. The neutron scattering cross sections were obtained from Ref. 164. Coherent scattering lengths and scattering factors were obtained from Ref. 165 and the X-ray scattering cross sections were taken from Ref. 166.

illustrated in Figure 3.1, enables the use of X-ray and neutron scattering as complementary techniques.

In neutron scattering, there are two different sources to harvest neutrons, reactor-source and spallation-source.[168] A reactor-source is usually continuous and the neutrons are a by-product of radioactive decay from uranium (^{235}U), whereas a spallation-source is pulsed and the neutrons are released from a heavy material, such as tungsten, after the collision with high energy protons.[169]

3.1.1 Isotope Substitution

In neutron scattering, the neutrons interact with the nucleus of the atom, which implies that the scattering cross section varies between isotopes. This makes neutron scattering a suitable technique in the study of biological systems, since they usually contain a lot of hydrogen. As mentioned in section 3.1, hydrogen has a much larger scattering cross section than deuterium, which can be useful when studying dynamics. Furthermore, hydrogen has a negative coherent scattering length, whereas deuterium has a positive one. This means that when hydrogen is correlated with atoms of positive scattering length, it gives rise to negative contributions in the coherent scattering, which enhances the contrast. The difference between hydrogen and deuterium can therefore be exploited as a method to "highlight" parts of the system that are of interest. This is illustrated in Figure 3.2, where the orange and green parts represent deuterated and hydrogenated parts, respectively.

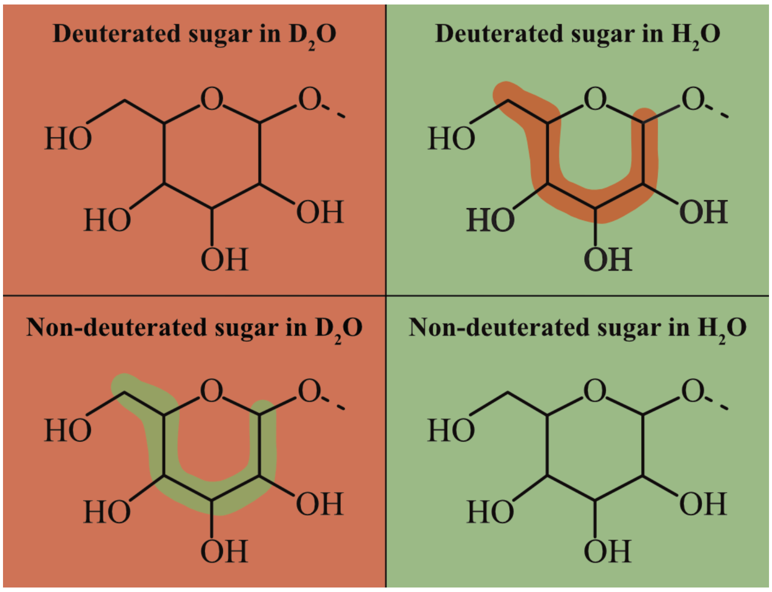

Figure 3.2: Schematic illustration of how different parts of a molecule can be "highlighted" by the use of isotope substitution, where the orange and green colours represent deuterated and protonated components, respectively.

3.1.2 Elastic and Inelastic Scattering

The principle of particle scattering, whether the particle is a photon or a neutron, is the change of momentum, P, and energy, E, of the incident particle. The momentum transfer can be expressed as

$$\mathbf{P} = \hbar(\mathbf{k} - \mathbf{k}') = \hbar\mathbf{Q}, \tag{3.1}$$

where $\hbar$ is the reduced Planck constant and $\mathbf{Q} = \mathbf{k} - \mathbf{k}'$ is the scattering vector defined as the difference between the wave vector of the incident and final wave. The energy transfer is expressed as

$$\Delta E = \hbar\Delta\omega, \tag{3.2}$$

where $\Delta\omega$ is the difference between the angular frequency of the incident, ω_i, and final, ω_f, particle. When there is no exchange of energy, $\Delta E = 0 \Leftrightarrow \Delta\omega = 0$, the scattering is referred to as elastic. In such a case, $|\mathbf{k}| = |\mathbf{k}'| = 2\pi/\lambda$, where λ is the particle wavelength. In contrast, inelastic scattering occurs when the energy is not conserved, $\Delta E \neq 0$. One difference between neutrons and X-rays is that the energy of thermal neutrons is on the same order of magnitude as the vibrations of atoms. This implies that neutrons can be used to measure the transfer of energy. However, the energy of X-rays is much higher compared to neutrons, and it is therefore difficult to measure inelastic scattering using X-rays. The elastic neutron scattering is used to gain information regarding the atomic distribution in a system, whereas the inelastic neutron scattering provides information about the dynamics of the atoms. In the following sections, elastic scattering will be assumed if nothing else is stated.

The geometry involved in the scattering process is the same for both X-rays and neutrons. The incoming wave collides and scatters of the sample through an angle, 2θ, which leads to Bragg's law

$$|\mathbf{Q}| = Q = \frac{4\pi}{\lambda}\sin(\theta). \tag{3.3}$$

3.1.3 The wave-formalism

For both X-ray and neutron scattering, the incoming particles can, before impinging the sample, be described as a plane wave given by[b]

$$\psi_\mathrm{i}(\mathbf{r}) = \psi_0 e^{i\mathbf{kr}}, \tag{3.4}$$

where ψ_0 is the amplitude of the incident wave related to the incident flux as $\Phi = |\psi_0|^2$, and $\mathbf{k}$ is the wave-vector of the incoming wave at position $\mathbf{r}$. The outgoing scattered wave is spherical and the wave function (from a single nucleus) can hence be described as

---

[b] The formalism can be found in multiple textbooks such as Refs.[169, 170]

$$\psi_\mathrm{f}(\mathbf{r}) = -\psi_0 f(\lambda,\theta)\frac{e^{i\mathbf{k}'\cdot(\mathbf{r}-\mathbf{r}_j)}}{|\mathbf{r}-\mathbf{r}_j|}, \tag{3.5}$$

where $\mathbf{k}'$ is the wave-vector of the outgoing wave at position $\mathbf{r}_j$. Figure 3.3 displays an illustration of elastic scattering of an incoming plane to a final spherical wave.

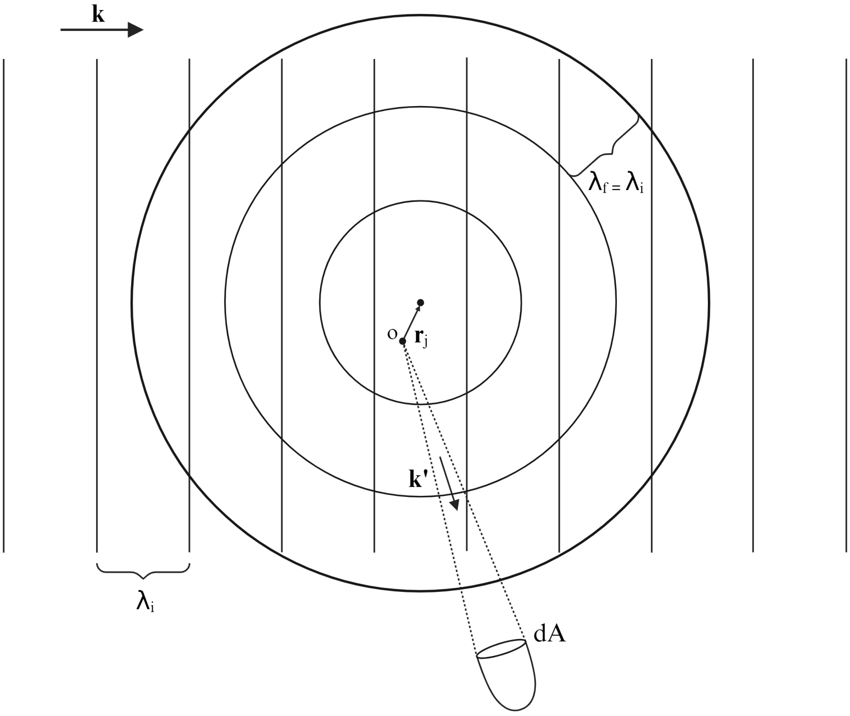

Figure 3.3: Elastic scattering where the initial (plane) wave, with wave vector **k** and wavelength λ_i, collide with an atom at position $\mathbf{r}_j$. The final (spherical) wave, with wave **k**' and wavelength λ_f, is scattered onto an area, dA.

The function $f(\lambda,\theta)$ given in eqn. (3.5) is different depending on whether the incoming particles are neutrons or photons.[169] For neutrons, $f(\lambda,\theta) = b$, where b is the scattering length of the nucleus, which is a measure of how strong the scattering from the nucleus is.[169] The scattering length depends on the nucleus as well as its spin relative to the neutron, which means that the scattering length changes depending on the isotope and that there are two different values of the scattering length if the nucleus has a non-zero spin.[169,171] Thus, eqn. (3.5) can, for neutron scattering, be written as

$$\psi_\mathrm{f}(\mathbf{r}) = -\psi_0 e^{i\mathbf{k}\cdot\mathbf{r}_j} b_j \frac{e^{i\mathbf{k}'\cdot(\mathbf{r}-\mathbf{r}_j)}}{|\mathbf{r}-\mathbf{r}_j|}. \tag{3.6}$$

In contrast, the scattering length in X-ray scattering depends on the atomic number, Z, as the X-rays do not interact with the nucleus but rather the electron cloud surrounding the atom. Therefore, $f(\lambda,\theta)$ is characterised differently using X-ray scattering. The function decays with increasing θ and decreasing λ and is a function of $\sin\theta/\lambda$, which leads to a decrease in $f(\lambda,\theta)$ with Q. This decrease is known as the atomic form factor.[169]

For a system consisting of N atoms, one needs to consider multiple spherical waves giving rise to interference. The outgoing wave function is then described as the sum of N individual wave functions,

$$\psi_{\mathrm{f}} = -\psi_0 e^{i\mathbf{k}\cdot\mathbf{r}} \sum_{j=1}^{N} \frac{b_j}{|\mathbf{r}-\mathbf{r}_j|} e^{i\mathbf{Q}\cdot\mathbf{r}_j}. \tag{3.7}$$

The interaction of a neutron with a nucleus can either lead to it being absorbed or scattered. The cross section, σ can therefore be divided into

$$\sigma = \sigma_{\mathrm{a}} + \sigma_{\mathrm{s}}, \tag{3.8}$$

where σ_{a} and σ_{s} are the absorption and scattering cross section, respectively. While the absorption cross section is related to $\mathbf{k}$, the total scattering cross section is related to the scattering length through

$$\sigma_{\mathrm{s}} = 4\pi\langle b^2\rangle, \tag{3.9}$$

where $\langle b^2\rangle = \frac{1}{N}\sum_{i=1}^{N} b_i^2$. In neutron scattering, the total cross section contains a coherent, σ^{coh}, and an incoherent, σ^{inc}, part. The difference between the respective parts is that the former contains both the scattering due to different nuclei and contributions due to self-scattering, whereas the incoherent part only contains self-scattering and is a result of the fact that different nuclei of the same atom type can have different spin states. The coherent and incoherent scattering cross sections are given by $\sigma^{\mathrm{coh}} = 4\pi\langle b\rangle^2$ and $\sigma^{\mathrm{inc}} = 4\pi(\langle b^2\rangle - \langle b\rangle^2)$, respectively.

3.1.4 Neutron Diffraction

Elastic coherent neutron scattering is known as neutron diffraction, which is an experimental technique used to gain information regarding the structural correlation lengths in the system of interest. The atomic structure of a liquid or an amorphous material is often described by the pair correlation function, $g(r)$, which is defined in section 2.1.2. The following section will describe how the pair correlation function relates to the data of a neutron scattering experiment.[c]

The output from neutron diffraction is the double differential scattering cross section, $\frac{d^2\sigma}{d\Omega dE_{\mathrm{f}}}(Q)$, which is defined as the fraction of neutrons, of final energy, E_{f}, scattered into solid angle $d\Omega$ with energies $\in [E_{\mathrm{f}};\ E_{\mathrm{f}} + dE_{\mathrm{f}}]$. As mentioned in section 3.1.2, one

---

[c] The derivation can be found in multiple textbooks and the reader is referred to Refs. 58, 169, 172 for more details.

does not have to account for the energy dependence of the scattered neutrons in elastic scattering. Therefore, the differential scattering cross section, $\frac{d\sigma}{d\Omega}$, can be obtained by integrating over all final energies,

$$\frac{d\sigma}{d\Omega} = \int_{-\infty}^{\infty} \frac{d^2\sigma}{d\Omega dE_{\mathrm{f}}} dE_{\mathrm{f}}. \tag{3.10}$$

In a neutron diffraction experiment the detectors measure the square modulus of the wave function. By making the assumption that the sample-to-detector distance, $\mathbf{r}$, is much larger than the distance between the nuclei, $\mathbf{r}_j$, one can approximate that $|\mathbf{r} - \mathbf{r}_j| \approx r$. The square modulus of eqn. (3.7) then becomes

$$|\psi_{\mathrm{f}}|^2 = \psi_{\mathrm{f}}\psi_{\mathrm{f}}^* = \frac{|\psi_0|^2}{r^2} \sum_{i=1}^{N} b_i e^{i\mathbf{Q}\cdot\mathbf{r}_i} \cdot \sum_{j=1}^{N} b_j^* e^{-i\mathbf{Q}\cdot\mathbf{r}_j}, \tag{3.11}$$

where i and j are indices representing two different scattering sites and $|\psi_0|^2 = \Psi$ is the flux of the incident wave. By defining the fraction incident neutrons scattered onto the area, dA, as $d\sigma = \frac{|\psi_{\mathrm{f}}|^2}{|\psi_0|^2} dA$, and the solid angle as $d\Omega = dA/r^2$, the differential scattering cross section can be written as

$$\frac{d\sigma}{d\Omega} = \frac{|\psi_{\mathrm{f}}|^2}{|\psi_0|^2} \frac{dA}{d\Omega} = \sum_{i=1}^{N} b_i e^{i\mathbf{Q}\cdot\mathbf{r}_i} \cdot \sum_{j=1}^{N} b_j^* e^{-i\mathbf{Q}\cdot\mathbf{r}_j}. \tag{3.12}$$

As previously mentioned, the scattering length in neutron scattering can vary based on element or isotope and on different spin orientations. For a nucleus with non-zero spin the scattering length has one of two different values, b^+ and b^-.[169] By averaging the nuclear scattering length, b, eqn. (3.12) can be rewritten as

$$\frac{d\sigma}{d\Omega} = \sum_{i,j}^{N} \langle b_i b_j^* \rangle e^{i\mathbf{Q}\cdot(\mathbf{r}_i - \mathbf{r}_j)}, \tag{3.13}$$

where the term $\langle b_i b_j^* \rangle$ can be separated into two different cases, $i = j$ and $i \neq j$. $i = j$ refers to the "self-scattering" of a nucleus whereas $i \neq j$ refers to the scattering of two different atoms. The two cases can be written as:[171]

$$\begin{aligned} &\text{for} \quad i = j: \qquad && \langle b^2 \rangle = \langle b \rangle^2 + \langle (b - \langle b \rangle)^2 \rangle \\ &\text{for} \quad i \neq j: \qquad && \langle b_i b_j^* \rangle = \langle b_j^* \rangle \langle b_j^* \rangle = \langle b \rangle^2. \end{aligned}$$

The scattering cross section can hence be divided into coherent and incoherent scattering, enabling eqn. (3.13) to be rewritten as

$$\frac{d\sigma}{d\Omega} = \underbrace{\langle b \rangle^2 \sum_{i,j}^{N} e^{i\mathbf{Q}\cdot(\mathbf{r}_i - \mathbf{r}_j)}}_{\text{coherent scattering}} + \underbrace{N(\langle b^2 \rangle - \langle b \rangle^2)}_{\text{incoherent scattering}}. \tag{3.14}$$

The coherent part is of most interest when it comes to diffraction studies since, as seen in eqn. (3.14), the incoherent part does not include any structural parameters. The coherent part is usually written as

$$\frac{d\sigma}{d\Omega}^{\mathrm{coh}} = N\langle b\rangle^2 S^{\mathrm{coh}}(\mathbf{Q}), \tag{3.15}$$

where $S^{\mathrm{coh}}(\mathbf{Q})$ is referred to as the coherent structure factor. To understand how the structure factor can be used to describe the structure of a material, one needs to understand the definition of $g(r)$, which is presented in section 2.1.2.

Using one of the main properties of the Dirac delta function, $\sum_i e^{i\mathbf{Q}\cdot\mathbf{r}_i} = \int_V e^{i\mathbf{Q}\cdot\mathbf{r}_i} \sum_i \delta(\mathbf{r}-\mathbf{r}_i)$, eqn. (3.15) can be rewritten as

$$S^{\mathrm{coh}}(\mathbf{Q}) = 1 + \frac{1}{N}\int e^{-i\mathbf{Q}\cdot\mathbf{r}} \sum_{i,j\neq i}^{N} \delta(\mathbf{r}-(\mathbf{r}_i-\mathbf{r}_j))d\mathbf{r}. \tag{3.16}$$

Subsequently, the definition of $g(\mathbf{r})$ can be inserted in eqn. (3.16) to obtain

$$S^{\mathrm{coh}}(\mathbf{Q}) = 1 + \rho\int e^{-i\mathbf{Q}\cdot\mathbf{r}} g(\mathbf{r})d\mathbf{r}, \tag{3.17}$$

which describes the relation between the coherent elastic structure factor and the pair correlation function. For an isotropic liquid the expression of the structure factor can be simplified to

$$S^{\mathrm{coh}}(Q) = 1 + 4\pi\rho\int_0^\infty r^2 g(r)\frac{\sin(Qr)}{Qr}dr. \tag{3.18}$$

Sometimes it can be useful to divide $S^{\mathrm{coh}}(Q)$ into partial structure factors, $S^{\mathrm{coh}}_{\alpha\beta}(Q)$, such that

$$S^{\mathrm{coh}}(Q) = \frac{\sum_{\alpha\beta}\langle b_\alpha\rangle\langle b_\beta\rangle(S^{\mathrm{coh}}_{\alpha\beta}(Q)-1)}{\sum_\alpha c_\alpha\langle b_\alpha\rangle^2}. \tag{3.19}$$

Similarly as $S^{\mathrm{coh}}(Q)$ can be related to $g(r)$, $S^{\mathrm{coh}}_{\alpha\beta}(Q)$ can be related to the partial pair correlation function by

$$S^{\mathrm{coh}}_{\alpha\beta}(Q) = c_\alpha\delta_{\alpha\beta} + c_\alpha c_\beta\rho\int e^{-i\mathbf{Q}\cdot\mathbf{r}} g_{\alpha\beta}(r)d\mathbf{r} \tag{3.20}$$

In papers I, II and VI, neutron diffraction was used to examine the structure in protein-sugar-water systems. The neutron diffraction experiments were performed on the NIMROD instrument[173] at the ISIS Pulsed Neutron and Muon Source, STFC Rutherford Appleton Laboratory, UK. The diffractometer has a broad Q-range of 0.01–50 Å^{-1} and the neutrons arrive to the sample with wavelengths between 0.05–10 Å. This is what makes NIMROD unique as it can probe structures at different length scales ranging from the interatomic ($<$ 1 Å) to the mesoscopic ($>$ 300 Å).[173] The samples were measured inside 1 mm thick $\mathrm{Ti_{0.676}Zr_{0.324}}$ containers, which were sealed with a PTFE O-ring. The samples in papers I and II were measured at 300 K and the samples in paper VI at 310 K.

The fully protonated myoglobin sample in paper I was analysed using X-ray diffraction. The measurement was also performed at the ISIS Pulsed Neutron and Muon Source, using Ag anode X-ray diffractometer (Empyrean),[174] with a wavelength of $\lambda = 0.5609$ Å. The sample was placed in silica glass capillaries with a thickness of 2 mm.

3.1.4.1 Data Corrections

The raw neutron and X-ray diffraction data in papers I and II was "corrected" using the GUDRUN and GUDRUN-X data correction software,[56] respectively, in order to obtain useful structure factors. Apart from the scattering from the sample holder ($Ti_{0.676}Zr_{0.324}$ containers and quartz/glass capillaries for neutron and X-ray scattering, respectively), the measured scattering data needs to be corrected for multiple scattering events, attenuation, and detector *dead time*.

To provide an absolute scale for the neutron scattering data, it was normalised to a vanadium[d] standard of suitable geometry, which enables the number of detected neutrons at the detector to be divided with the number of theoretically detected neutrons. This provides a normalisation factor for each detector. Unfortunately, there is nothing equivalent for X-rays. However, the method used in GUDRUN-X works rather well.[e].

In section 3.1, it was assumed that multiple scattering events did not occur and that there is no absorption of neutrons in the sample. However, in reality, this assumption is only accurate if the attenuation and multiple scattering cross sections are not too large. By knowing the atom composition and the geometry of the sample, the attenuation and probability of multiple scattering can be calculated and subsequently corrected for. This is then calculated as the background signal and is subtracted from the final structure factor.

Finally, in neutron scattering, corrections for the detector *dead time* need to be performed. The *dead time* refers to the interval between the detection of one neutron and the registration of the next by the detector. It results in some neutrons being neglected. Therefore, this is compensated for using GUDRUN.

3.1.4.2 Structure Refinement Modelling

Neutron and X-ray diffraction data are used to gain information regarding the structure within the system of interest and can be used as an experimental basis for an atomic model. Empirical Potential Structure Refinement (EPSR)[175] is an iterative modelling

---

[d] Vanadium is used due to its small coherent scattering length.

[e] This method is described in more detail in Ref. 56

method derived from Reverse Monte Carlo (RMC).[176] Based on the Monte Carlo approach, EPSR iteratively refines an atomistic simulation until maximum consistency with experimental data is achieved. To use the method effectively, one typically needs substantial prior knowledge of the system, including its composition, density, and molecular geometry, and correct assumptions are needed to avoid non-physical results.

An EPSR simulation begins with the construction of a simulation box with the correct density and intramolecular structure. The density is specified in atoms/Å^3 to ensure a consistent value independent of the isotope composition. The intramolecular geometry is defined through general harmonic force constants for bonds between atom pairs, together with bond angle and dihedral angle terms. These force constants are deliberately simple, depending on a single general parameter weighted by the equilibrium distance and reduced mass of the atom pair, which allows for a broad range of molecular species to be treated without requiring a full force field specification.[177] Intermolecular interactions are governed by a Lennard-Jones (LJ) potential combined with a Coulomb potential. The Lennard-Jones parameters σ and ε are defined as self-interaction parameters for each atom type, describing interactions between identical atom types $(i - i)$. Parameters for interactions between different atom types $(i - j)$ were generated using the Lorentz-Berthelot combination rules:

$$\sigma_{ij} = \frac{\sigma_i + \sigma_j}{2} \qquad \text{and} \qquad \varepsilon_{ij} = \sqrt{\varepsilon_i \varepsilon_j}. \tag{3.21}$$

Together, these terms constitute the reference potential (RP). Once the RP is defined, the potential energy of the system is minimised using the Metropolis Monte Carlo method, in which random translations, rotations and intramolecular shakes are performed independently of the surrounding molecular environment. It is only the intramolecular energy that is considered when accepting or rejecting these moves. For each proposed move, the change in potential energy is calculated as

$$\Delta U = U_{\text{after}} - U_{\text{before}}, \tag{3.22}$$

where if $\Delta U < 0$ the move is accepted; otherwise, the move is accepted with a probability of $\exp(-\Delta U/kT)$. Once the system has equilibrated under the RP, the $g(r)$s are calculated and Fourier transformed to obtain the simulated $S_{\text{calc}}(Q)$. The difference between the experimentally obtained structure factor, $S_{\text{exp}}(Q)$, and the simulated $S_{\text{calc}}(Q)$ is then used to calculate the empirical potential (EP), which is added to the RP. The process is iterated from the energy minimisation step until the EP converges to a stable form, at which point the simulation is considered to be consistent with the experimental data. More detailed information about EPSR can be found in the EPSR manual.[178]

Dissolve[177] is a successor code to EPSR that implements the same core empirical potential refinement methodology but has been redesigned to address several limitations of EPSR. While the fundamental procedure remains the same, there are several important differences, such as the treatment of the force field. In contrast to EPSR, Dissolve employs a full classical force field, providing proper harmonic bond and angle potentials as well as torsional terms. This makes Dissolve better suited for the treatment of large and flexible molecules, such as proteins. Furthermore, Dissolve offers substantially improved scalability. While EPSR is limited to approximately $2 \cdot 10^5$ atoms, Dissolve can handle systems of up to $3 \cdot 10^6$ atoms, which is essential for modelling complex systems such as proteins in solution. A more detailed description of Dissolve and how it compares to EPSR can be found in Ref. 177.

The atomistic model of the protein-sugar-water systems studied in paper I utilised the EPSR method. The myoglobin structure (PDB ID: 1DWR[101]) was obtained from the protein data bank (PDB) and the water and sugar molecules were created using Jmol.[179] The SPC/E force field was used for the water molecules[180] and the OPLS-AA force field for the sugar molecules.[181] The reference potential for the protein was based on the OPLS-AA force field[101] with some modifications. Atoms of the same element were grouped together and assigned force field parameters accordingly.

In papers II and VI, Dissolve modelling was used. The simulation box was created in the Dissolve GUI by adding the molecules included in the system and applying parameters such as temperature and density. The structure of myoglobin, which was used in paper II, was the same as that used for the EPSR model in paper I. However, a more detailed version of the force field was implemented. Dissolve allows for all atoms to have individual charges, which creates a more realistic description of the protein. For the water molecules, the SPC/Fw[182] was used and for the disaccharides the same OPLS-AA force field as that used in the EPSR modelling was used. The structure of the HEWL molecule studied in paper VI was obtained from the protein data bank (PDB ID: 1LYZ[102]).

3.1.4.3 Coordination Numbers

The coordination number, $N_{\alpha\beta}(r_1,r_2)$, provides information regarding how many atoms of type β surround atom of type α within an interval $r_1 \leq r \leq r_2$. It is typically given by[57]

$$N_{\alpha\beta}(r_1,r_2) = 4\pi\rho c_\beta \int_{r_1}^{r_2} r^2 g_{\alpha\beta}(r) dr, \tag{3.23}$$

where c_β is the atomic number density of atom β and $g_{\alpha\beta}(r)$ is the partial pair correlation function. Coordination numbers can be obtained for each peak in $g_{\alpha\beta}(r)$ by integrating over the peak areas. The first coordination shell is from $r_1 = 0$ Å to r_2, where r_2 is defined as the position of the first minimum point after the first peak. The coordination numbers presented in papers I, II and VI were calculated from the EPSR or Dissolve produced models using the VMD software.[183]

3.1.4.4 Hydrogen Bonding

The structure and properties of many biological molecules, as well as water, are to a large extent determined by hydrogen bonding. A hydrogen bond is the interaction between a hydrogen atom covalently bonded to a donor atom (D) and a pair of non-bonded electrons of an acceptor atom (A). Figure 3.4 illustrates hydrogen bonding between water molecules, where r_{OO} and θ_{DHA} denote the distance and angle between the donor and acceptor oxygen atoms.

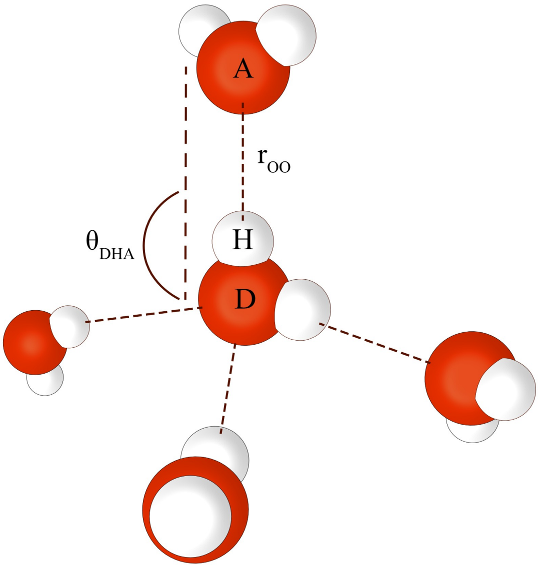

Figure 3.4: Hydrogen bonding between water molecules. A stands for acceptor, H for hydrogen and D for donor. The figure illustrates the bond length, r_{OO}, and the angle, θ_{DHA}, between the donor and acceptor oxygens of water.

Hydrogen bonds are directional interactions and their identification therefore requires more than the spatial restriction used for coordination numbers. By adding an angular restriction between the donor and acceptor atoms, it is possible to identify hydrogen bonds and characterise their strength.

In paper II, the number of hydrogen bonds between the oxygen atoms on the surface of the protein and the oxygens in either water or trehalose was calculated using the VMD software.[183] As with the coordination numbers, a spatial restriction of $r_{OO} < 3.4$ Å was applied. In addition, an angular restriction of $\theta_{DHA} \geq 120°$ was imposed, meaning that relatively weak hydrogen bonds were also included.

3.1.5 Quasielastic Neutron Scattering (QENS)

In this thesis, the main focus has been to investigate the stabilising and anti-aggregating effect disaccharides have on proteins in aqueous solutions. In such systems the presence of water is extremely important as it induces translational and rotational motions within the biological macromolecules. One of the advantages with neutrons is that they can be used to study both the structure and dynamics of materials with atomic resolution. As mentioned in section 3.1.2, the inelastic part ($\Delta E \neq 0$) of the scattering provides information about the dynamics of the atoms. In Figure 3.5, the scattering function as a function of energy transfer is shown. The difference between elastic and inelastic scattering is clear as elastic scattering is seen as a very sharp peak around $\hbar\omega = 0$ while inelastic scattering is seen as peaks at the respective energy transfer. The broadening of the peak around $\hbar\omega = 0$ is referred to as quasielastic scattering. The low energy transfers that are measured in a QENS experiment are related to relatively slow atomic motions such as rotations and translations. The resulting energy transfer is related to a frequency shift according to de Broglie equation expressed in eqn. (3.2).

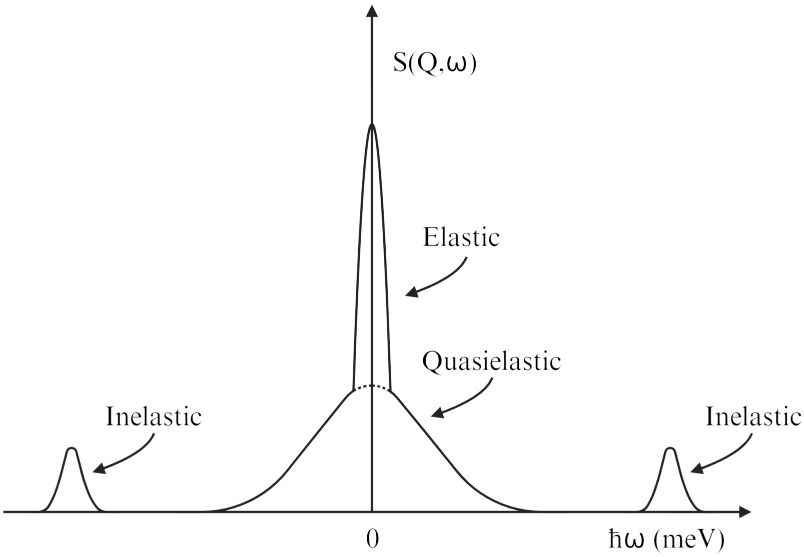

Figure 3.5: The scattering function as a function of energy transfer. The smaller peaks $\hbar\omega \neq 0$ are the inelastic scattering, the sharp peak around $\hbar\omega = 0$ is the elastic scattering, and the broadeing of the latter is the quasielastic scattering.

The theory behind QENS is very similar to the case of elastic neutron scattering described in section 3.1.4. However, the positions of the atoms are now time-dependent and the energy transfer is not zero, resulting in a double differential scattering cross section given by[184]

$$\frac{d^2\sigma}{d\Omega dE} = \frac{1}{\hbar}\frac{d^2\sigma}{d\Omega d\omega} = \frac{k'}{k}\frac{1}{2\pi}\int_0^{\infty} e^{-i\omega t}\sum_{i,j}^{N}\langle b_i b_j^*\rangle e^{i\mathbf{Q}\cdot(\mathbf{r}_i(0)-\mathbf{r}_j(t))}dt, \tag{3.24}$$

which can be divided into coherent and incoherent scattering

$$\begin{aligned}\frac{d^2\sigma}{d\Omega dE} &= \underbrace{\frac{k'}{k}\frac{1}{2\pi}\langle b\rangle^2\int_0^\infty e^{-i\omega t}\sum_{i,j}^{N} e^{i\mathbf{Q}\cdot(\mathbf{r}_i(0)-\mathbf{r}_j(t))}dt}_{\text{Coherent scattering}} \\ &\quad \underbrace{+\frac{k'}{k}\frac{1}{2\pi}(\langle b^2\rangle-\langle b\rangle^2)\int_0^\infty e^{-i\omega t}\sum_{i}^{N} e^{i\mathbf{Q}\cdot(\mathbf{r}_i(0)-\mathbf{r}_i(t))}dt,}_{\text{Incoherent scattering}}\end{aligned} \tag{3.25}$$

where the latter corresponds to a pure self-scattering part. Similarly to the elastic case, described in section 3.1.4, $S^{\mathrm{coh}}(\mathbf{Q},\omega) = \frac{1}{N}\int_0^\infty e^{-i\omega t}\sum_{i,j}^N e^{i\mathbf{Q}\cdot(\mathbf{r}_i(0)-\mathbf{r}_j(t))}dt$ and $S^{\mathrm{inc}}(\mathbf{Q},\omega) = \frac{1}{N}\int_0^\infty e^{-i\omega t}\sum_{i}^N e^{i\mathbf{Q}\cdot(\mathbf{r}_i(0)-\mathbf{r}_i(t))}dt$, which enables division of the double differential scattering cross section into

$$\frac{d^2\sigma^{\mathrm{coh}}}{d\Omega dE} = \frac{k'}{k}\frac{N}{2\pi}\langle b\rangle^2 S^{\mathrm{coh}}(\mathbf{Q},\omega) \tag{3.26}$$

and

$$\frac{d^2\sigma^{\mathrm{inc}}}{d\Omega dE} = \frac{k'}{k}\frac{N}{2\pi}((\langle b^2\rangle-\langle b\rangle)^2)S^{\mathrm{inc}}(\mathbf{Q},\omega). \tag{3.27}$$

In section 3.1.4 the particles were assumed to be static when discussing the correlation function. However, to understand the dynamics of particles, it is often useful to include the displacements over time, which is done in the dynamic pair correlation function presented in section 2.1.2. Using a general property of the Dirac delta function ($\sum_i e^{i\mathbf{Q}\cdot\mathbf{r}_i} = \int_V e^{i\mathbf{Q}\cdot\mathbf{r}_i}\sum_i \delta(\mathbf{r}-\mathbf{r}_i)$) and eqns. (2.6) and (2.7), the dynamic structure factors can be divided into

$$\begin{aligned}S^{\mathrm{coh}}(\mathbf{Q},\omega) &= \int_0^\infty \sum_{i,j}^N e^{i(\mathbf{Q}\cdot(\mathbf{r}_i(0)-\mathbf{r}_j(t))-\omega t)}dt \\ &= \int_0^\infty\int_{-\infty}^\infty e^{i(\mathbf{Q}\cdot(\mathbf{r}_i(0)-\mathbf{r}_j(t))-\omega t)}G(\mathbf{r},t)d\mathbf{r}dt\end{aligned} \tag{3.28}$$

and

$$\begin{aligned}S^{\mathrm{inc}}(\mathbf{Q},\omega) &= \int_0^\infty \sum_{i}^N e^{i(\mathbf{Q}\cdot(\mathbf{r}_i(0)-\mathbf{r}_i(t))-\omega t)}dt \\ &= \int_0^\infty\int_{-\infty}^\infty e^{i(\mathbf{Q}\cdot(\mathbf{r}_i(0)-\mathbf{r}_i(t))-\omega t)}G_{\mathrm{s}}(\mathbf{r},t)d\mathbf{r}dt.\end{aligned} \tag{3.29}$$

$S^{\mathrm{coh}}(\mathbf{Q},\omega)$ and $S^{\mathrm{inc}}(\mathbf{Q},\omega)$ are the coherent and incoherent dynamic structure factors related to the total dynamic pair correlation function[f] and the dynamic self-correlation

---

[f] The total pair correlation function ($G(\mathbf{r},t)$) includes both the self-correlation and the distinct part.

function, respectively, through Fourier transformation.

QENS was used in papers I and II to examine solvent dynamics. The QENS measurements were performed at 300 K using the IRIS spectrometer[185] at the neutron spallation source, ISIS. To be able to extract the dynamics of the water, sugar, and protein molecules separately, isotope substitution was utilised. The following systems were studied: myoglobin/D-sugar/H_2O, myoglobin/H-sugar/H_2O and myoglobin/H-sugar/D_2O. Due to the incoherent scattering cross section of hydrogen being about 40 times larger than that of deuterium, myoglobin/D-sugar/H_2O mostly displays dynamics of water molecules whereas myoglobin/H-sugar/D_2O mostly represents the dynamics of myoglobin and sugar. The following four reference systems were also prepared: myoglobin in D_2O, myoglobin in H_2O, H-sugar in D_2O, and D-sugar in H_2O. The samples were placed in annular aluminium alloy cans providing a sample thickness of 0.1 or 0.25 mm[g]. All data corrections were performed using the Mantid software package.[186]

3.1.5.1 Analysis of the QENS Data

QENS is obtained from the broadening of the scattering function as a function of the energy transfer. Therefore, in the analysis of QENS one looks at the broadening and how it depends on Q. By Fourier transforming the scattering function in the time domain, the intermediate scattering signal, $I(Q,t)$, can be obtained, which is what has mainly been analysed in this work.

The dynamics of atoms in a system can be described by a number of different models, where one example is the use of a stretched exponential function also referred to as the Kohlrausch-William-Watts (KWW) function[187]

$$I_i(Q,t) = A_i \cdot e^{((-\frac{t}{\tau_i})^{\beta_i})}, \tag{3.30}$$

where A^i is the scattering contribution from atom type i to the total scattering, τ_i is the typical relaxation time, and β_i ($0 < \beta_i < 1$) is the stretching parameter. Low values of β_i means that the atoms have a large distribution of relaxation times. In contrast, $\beta = 1$ turns eqn. (3.30) into a simple exponential, which implies that all atoms of type i have the same relaxation time. Which relaxation time corresponds to which atom type can be determined by the use of isotope substitution of hydrogen for deuterium. As previously mentioned, hydrogen has a significantly larger scattering cross section compared to deuterium, which makes it possible to "filter out" for example the fast dynamics of water by replacing the H_2O by D_2O.

To calculate the diffusion constants, D_s, presented in papers I and II, the following fitting procedure was performed. The three isotope compositions ($I^1(Q,t)$, $I^2(Q,t)$, and $I^3(Q,t)$) were fitted simultaneously by solving the non-linear equation system

---

[g] The thickness depends on the hydrogen content of the sample to ensure less than 10% scattering from the sample

$$\begin{bmatrix} A_P^1 & A_S^1 & A_W^1 \\ A_P^2 & A_S^2 & A_W^2 \\ A_P^3 & A_S^3 & A_W^3 \end{bmatrix} \cdot \begin{bmatrix} e^{-(t/\tau_P)^{\beta_P}} \\ e^{-(t/\tau_S)^{\beta_S}} \\ e^{-(t/\tau_W)^{\beta_W}} \end{bmatrix} = \begin{bmatrix} I^1(Q,t) \\ I^2(Q,t) \\ I^3(Q,t) \end{bmatrix}, \tag{3.31}$$

where P, S, and W stand for protein, sugar, and water, respectively. The superscripts (1, 2, and 3) represent the three isotope compositions. The A^i of each component was fixed to its relative contribution to the total incoherent scattering cross section[h]. τ and β are the relaxation time and stretching parameter of each molecular component. The average relaxation times were calculated using

$$\langle \tau \rangle = \frac{\tau}{\beta} \Gamma \left(\frac{1}{\beta} \right), \tag{3.32}$$

where Γ is the gamma function. At low Q values the translational dynamics exhibit a Q^2-dependence (i.e. $1/\langle \tau \rangle \propto Q^2$). However, sometimes at higher Q-values, a considerable deviation from the linearity can be observed. Hence, the Q^2-dependence of $\langle \tau \rangle$ was fitted using a Gaussian jump-diffusion model[188]

$$\frac{1}{\tau} = \frac{1}{\tau_{\mathrm{res}}} \left[1 - exp \left(\frac{Q^2 \langle r^2 \rangle}{6} \right) \right], \tag{3.33}$$

where τ_{res} is the average residence time between two consecutive jumps of the moving atoms and $\langle r^2 \rangle$ is the mean square jump length. These two parameters can be used to calculate the self-diffusion constant[188] through

$$D_{\mathrm{s}} = \frac{\langle r^2 \rangle}{6\tau_{\mathrm{res}}}. \tag{3.34}$$

3.1.6 Neutron Spin Echo (NSE) Spectroscopy

Neutron spin echo (NSE) enables the observation of slow dynamics on the nanosecond to microsecond timescale, making it well suited for studying phenomena such as polymer motion, protein domain dynamics, diffusion, and relaxation processes.

In conventional neutron spectroscopy, energy changes are measured by comparing the velocities of the incoming and scattered neutrons, and the energy resolution is linked to the precision of these velocities. To achieve higher energy resolution, neutrons with unwanted velocities must be filtered out. As a consequence, very few neutrons remain at high energy resolutions, making QENS poorly suited for studying slower dynamics. In contrast, in NSE the energy resolution is not limited by the beam monochromatisation. Instead, each neutron's velocity is encoded in its spin through Larmor precession, so that all neutrons in the beam contribute to the measurement regardless of their velocity.

---

[h] These values can be found in Table S3 in the SI of papers I and II.

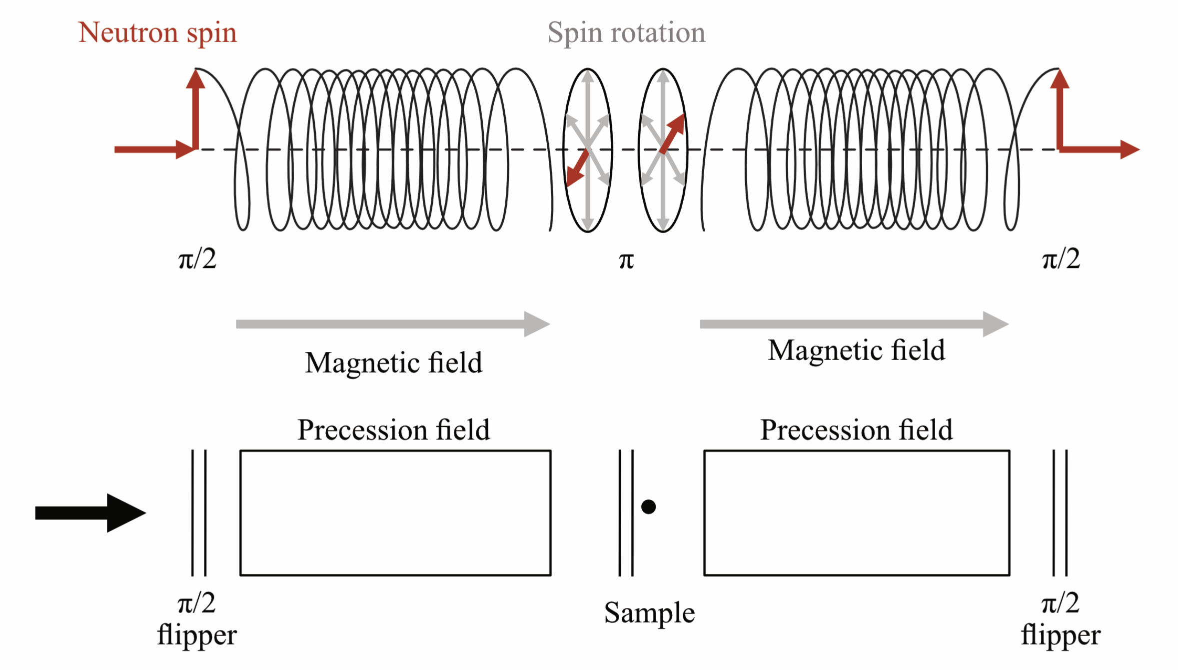

Figure 3.6: Schematic illustration of the NSE spectrometer. The upper part shows the neutron spin orientation at each stage: a $\pi/2$-rotation before entering the first precession field, a π-rotation near the sample, and a second precession field followed by a $\pi/2$-rotation. The lower part shows the instrument layout.

In NSE, a beam of longitudinally polarised neutrons passes through a $\pi/2$-flipper, which rotates all spins to be perpendicular to the direction of the neutron beam, which is illustrated in Figure 3.6 as a red arrow pointing upwards. The neutrons then enter a magnetic field where their spins precess around the field direction at the Larmor frequency, ω_L. The total precession angle is inversely proportional to the velocity of the neutron, which means that each individual neutron carries a velocity tag encoded in its spin orientation. The Larmor precession angle, ϕ, is proportional to the time the neutron spends in the field and is related to the neutron velocity through:

$$\phi = \frac{\gamma H l}{v}, \tag{3.35}$$

where γ is the Larmor constant, H is the average strength of the magnetic field of length l between the $\pi/2$- and π-flipper. Near the sample, a π-flipper rotates the spins by 180°, effectively reversing the sense of accumulated precession, which results in ϕ turning into $-\phi$. After scattering, the neutrons pass through a second magnetic field that is symmetric to the first. This adds another precession angle ϕ' according to

$$-\phi + \phi' = -\frac{\gamma H l}{v} + \frac{\gamma H' l'}{v'}, \tag{3.36}$$

where H' is the average strength of the magnetic field of length l' between the π- and the second $\pi/2$-flipper. If a neutron's velocity is unchanged by the sample (elastic scattering), the precession in the second field exactly cancels that from the first, and all spins return to their original orientation (this is the spin echo). However, if the sample changes a neutron's velocity slightly (quasielastic scattering), the precession in the two fields does not cancel, and the final spin orientation differs from the initial one. If one assumes that the velocity change is small and $Hl = H'l'$, the change of the neutron's energy can be obtained through

$$-\phi + \phi' = \gamma Hl \left(\frac{1}{v'} - \frac{1}{v} \right) \approx \gamma Hl \frac{1}{v}(v' - v) \approx \frac{\gamma H'l'}{mv^3} \hbar\omega = t\omega, \tag{3.37}$$

where t is the Fourier time. A second $\pi/2$-flipper then rotates the spins back into the longitudinal direction, and an analyser transmits only neutrons with a specific spin orientation to the detector.

At the detector, it is the polarisation that is measured, which is the ensemble average over all detected neutrons. The analyser selects one component of the neutron spin, for example x, which corresponds to the cosine of the net precession angle

$$P_x = \langle \cos(-\phi + \phi') \rangle = \left\langle \cos\left(\frac{\gamma H'l'}{mv^3} \hbar\omega \right) \right\rangle. \tag{3.38}$$

This is the average over all ω, weighted by the probability that a neutron scatters with that particular ω, which is described by $S(\mathbf{Q},\omega)$. By using eqns. (3.37) and (3.38), P_x can be written in terms of $S(\mathbf{Q},\omega)$:

$$P_x = \frac{\int S(\mathbf{Q},\omega) \cos(\omega t) d\omega}{\int S(\mathbf{Q},\omega) d\omega}, \tag{3.39}$$

where the numerator is the cosine Fourier transform of $S(\mathbf{Q},\omega)$, which is the real part of the intermediate scattering function, $I(\mathbf{Q},t)$, and the denominator is the static structure factor, $S(\mathbf{Q})$. Thus, the quantity directly measured in a NSE experiment is the normalised intermediate scattering function, $S(\mathbf{Q},t)/S(\mathbf{Q},0)$. For a more detailed description of the working principles of NSE the reader is referred to Refs. 150, 189, 190.

In paper V, NSE was used to study the dynamics of HEWL monomers and fibrils in solution. The measurements were performed at 310 K with a Q range of 0.021–0.217 Å^{-1}, using the IN15 spectrometer at the Institut Laue-Langevin (ILL),[191] Grenoble, France. The dynamics of the protein was measured in D_2O with isotope substitution of the exchangeable hydrogens of the protein. This was done to suppress the incoherent scattering from hydrogen and enhance the coherent signal from the protein. The monomers were measured using a quartz cuvette and the fibrils were placed between two glass slides separated by a spacer. Both sample holders provided a sample thickness of 2 mm.

3.1.6.1 Analysis of the NSE Spectroscopy Data

The background signal was first subtracted from the output. The obtained structure factors were then normalised according to $I(Q,t) = S(Q,t)/S(Q,0)$. Similarly to the fitting of the $I(Q,t)$ obtained by QENS, the normalised $I(Q,t)$ were fitted using a stretched exponential

$$I(Q,t) = A \cdot e^{-(t/\tau)^{\beta}}, \tag{3.40}$$

where $A = 1$ is the amplitude. The average relaxation time was calculated in the same manner as for QENS (see eqn. (3.32)). A model describing Fickian diffusion was used to calculate the diffusion constant

$$D_s = \frac{1}{\langle\tau\rangle Q^2}. \tag{3.41}$$

3.1.7 X-ray Scattering

To probe different Q-ranges the scattering angle to the detector and/or the detector distance relative to the sample can be adjusted. Placing the detector far away results in a smaller scattering vector and information on relatively large structures can be gained. This also results in scattering at small angles (typically 0.1–10°) and is referred to as small-angle X-ray scattering (SAXS). By the use of SAXS, structural information of materials can be obtained and studied on a nanometre scale. By moving the detector closer to the sample, scattering at wider angles (typically $> 10°$) can be analysed. This method is commonly referred to as wide-angle X-ray scattering (WAXS) and can be used to gain information regarding distances as small as those within amyloid fibrils. Figure 3.7 shows an illustration of the difference between SAXS and WAXS.

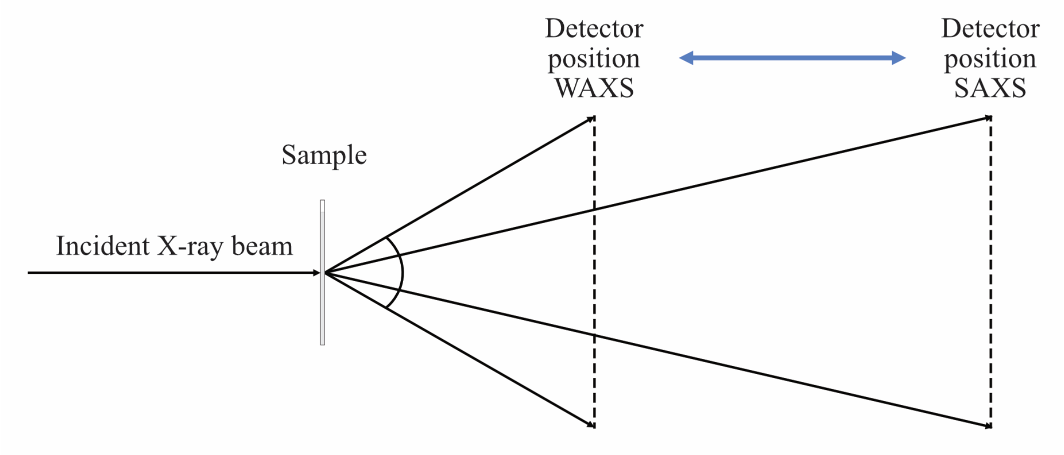

Figure 3.7: Schematic illustration of the difference in detector position between SAXS and WAXS.

As mentioned in section 3.1.2, the scattering behaviour of X-rays can be explained by Bragg's law (see eqn. (3.3)). Like neutron diffraction, the diffraction peaks correspond to repeated distances in the material. The wave vector can be related to real-space distances by combining $\mathbf{Q} = \mathbf{k}_i - \mathbf{k}_f$ and eqn. (3.3), which results in $Q = 2\pi/d$, where d is the distance between repeated structures in the material.[170] SAXS can also be used to obtain information regarding the shape and size of macromolecules, such as proteins or structural entities, in a system.[192]

In paper III, the inhibitory effect of trehalose and sucrose on fibril formation of HEWL was investigated, where SAXS and WAXS were used to examine the inter- and intramolecular distances of the aggregates, respectively. Similarly, SAXS and WAXS were used to structurally characterise the systems in paper V. The measurements took place at Chalmers Materials Analysis Laboratory (CMAL) using the Mat: Nordic SAXS/WAXS/GISAXS instrument (SAXSLAB) at room temperature. The exposure time was 15 min/sample over a Q-range of 0.0138–0.30659 Å^{-1} and 5–10 min/sample over a Q-range of 0.0386–2.2827 Å^{-1} for SAXS and WAXS, respectively, with an X-ray wavelength of $\lambda = 1.54$ Å. The samples in paper III were placed in quartz capillaries with a thickness of 1.5 mm. In paper V, the samples were measured using a sandwich holder.

3.2 Molecular Dynamics (MD) Simulations

The modelling methods EPSR and Dissolve, described in section 3.1.4.2, are excellent tools for analysing the structural arrangement of experimentally measured systems. However, the primary focus of these methods is structural refinement and may not provide insights into the dynamic behaviours of systems over time. Additionally, the high-quality experimental data required for EPSR may not always be feasible to obtain. To complement EPSR and gain a deeper understanding of the dynamics of a molecular system, theoretical models are indispensable. One such powerful method is classical MD simulations. The first molecular dynamics simulation was performed in 1957 to study the properties of hard sphere fluids.[193] However, MD simulations can be used in a number of different areas. In this thesis, MD simulations have been used to study the dynamics of aqueous solutions containing sucrose and trehalose. This section offers a concise introduction to the basic principles of classical MD simulations.

To perform MD simulations one first needs to create an initial state of the system, the simulation box. In the initial state, the initial atomic positions and velocities as well as the types of particles in the system need to be defined. For a sufficiently simple system this step can be done manually. Once the initial state is defined, interaction potentials between the particles in the system need to be introduced. This is done by the use of existing force fields. There are many different force fields that are used for different types of particles and purposes. Some examples are the general amber force field (GAFF)[194] and the chemistry at harvard macromolecular mechanics force field (CHARMM36),[195–197] which were used in paper I to perform MD simulations on the carbohydrates and the protein, respectively. The force fields are commonly based on a sum of interatomic potentials, where the total potential is a sum of the intra- and intermolecular potentials and can be expressed as

$$\begin{aligned} U_i = \sum k_i^{\text{bond}}(r_i - r_0)^2 + \sum k_i^{\text{angle}}(\theta_i - \theta_0)^2 + \sum k_i^{\text{dihedral}}(1 + cos(n_i\phi_i + \delta_i)) \\ + \sum_i \sum_{j\neq i} 4\varepsilon_{i,j} \left[\left(\frac{\sigma_{i,j}}{r_{i,j}} \right)^{12} + \left(\frac{\sigma_{i,j}}{r_{i,j}} \right)^{6} \right] + \sum_i \sum_{j\neq i} \frac{q_i q_j}{4\pi\varepsilon_0 r_{i,j}}, \end{aligned} \tag{3.42}$$

where the first term provides the potential energy corresponding to the variation in bond length between two bonded atoms in which k_i^{bond} is a specific bond strength and r_0 is the atom position at equilibrium. The second term corresponds to the variation of the bond angle within a molecule, where θ_0 is preferred with the strength k_i^{angle}. For larger molecules (more than four atoms) the third term is also included. It corresponds to the torsion potential where ϕ_i is the torsion angle for atom i, n_i is the number of potential minima the torsion angle can reside in, and δ_i is the phase. These three terms correspond to the potential energy of the bonded atoms.[198] The two final terms correspond to the potential energy of the non-bonded atoms, where the fourth term, known as the Lennard-Jones (LJ) potential, approximates the forces between non-bonded atoms. This term combines the repulsive effect originating from the Pauli exclusion principle, with the attractive van der Waals force. In this context, $\sigma_{i,j}$ represents the equilibrium distance between atoms i and j, and $\epsilon_{i,j}$ is the depth of the potential energy-well at that distance. The fifth and final term relates to the Coloumb-interactions between two atoms with charges q_i and q_j separated by a distance of $r_{i,j}$. Finally, by solving Newton's equations for motion

$$m_i \frac{d^2\mathbf{r}_i}{dt^2} = \mathbf{F}_i = -\nabla U, \tag{3.43}$$

where m_i and r_i are the mass and position of atom i, $\mathbf{F}_i$ is the force on atom i, and U is the potential energy, the position and velocity of each atom as a function of time can be determined. The movement of the particles can be simulated by the use of a number of algorithms, where the most simple one is the Verlet algorithm.

3.3 Differential Scanning Calorimetry (DSC)

When the temperature of a material changes, it undergoes both physical and chemical transformations, which may be either endothermic or exothermic. Processes such as crystallisation, glass transition, melting, and protein denaturation are examples of such changes. Differential scanning calorimetry (DSC) is a widely-used technique to study these thermal behaviours, as demonstrated in papers III and IV.

During DSC measurements, the sample and a reference (typically an empty sample holder) is heated or cooled at a constant rate (°C/min). Both are placed in identical, hermetically sealed aluminium pans on separate platforms within the DSC cell. The sample and reference are heated or cooled via their respective thermoelectric disk, which would result in a difference in temperature due to the heat capacity (C_p) of the sample. This difference is detected by thermocouples and is related to the heat flow via Ohm's law, $q = \Delta T/R$, where q is the sample heat flow, ΔT the difference in temperature between the sample and reference, and R is the resistance in the thermoelectric disk.[199] The difference in temperature corresponds to the energy required to change the temperature of the sample. The working principles of DSC are shown in Figure 3.8.

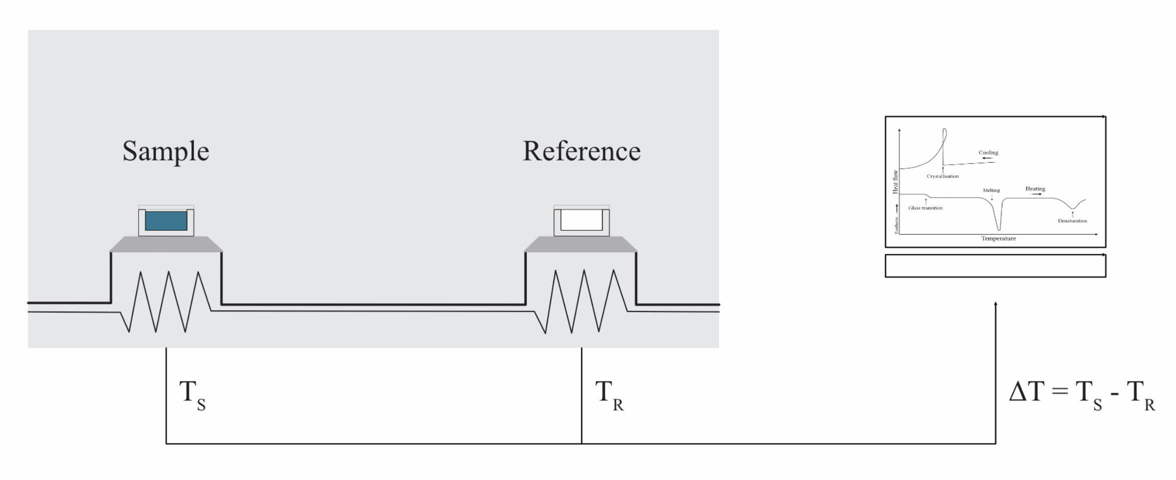

Figure 3.8: The working principles of DSC displaying the sample and reference pans placed on separate thermoelectric disks in the DSC cell. The difference in temperature between the sample and reference is transferred to the computer for analysis.

When no thermal transitions are occurring, the DSC heat flow signal remains approximately constant, producing a flat baseline. However, exothermic and endothermic processes cause deviations that produce distinct features on the DSC curve, as illustrated in Figure 3.9. Biological systems usually contain a significant amount of water, whose crystallisation during cooling appears as a pronounced exothermic peak. The crystallisation temperature, T_c, is extrapolated from the onset of this peak. Both the peak intensity and T_c may vary with the cooling rate. Conversely, melting of a crystallised sample is an endothermic process that requires energy to disrupt the crystal structure and appears as a dip in the curve upon heating. The glass transition is observed as a step in the DSC curve during heating, where T_g can be obtained from the onset point or the midpoint of the step. Heat-induced protein denaturation produces an endothermic dip, with T_den obtained from the position of the dip minimum.

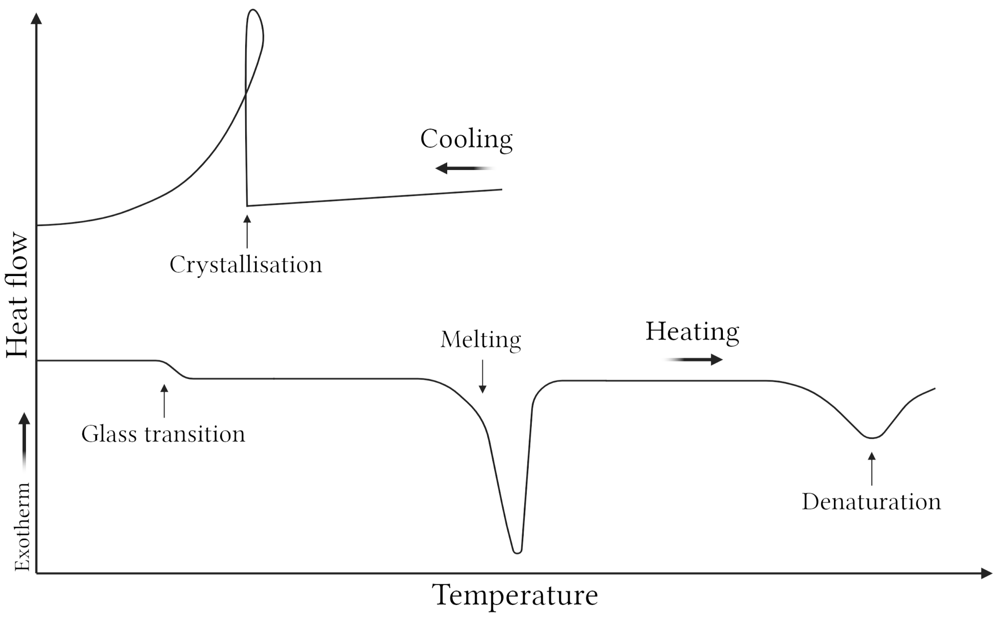

Figure 3.9: Schematic image of a typical DSC curve showing the heat flow as a function of temperature. The crystallisation is seen as an exotherm peak during the cooling process. The glass transition is seen as a step during heating, while both the melting and the protein denaturation are seen as endothermal dips.

The calorimetric measurements in papers III and IV were performed using a DSC Q2000 (TA Instruments). The instrument is equipped with a liquid nitrogen cooling system (LNCS) and a thermal element, enabling cooling to -180 °C and heating to 550 °C. The sample was placed in a hermetic aluminium pan, sealed using a sealing press. The weights of both the sample and pan were recorded using a balance (Precisica 262SMA-FR) with a precision of 0.01 mg. The measurement of the crystallisation, glass transition and protein denaturation was performed as described in papers III and IV.

The instrument was calibrated to optimise its performance for a specific temperature range and the utilised heating and cooling rates. The primary Tzero calibration sequence involved setting a baseline for calculating the time constants and capacitances of both the sample and reference sensors, utilising a sapphire[i] standard for accuracy. Following this, a three-point calibration was executed using indium, mercury, and MQ water. Finally, the calibration of heat capacity was conducted using a Temperature Modulated Differential Scanning Calorimetry (TM-DSC) approach, again employing a sapphire standard reference.

---

[i] The heat capacity of sapphire is well-known and stable.

3.4 Dielectric Spectroscopy (DS)

A material contains charges that respond to an applied electric field, including electrons bound to nuclei, ions in a lattice, permanent molecular dipoles, and mobile charge carriers. The applied electric field displaces or reorients these charges, producing a net polarisation of the material. Different types of charges respond on very different timescales, and dielectric spectroscopy (DS) exploits this separation of timescales by probing the material's response over a broad frequency range. In a DS experiment, the sample is placed between two electrodes (forming a capacitor), and subjected to an AC voltage, so that by varying the frequency one can selectively probe individual polarisation mechanisms. In addition, varying the temperature reveals how the dynamics of each process varies with temperature. This combination of broad frequency and temperature ranges makes DS a versatile tool for studying dynamics as diverse as the rotation of protein side groups, charge transport, and molecular motions.[200]

An electromagnetic wave propagates through vacuum with constant velocity and amplitude, but in a material both are reduced. The response is captured by the complex permittivity, ε^*, of the material. Measuring the phase shift and loss in amplitude of the wave relative to vacuum therefore provides information on how the medium responds to an external electric field. When an external field, $\mathbf{E}$, is applied to a material placed between two electrodes, it induces a polarisation, $\mathbf{P}$, giving rise to the electric displacement field

$$\mathbf{D} = \varepsilon_0 \mathbf{E} + \mathbf{P} = \varepsilon_r \varepsilon_0 \mathbf{E}, \tag{3.44}$$

where $\varepsilon_0 = 8.85 \cdot 10^{-12}$ As/Vm is the permittivity of vacuum and ε_r is the permittivity (dielectric constant) of the material. For a harmonic field $E = E_0 \exp(i\omega t)$, the dipoles in the material oscillate along the field direction, producing a displacement field,

$$D = D_0 \exp(i(\omega t - \delta(\omega))), \tag{3.45}$$

where the amplitude D_0 and the phase shift $\delta(\omega)$ depend on the properties of the material. The complex permittivity can then be described as

$$\varepsilon^*(\omega) = \varepsilon'(\omega) - i\varepsilon''(\omega) = \frac{D(\omega)}{\varepsilon_0 E(\omega)} = \frac{D_0(\omega)}{\varepsilon_0 E_0} \exp(-i\delta(\omega)), \tag{3.46}$$

where ε' is the real part of the permittivity and describes how much energy is stored in the material and ε'' is the complex part of the permittivity and describes how energy is lost and dissipated in the material.[200,201]

In practice, $\mathbf{D}$ and $\mathbf{E}$ are not measured directly. Instead, the sample is treated as a dielectric of a parallel plate capacitor of area, A, and plate separation, d, and the current response, $I^*(\omega)$, to the applied voltage, $U^*(\omega)$, is recorded. A basic representation of the principle can be seen in Figure 3.10.

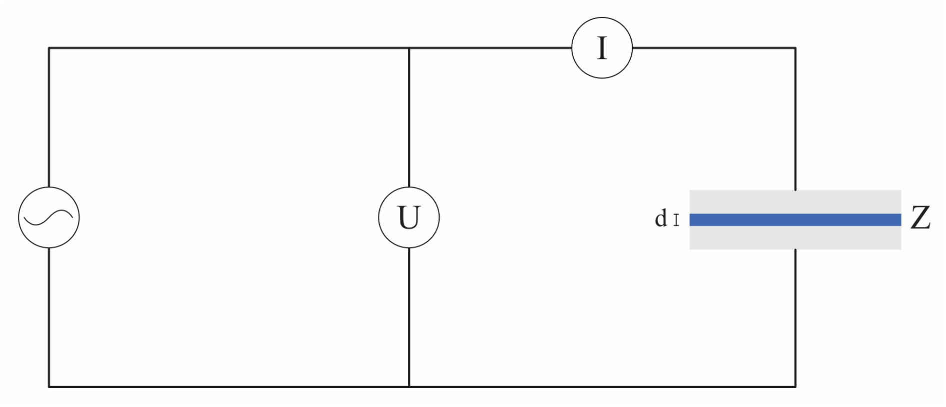

Figure 3.10: Simplified illustration of the electrical circuit of a DS setup. The sample is shown in blue, placed between two electrodes shown in gray.

The complex impedance follows from Ohm's law, $Z^* = U^*/I^*$, from which the complex permittivity is obtained as

$$\varepsilon^*(\omega) = \frac{1}{i\omega Z^*(\omega)} \cdot \frac{d}{\varepsilon_0 A}. \tag{3.47}$$

If the applied electric field is suddenly switched off there is a certain time it takes for the dipoles to respond and relax into their original random orientations. This relaxation time, τ, is dependent on the local environment of the individual dipoles. The frequency dependence of the complex permittivity of a material exhibiting a single relaxation process with a defined relaxation time is given by the Debye function

$$\varepsilon^*(\omega) = \varepsilon_\infty + \frac{\Delta\varepsilon}{1 + i\omega\tau}, \tag{3.48}$$

where ε_∞ is the high-frequency permittivity, $\Delta\varepsilon$ the amplitude of a specific dipole relaxation and τ is the characteristic relaxation time. The real, $\varepsilon'(\omega)$ and imaginary, $\varepsilon''(\omega)$ parts are described by:

$$\varepsilon'(\omega) = \varepsilon_\infty + \Delta\varepsilon \frac{1}{1 + \omega^2\tau_D^2}, \tag{3.49}$$

and

$$\varepsilon''(\omega) = \Delta\varepsilon \frac{\omega\tau_D}{1 + \omega^2\tau_D^2}, \tag{3.50}$$

respectively. The Debye model is the most simple model to describe the relaxation process. However, for many glass forming materials the Debye model is not ideal and thus many other empirical models have been developed such as Cole-Cole,[202] Cole-Davidson,[203] and Havriliak-Negami (HN).[204] The HN function,

$$\varepsilon^*(\omega) = \varepsilon_\infty + \frac{\Delta\varepsilon}{(1+(i\omega\tau)^m)^n} \qquad 0 < m \leq 1 \text{ and } 0 < mn \leq 1, \tag{3.51}$$

is a combination of the Cole-Cole and Cole-Davidson and is the most commonly used fitting model in the frequency domain. Here, m and n are shape parameters describing the symmetric and asymmetric broadening, respectively, which is shown in Figure 3.11. Typically, β-relaxations give rise to symmetrical relaxation peaks, well described by the Cole-Cole function, while α-relaxations is asymmetrically broadened and is often described by the Cole-Davidson equation or the more general HN function.

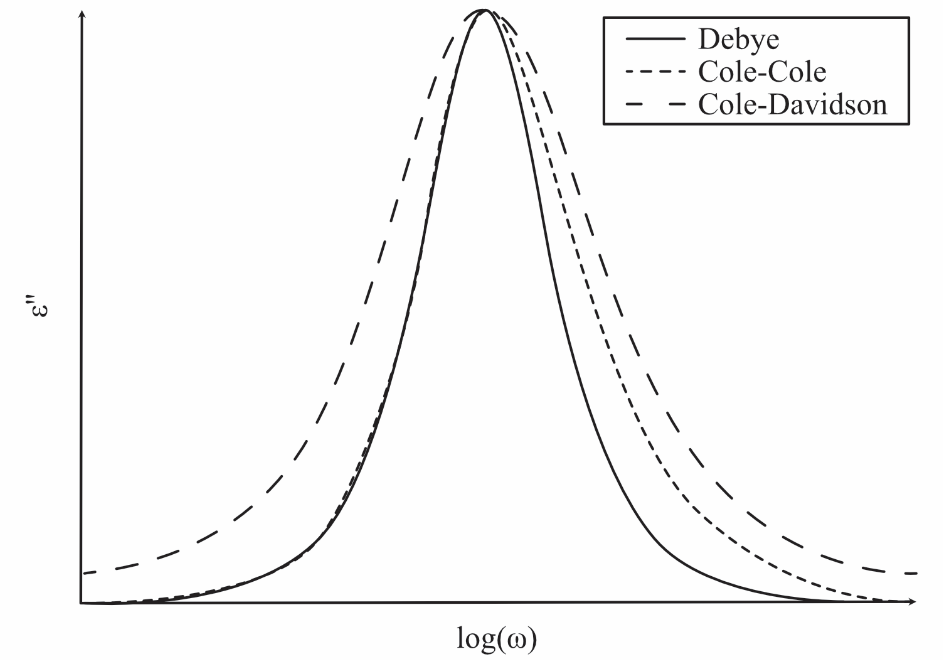

Figure 3.11: Representation of the fit functions used to describe the dielectric relaxations in the frequency domain, where the solid line represents the Debye function, the short dashed line the Cole-Cole function and the dashed line the Cole-Davidson function.

In paper V, the DS measurements were performed on a Novocontrol Alpha frequency analyser over the frequency range 0.02–10^7 Hz and at temperatures between 133–288 K in steps of 5 K. Hydrated protein monomers and fibrils were pressed between two 20 mm electrodes separated by a 100 µm Teflon spacer, forming the dielectric capacitor. The temperature was stabilised to within 0.01 K, and each measurement was preceded by an equilibration time of 600 s.

3.4.1 Analysis of the DS Data

The complex permittivity was fitted using a sum of HN functions

$$\varepsilon^*(\omega,T) = \varepsilon_\infty(T) + \frac{\Delta\varepsilon(T)}{[1+(i\omega\tau(T))^m]^n} + \frac{\sigma_0(T)}{i\varepsilon_f\omega}. \tag{3.52}$$

The final term accounts for the DC conductivity contributions. Assuming statistical independence of the relaxation processes, three (or four) partly overlapping HN functions were used to describe the measured spectra across the full frequency and temperature range. The relaxation time at maximum loss, $\tau_{\max}$, is obtained analytically from the HN parameters as

$$\tau_{\max} = \tau \sin^{-1/m}\left(\frac{\pi m}{2(1+n)}\right) \sin^{1/m}\left(\frac{\pi mn}{2(1+n)}\right). \tag{3.53}$$

For the hydrated proteins, the strong conductivity contribution dominates the imaginary part at low frequencies and obscure the underlying relaxation peaks. To suppress this contribution, the dielectric spectra were instead analysed using the conductivity-free derivative representation: $\varepsilon'(d\varepsilon'/dln\omega = -(2/\pi)\varepsilon''$.

3.5 Atomic Force Microscopy (AFM)

Atomic force microscopy (AFM) is one of the most commonly used scanning probe microscopy techniques, offering nanometre resolution for examining sample topography.[205] The main principle of AFM involves a resonating cantilever with a sharp tip which raster scans a selected area. It measures surface contact forces between the sample and the probe, generating an image of the sample's topography. This specific mode is referred to as tapping mode and is what is used in papers III and V. Besides tapping mode, there are two other standard imaging modes: contact mode and non-contact mode. In contact mode, the tip remains in constant contact with the sample and is "dragged" across the surface, generating an image from the feedback signal required to keep the cantilever at a constant height. In contrast, non-contact mode involves positioning the tip in close proximity to the surface, typically within a few Ångströms, without direct contact. The topography image in this mode is derived from the force interactions during the scanning process.

AFM was used to image the amyloid fibrils in papers III and V. The samples were diluted and pipetted onto mica plates which were rinsed 10 times with 200 µL MQ water following incubation for 10 min at room temperature. The surface was then carefully dried using filter paper and nitrogen. The AFM images were recorded on an NT-MDT NTEGRA Prima atomic force microscope with a NSG01 gold-coated single crystal silicon probe (Resonant frequency $\sim$ 150 kHz, force constant $\sim$ 5.1 N/m) using tapping mode (0.5 Hz scan frequency). The images were processed using the software Gwyddion.[206]

4

Sample Preparations

In the following chapter the different sample preparations used in the different papers will be explained.

4.1 Papers I and II

To gain new insights regarding the stabilising and anti-aggregating properties of trehalose, paper I compares a system consisting of 25 wt% myoglobin, 25 wt% trehalose, and 50 wt% water with one in which trehalose was replaced with sucrose, in paper I. The samples were prepared by dissolving the protein in sugar solutions. In paper II, similar but more diluted systems containing trehalose were prepared. The weight ratio of the systems was 10 wt% myoglobin, 20 wt% trehalose, and 70 wt% water. As a reference, a two-component system consisting of 33 wt% myoglobin and 67 wt% water was prepared in paper I.

The scattering length depends on the isotope. If the molecular structure of the system is unaffected by isotope substitution, then the changes in the structure factor are exclusively due to differences in the scattering lengths. This characteristic is advantageous for creating contrast in neutron scattering experiments. In papers I and II, neutron diffraction was used to analyse the role of the disaccharides in stabilising the native state of myoglobin and the following six isotopically different samples were prepared:

1. Myoglobin:D-sugar:D_2O
2. Myoglobin:D-sugar:H_2O
3. Myoglobin:H-sugar:D_2O
4. Myoglobin:H-sugar:H_2O
5. Myoglobin:HD-sugar:D_2O
6. Myoglobin:HD-sugar:HDO

The protonated and deuterated sugars are denoted H-sugar and D-sugar, respectively, where the isotope substitution in the sugar only applies to their carbon-bound hydrogens. The sugar in samples 1 and 3 were repeatedly dissolved in D_2O and dried under vacuum at 70 °C to exchange the hydroxyl hydrogens for deuterium. Myoglobin was freeze dried in H_2O (for samples 2 and 4) or D_2O (for samples 1 and 3) before use, to remove residual water molecules, and to deuterate the exchangeable hydrogens of the protein. Samples 5 and 6 were created from a 50/50 mol% mixture of samples 1 and 3 and samples 1 and 4, respectively.

In addition to the structural analysis of the samples, the dynamics of the systems were investigated by the use of QENS. Here, three isotopically different samples with sugar as well as two reference systems without sugar were prepared:

1. Myoglobin:D-sugar:H_2O
2. Myoglobin:H-sugar:D_2O
3. Myoglobin:H-sugar:H_2O
4. Myoglobin:D_2O
5. Myoglobin:H_2O
6. H-sugar:D_2O
7. D-sugar:H_2O

4.2 Paper IV

The stabilising effect of trehalose and sucrose at different temperatures and sample compositions were investigated in paper IV. Samples were prepared containing varying proportions of water, protein (either myoglobin or HEWL), and trehalose or sucrose. Synergistic effects were also investigated by combining of trehalose and sucrose to some samples.

Two preparation sequences were used. In sequence one, trehalose or sucrose was dissolved in MQ water under stirring and heating, after which the protein was added at room temperature and dissolved under gentle stirring. Samples with a target water concentration below 35 wt% were then concentrated by vacuum evaporation.

In sequence two, owing to the limited solubility of both sugar and protein, stock solutions of 50 wt% water and 50 wt% sugar were first prepared. Protein was subsequently added at room temperature and dissolved under gentle stirring, and the final water content was reached by vacuum evaporation or by blow-drying at approximately 40 °C. Sequence one was used for myoglobin, whereas sequence two was performed for both myoglobin and HEWL.

The sugar-to-protein weight ratios included 0:1, 1:3, 1:1, 3:1, and 1:0, depending on solubility constrains. The compositions of all samples are presented in Figure 4.1.

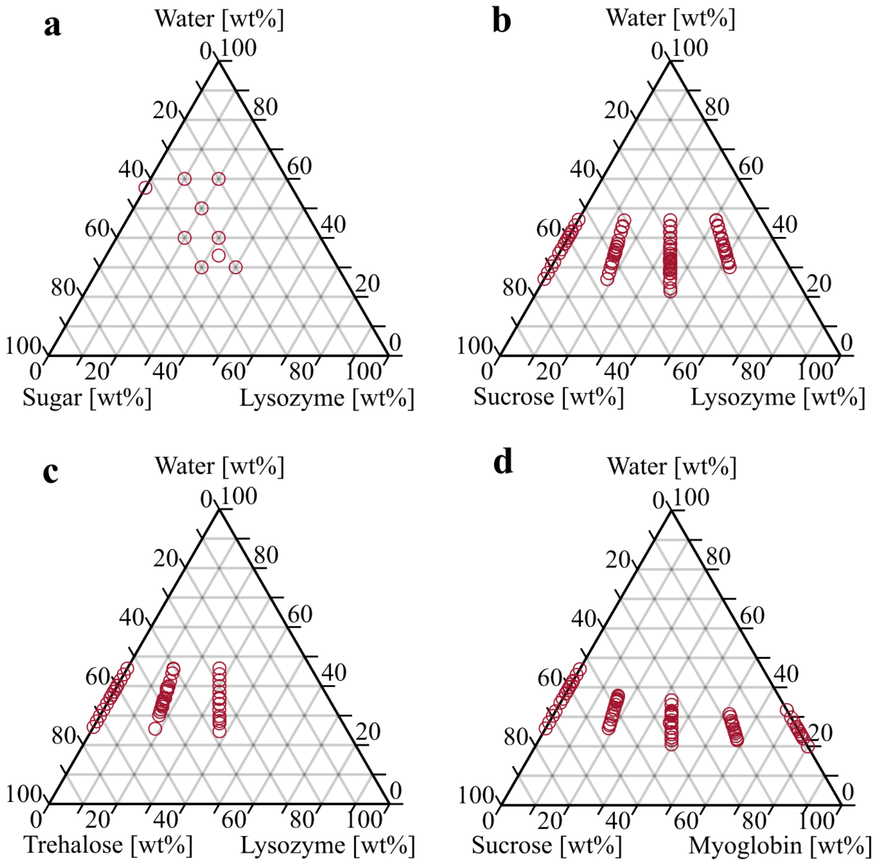

Figure 4.1: Ternary diagrams to illustrate the different compositions investigated. Reproduced from Ref. 53. Copyright © 2024 The Authors. Published by American Chemical Society.

4.3 Papers III and VI

In papers III and VI, the stabilising and anti-aggregating properties of trehalose and sucrose on HEWL were analysed. Each disaccharides was dissolved in MQ water under continuous stirring at ambient conditions. For the three-component systems (20 wt% HEWL, 27 wt% sugar, and 53 wt% MQ water), HEWL was added gradually to the sugar solutions and dissolved under gentle stirring. For the two-component systems (27 wt% HEWL and 73 wt% MQ water), HEWL was likewise dissolved gradually in MQ water under gentle stirring. The pH of the samples was recorded using both a Mettler Toledo Seven2go pH-meter and pH indicator sticks, and adjusted to 2.0 by adding small amounts of 2 M HCl. The samples were then incubated at different temperatures (T_{inc}). A table containing the different samples with their respective pH values and T_{inc} can be found in paper III.

In paper VI, the structure of the systems was investigated using neutron diffraction and the five following isotopically different samples were prepared for both native and fibrillar HEWL:

1. HEWL:D-sugar:D_2O
2. HEWL:D-sugar:H_2O
3. HEWL:H-sugar:D_2O
4. HEWL:H-sugar:H_2O
5. HEWL:HD-sugar:HDO

It should be noted that the exchangeable hydrogens were not exchanged, which does have an effect on the scattering contrast.

4.4 Paper V

HEWL (10 wt%) was dissolved in a 50 mM glycine-HCl buffer. The protein solution was filtered using a 0.1 µm filter to remove any preformed aggregates. The concentration of the solution was measured before and after filtration by UV-Vis spectroscopy. The pH was adjusted to pH 2.0 by addition of 2 M HCl and confirmed using both a Mettler Toledo Seven2go pH-meter and pH indicator sticks. The samples were incubated at 65 °C for 100 h. Upon fibrillation, HEWL forms a viscous gel, which was isolated by centrifugation at 14100g for 20 min, after which the supernatant was removed. To remove excess ions and HEWL monomers, the pellet was resuspended in excess of MQ water and centrifuged again under the same conditions. The supernatant was discarded, and the resulting gel pellet was dried under vacuum until a constant weight was reached.

In paper V, the dynamics of HEWL fibrils as well as native HEWL was investigated using NSE and DS. For these two techniques, different sample compositions were investigated. For the NSE measurements three different systems were prepared: a monomer sample (27 wt% HEWL in 73 wt% D_2O), a fibril sample (27 wt% HEWL in 73 wt% D_2O), and a diluted fibril sample obtained by tenfold dilution of the latter (2.7 wt% HEWL in 97.3 wt% D_2O). D_2O was used for the NSE samples due to the large incoherent scattering contribution of hydrogen atoms. The exchangeable hydrogens in HEWL were exchanged for deuterium by repeatedly dissolving the monomers or fibrils in D_2O followed by vacuum evaporation. This step was performed three times.

For the DS measurements, the dynamics in systems containing hydrated protein was investigated. HEWL fibrils and monomers were initially dried in vacuum at room temperature. The hydration level was then adjusted at atmospheric pressure by controlled exposure to elevated humidity in a desiccator.

5

Summary of Results

This thesis is based on six papers with the combined focus of protein stability and how structure and dynamics are affected by the presence of sugar and water. Papers I, II, and IV examine protein monomers in solution, with the aim of elucidating why trehalose is considered a superior protein stabiliser compared to other disaccharides such as sucrose. Papers III, V, and VI extend the study to amyloid fibrils in order to investigate the inhibitory effect of these disaccharides. The following sections summarise the results presented in the attached papers.

5.1 Paper I

Disaccharides are widely used as protein stabilisers, with trehalose generally considered the most effective. To elucidate the molecular mechanism behind this superior stabilising effect, paper I compared the structural and dynamical properties of aqueous trehalose and sucrose solutions containing the protein myoglobin.

The structural properties were studied using neutron and X-ray diffraction in combination with EPSR modelling, from which partial pair correlation functions, $g(r)$s, were calculated and are displayed in Figure 5.1. The green and red solid lines represent the correlation between oxygen atoms on the surface of the protein and water oxygen in the trehalose and sucrose containing systems, respectively. The results show that myoglobin is preferentially hydrated by water rather than sugar in both systems, but that this effect is more pronounced for trehalose. The green and red dashed lines represent the correlation between oxygen atoms on the surface of the protein and any oxygen atom in trehalose or sucrose, respectively. Here it can be seen that this interaction is slightly more pronounced for sucrose compared to trehalose. However, it should be mentioned that this interaction is quite small in both cases.

The dynamical properties were investigated using both QENS and MD simulations. The experimentally obtained $I(Q,t)$s were fitted as described in Section 3.1.5.1 to obtain the average relaxation times. Plotting the inverse average relaxation times as a function of Q^2 showed that the data are well described by the Gaussian jump-length diffusion model, which was then used to extract the diffusion constants. Both the water and sugar dynamics were found to be faster in the sucrose-containing systems, in both the two- and three-component systems. This effect is particularly clear for water in the three-component system, where the diffusion constant is significantly higher with sucrose than with trehalose, indicating that trehalose slows the hydration water, and consequently the protein, more effectively. As expected, the water dynamics were considerably faster than the sugar dynamics in all systems. The difference between the diffusion constants of sucrose and trehalose in the three-component system was, however, small, suggesting that the sugar dynamics themselves are quite similar in the two systems.

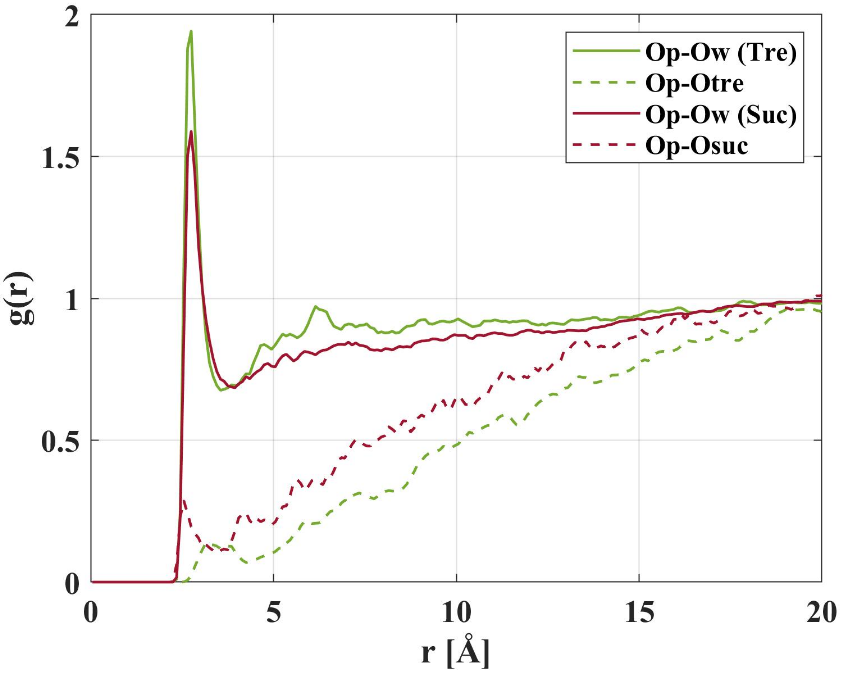

Figure 5.1: Partial pair correlation functions between the oxygens on the surface of the protein (Op) and water oxygens (Ow) or any oxygen atom in trehalose (Otre) or sucrose (Osuc). Reproduced from Ref. 51 with permission from the PCCP Owner Societies.

By the use of classical MD simulations, it was possible to investigate the rotational motion around the dihedrals between the two glucose rings of trehalose and the glucose and fructose rings of sucrose. The results showed that the rotational motion between the two glucose rings of trehalose was slower than the corresponding motion between the glucose and fructose rings of sucrose, suggesting that sucrose has a higher rotational mobility. As previously mentioned, trehalose was found to not interact directly with the protein. This result in combination with the slower rotational motion could be the reason for the superior stabilising effect compared to other disaccharides. To further investigate this hypothesis, rotational free energy calculations were performed. The results from these calculations show that the trehalose molecule has a similar mobility around both dihedrals, whereas for sucrose the mobility around the dihedral closer to the glucose ring was slower than that around the dihedral closer to the fructose ring. It could be concluded that the values of rotational potential of mean force for simulations with trehalose are higher, indicating that sucrose has a higher rotational mobility.

In addition, trehalose was observed to bind to fewer oxygen atoms of amino acids in the backbone of myoglobin than sucrose. The more direct binding of sucrose to the protein, combined with its faster rotational motions, suggests that sucrose facilitates protein dynamics more than trehalose and that sucrose and trehalose might be differently effective under different conditions. From these results, it can be concluded that trehalose possesses the ability to stabilise the native state of the protein without almost any direct contact with the surface of the protein.

5.2 Paper II

In paper I, trehalose was found to stabilise the native fold of myoglobin with minimal direct interaction with the surface of the protein. However, the relatively high concentration (25 wt% protein, 25 wt% sugar, and 50 wt% water) made it difficult to resolve how the trehalose molecules arrange themselves around the protein and in particular whether they form the "sugar-shell" that has previously been proposed to trap water close to the protein surface. Paper II addressed this limitation by employing more dilute samples (10 wt% protein, 20 wt% trehalose, and 70 wt% water), enabling a clearer investigation of the arrangement of trehalose relative to the hydration layer.

Neutron diffraction combined with Dissolve modelling was used to obtain structural information about the system. Partial pair correlation functions, $g(r)$s, were calculated with the same conditions as in paper I. Consistent with paper I, the protein was found to be preferentially hydrated by water rather than trehalose, and notably, no evidence of a "sugar-shell" surrounding the protein was observed.

In the initial model, molecules were randomly distributed in the simulation box. To rule out potential bias from the starting configuration, an alternative model was constructed with the protein centred in the box, trehalose molecules arranged on a tight sphere around it, and water molecules placed on an outer sphere. This model represents the opposite of the preferential hydration scenario. After refinement, the water molecules redistributed evenly throughout the box, whereas the trehalose molecules did not. A comparison of the $g(r)$s showed that, even starting from this configuration, the protein remained preferentially hydrated by water. The trehalose molecules stayed closer to the protein than in the randomly distributed system, but were nonetheless excluded from the immediate surface. Both the randomly distributed and the alternative model converged to the experimental data in the range 1–30 Å^{-1}, which is notable given the apparent differences between them. However, closer inspection of the low-Q region showed that the randomly distributed model reproduces the experimental data more accurately, providing further support for the preferential hydration model. This is illustrated in Figure 5.2, where (a) shows the alternative model before refinement, with trehalose positioned closer to the protein than water, and (b) shows the same system after refinement, with trehalose excluded from the surface and water now occupying the regions closest to the protein surface.

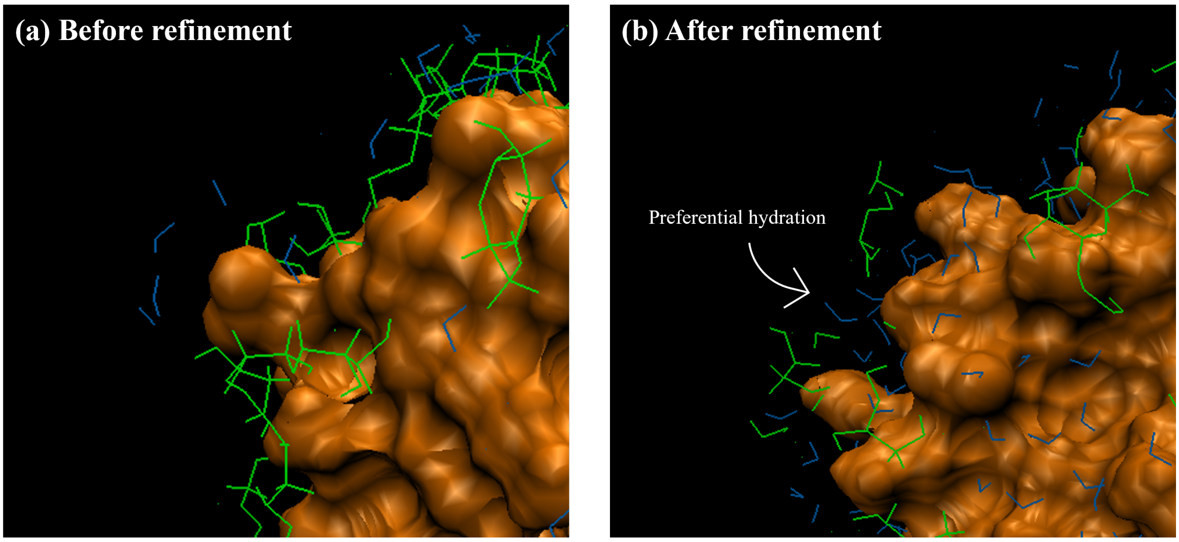

Figure 5.2: A magnified three-dimensional image of the alternative model (a) before and (b) after potential refinement. Only water and trehalose within 4 Å are visualised for visibility. The protein is illustrated in orange, and trehalose and water as green and blue stick figures, respectively. Reproduced from Ref. 52 with permission from the Royal Society of Chemistry.

The dynamical properties were investigated using QENS, and the results were compared with those of the corresponding trehalose-containing system in paper I. As expected, the dynamics were faster in the more dilute system, owing to the higher water content. The diffusion constant of water approached that of bulk water, consistent with a composition of 70 wt% water. The diffusion constants of trehalose and myoglobin also increased in the more dilute system. Furthermore, a comparison of the average relaxation times further showed that the internal protein dynamics, together with the water dynamics, are approximately four times faster in the dilute case, indicating a strong coupling between the internal protein motions and the water mobility. These results demonstrate that trehalose slows down the internal protein dynamics despite having very limited direct interaction with the protein surface.

5.3 Paper III

Trehalose has been shown to stabilise the native fold proteins as well as inhibit aggregation. The aim of paper III was therefore to investigate the mechanism behind these properties by comparing with sucrose. The protein HEWL is known to form amyloid fibrils at low pH and elevated temperatures. The inhibitory effect of both disaccharides was therefore evaluated at pH 2.0 and 3.5 following incubation at $T_{\text{inc}} = 57$ °C for 24 h.

The denaturation temperature of HEWL was recorded by the use of DSC. Both trehalose and sucrose were observed to increased the denaturation temperature of HEWL, confirming that both disaccharides stabilise the native state. Unexpectedly, sucrose had a slightly larger effect at both pH values, increasing the denaturation temperature by 12.6 °C at pH 2.0, compared to 9.5 °C for trehalose.

The intermolecular correlations were investigated by the use of SAXS. The results revealed two distinct peaks in the low-Q region for the two-component system at pH 2.0, indicating a bimodal size distribution not observed for the other systems. Figure 5.3(a) shows all systems incubated at $T_{\text{inc}} = 57$ °C. The peak in the lower Q-range ($Q = 0.0447$ Å^{-1}, $d = 141$ Å), suggests the formation of larger aggregates such as fibrils. In contrast, the Lys/H_2O system at pH 3.5 exhibited only a broad peak at $Q = 0.133$ Å^{-1} ($d =$ 55.6 Å), corresponding to monomer-to-monomer distances in solution. These results indicate a significant structural difference between the Lys/H_2O system at pH 2.0 compared to at pH 3.5. The sugar-containing systems showed less pronounced structural differences between pH values, indicating that the decrease in pH had a lesser effect in the presence of either disaccharide. The absence of the peak in the lower Q-region indicates that both trehalose and sucrose possess an inhibitory effect. To evaluate whether the inhibitory property was solely due to elevated denaturation temperatures, the incubation temperatures were increased closer to each system's denaturation midpoint (65 °C for trehalose, 68 °C for sucrose). Under these conditions, both sugar-containing systems at pH 2.0 showed an additional peak in the low-Q region, which can be seen in Figure 5.3(b). However, it is far less prominent than in the Lys/H_2O system at pH 2.0, suggesting that while the disaccharides increase the denaturation temperature, which contributes to protection, it is not the sole mechanism.

Although SAXS indicated larger aggregates in the Lys/H_2O system at pH 2.0, it could not confirm their fibrillar nature. WAXS was used to investigate possible correlations on a shorter length scale, and revealed a shoulder peak at a Q-value corresponding to approximately 4.55 Å in the Lys/H_2O system at pH 2.0. This is consistent with the characteristic interstrand distance of amyloid fibrils and was not observed for the sugar-containing systems incubated at $T_{\text{inc}} = 57$ °C, which further supports the inhibitory effect of both disaccharides.

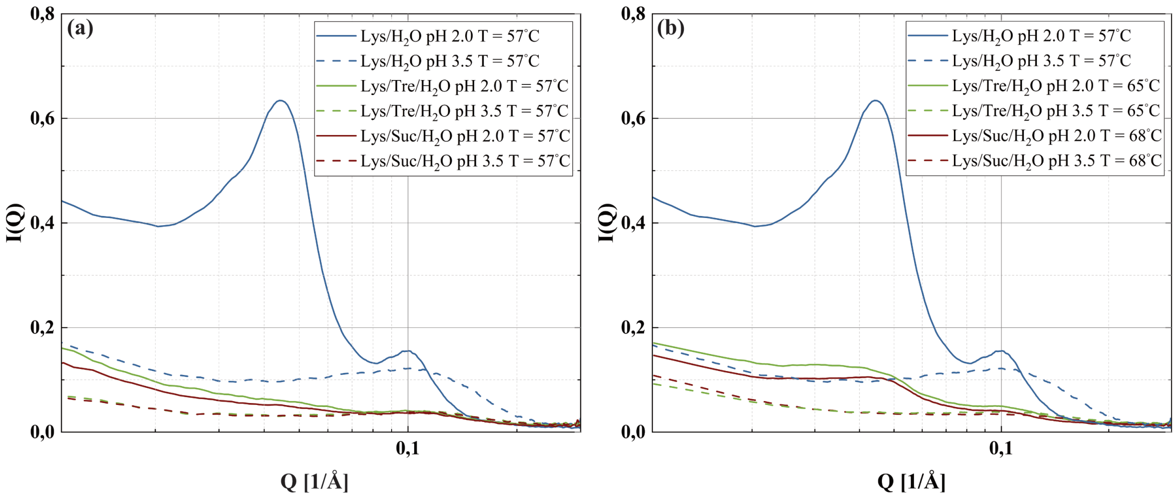

Figure 5.3: SAXS data of (a) Lys/H_2O, Lys/Tre/H_2O, and Lys/Suc/H_2O systems at pH 2.0 and pH 3.5 incubated at T_{inc} = 57 °C and (b) Lys/Tre/H_2O and Lys/Suc/H_2O systems at pH 2.0 and pH 3.5 incubated at T_{inc} = 65 °C and 68 °C, respectively. The Lys/H_2O system is the same data in both (a) and (b). Reproduced from Ref. 207 with permission from the Royal Society of Chemistry.

AFM was used to confirm that the aggregates observed by SAXS in the Lys/H_2O system at pH 2.0 are of amyloid type. The AFM images presented mature amyloid fibrils in the Lys/H_2O system at pH 2.0. Furthermore, fibrils were also found in the sugar-containing systems, although the SAXS data indicate that these are present at much lower concentrations.

5.4 Paper IV

The results from paper I indicated that trehalose is more effective compared to sucrose in decreasing the dynamics of the protein. However, the results from paper III showed that sucrose is slightly more effective in regards to increasing the T_{den}. The aim of paper IV was therefore to compare the stabilising effect of the two sugars at different conditions, such as temperature and concentration. In this paper, the stability of both myoglobin and HEWL was evaluated via the T_{g} and the T_{den}, at different sample compositions, by the use of DSC.

When a sample has a sufficiently low water content, crystallisation can be avoided. By adding sugar, the temperature at which crystallisation occurs can be lowered while the sample still contains a considerable amount of water. By investigating the maximal amount of water possible in a sample before it crystallises, the amount of amorphous hydration water present in the system can be deduced. In paper IV, these measurements were performed on systems containing sucrose to complement the study performed on similar systems containing trehalose presented in Ref. 33. The comparison of the results are presented in Figure 5.4. The results for the trehalose-containing systems show a linear relation between the maximum water content of the five different trehalose-to-protein ratios, indicating that the maximum amount amorphous water in the systems should be a weighted average of the binary systems. This suggests that basically no trehalose molecules replace the water at the protein surface. However, the results obtained for the sucrose containing systems show that the relation between the maximum water content of the five different sucrose-to-protein ratios is non-linear and that the water content at intermediate sucrose-to-protein ratios is considerably lower compared to the trehalose-containing samples. This suggests that the protein and sucrose molecules are not fully hydrated at these concentrations and that some sucrose molecules replace water at the protein surface. These results confirm that both systems are in agreement with the preferential hydration model and that it is more pronounced for trehalose, which is consistent with the results presented in paper I.

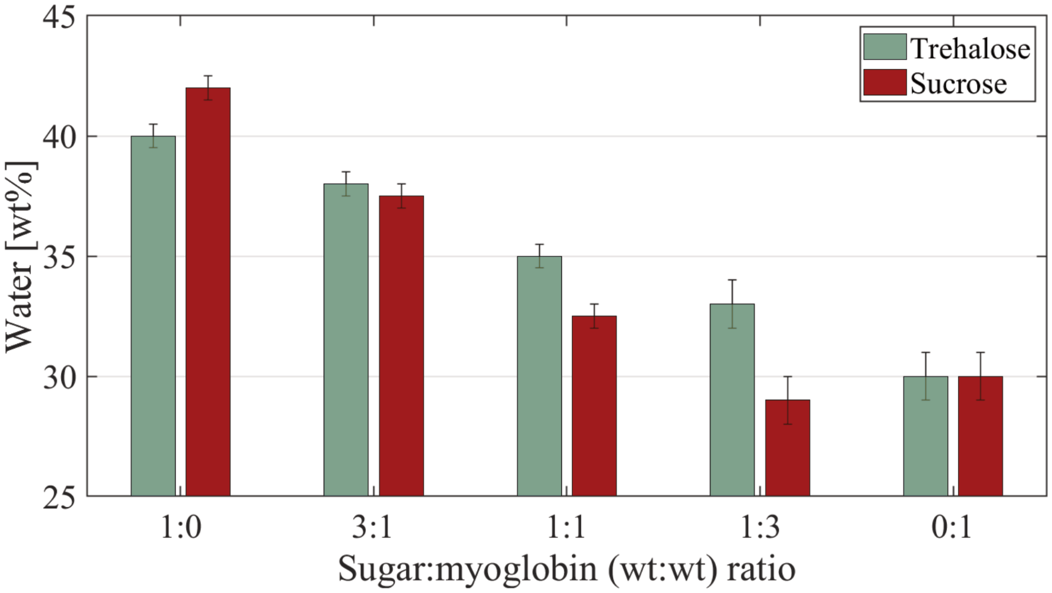

Figure 5.4: Maximum water content retained without crystallisation during cooling, shown for various sugar-to-protein weight ratios. The green bars indicate trehalose-containing systems and the red bars indicate sucrose-containing systems. Reproduced from Ref. 53. Copyright © 2024 The Authors. Published by American Chemical Society.

The T_g was observed to rapidly decrease with an increasing water content at low water concentrations for both the trehalose and sucrose containing systems. However, at higher water concentrations partial crystallisation occurs, resulting in a higher T_g of such samples. Increasing the water concentration further only results in an increase of the amount of ice in the system and not an increase of the amount hydration water.

Therefore, the T_g is observed to be relatively unaffected by such increments. Since the protein denaturation occurs at higher temperatures, the T_{den} is unaffected by crystallisation and is seen to decrease linearly with increasing water content across the entire concentration range. Consistent with the results obtained in paper III, both sucrose and trehalose increase the T_{den} of the protein, the former slightly more than the latter. As expected, a higher sugar-to-protein ratio results in a higher T_{den} in both cases.

Additionally, the occurrence of possible synergistic effects was explored through different combinations of the two sugars. It was seen that both the T_g and the T_{den} change linearly when one disaccharide is exchanged by the other, indicating that samples containing trehalose and sucrose behave as a linear combination of the samples containing sucrose or trehalose. This suggests that there are no synergistic effects when combining the two disaccharides.

5.5 Paper V

The general conception of amyloid fibrils is that they are relatively rigid protein structures. Paper V aims to examine the protein dynamics of amyloid fibrils formed by HEWL, compared with a reference system containing native HEWL, using NSE and DS. The morphology of the amyloid fibrils was examined by AFM.

The NSE measurements were performed on three HEWL:D_2O systems: one with fibrillated HEWL, one with native HEWL (both with a protein:D_2O ratio of 27wt%:73wt%) and one HEWL fibril system diluted 10 times relative to the original concentration. The $I(Q,t)$ curves for each Q-value were fitted by a stretched exponential, from which the average relaxation time was calculated and subsequently the Q^2 dependence was fitted using Fick's model of diffusion. The diffusion constant of the protein could then be extracted from the slope of the resulting curve for each system, from which the corresponding particle size was calculated. The diffusion constant of the fibrils in both the concentrated and the diluted system was lower than that of the HEWL monomers. The size obtained for the HEWL monomers is consistent with previously reported values, suggesting that the measured dynamics reflects diffusion of entire protein molecules. For the fibrils, however, the dynamically active segments were much smaller than the fibrils observed by AFM, indicating that the observed motion likely reflects the dynamics of shorter structural segments, such as the end regions of the fibrils, rather than diffusion of the entire fibril.

The $I(Q,t)$ curves of the fibril samples showed no clear plateau at any of the measured Q-values. Figure 5.5 shows the $I(Q,t)$ of the three different systems at a representable Q-value ($Q = 0.055$ Å^{-1}). For segmental motions confined in two dimensions, with no displacement along the long axis' of the fibril, a plateau is expected at sufficiently long times, with a value that depends on the displacement parameter, d. For the lowest

Q-values of the dilute fibril sample ($Q = 0.021$ Å^{-1}), a plateau value of 0.1 could not be ruled out at times beyond the experimentally accessible window. This implies that the polymer-like segmental motions must have an amplitude of at least 15 nm. The exact length of the moving segments cannot be directly extracted, since connected segments exhibit different dynamics from those of a freely diffusion rigid rod of equivalent length. However, given the relatively long persistence length of the fibrils, displacements of 15 nm or more would likely require extended portions of the fibril, on the order of 100 nm to participate in correlated motion.

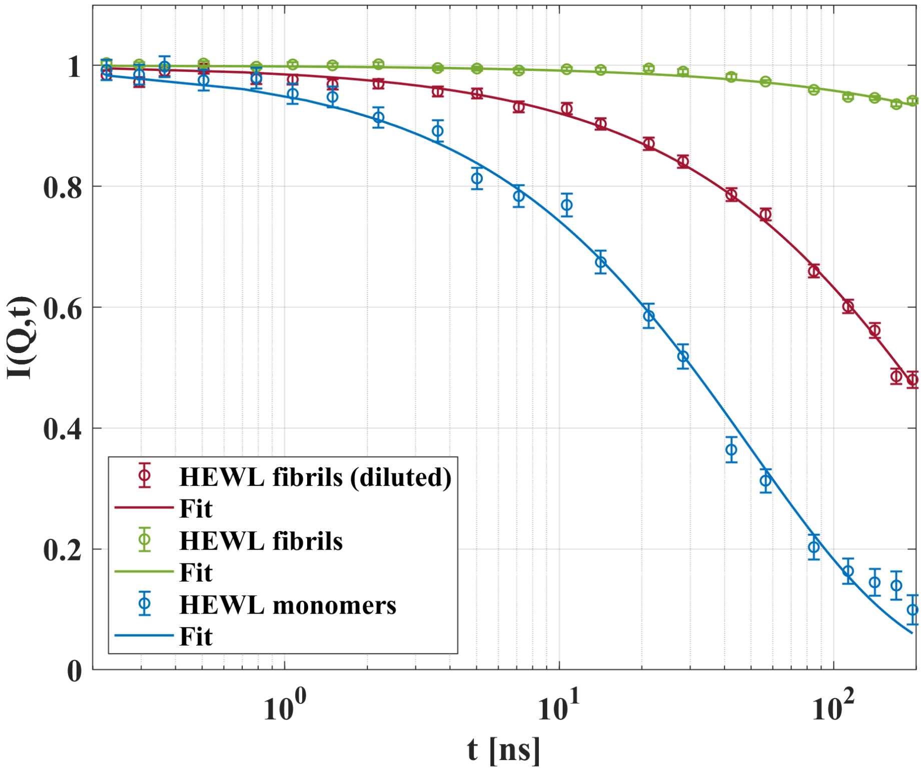

Figure 5.5: Intermediate scattering functions for HEWL monomers and fibrils at $Q = 0.055$ Å^{-1}, where the blue symbols represent the native HEWL and the green and red symbols represent the concentrated and the 10 times diluted fibril system, respectively. The solid lines are the fits by stretched exponentials. Obtained from paper V.

The DS measurements were performed on hydrated HEWL monomers and fibrils with a water content of 25wt% in order to avoid ice formation in the samples at lower temperatures. Three distinct dynamical processes were revealed, present in both the monomer and fibril systems, and are shown in Figure 5.6 together with the segmental motions revealed by NSE. The first, referred to as P1, has previously been attributed to the dynamics of hydration water and was observed for both the monomers and the fibrils. An additional process, referred to as the P2-process, was also observed in both systems and has previously been reported for hydrated lysozyme and attributed to the relaxation of protein side groups. Since the P2-process observed for the fibrils is very similar to that observed for the monomers, it is suggested that the side groups in HEWL fibrils undergo fluctuations similar to those in the monomers. Lastly, the P3-process is attributed to large scale conformational fluctuations of the protein. The temperature at which the structural relaxation intersects $\log_{10} = 2$ defines the glass transition temperature, which was observed for both the HEWL monomers and fibrils in this study. Since P3 is also observed for the HEWL fibrils, it is likely that the internal structural fluctuations of HEWL are not much affected by the transition from monomer to fibril. It has previously been shown that the internal dynamics of protein monomers are governed by those of the solvent, which is confirmed here for the monomers since the protein relaxations exhibit the same temperature dependence as the solvent relaxation. This was also, for the first time, observed for the fibrils, suggesting that the internal dynamics of the fibrils are governed by those of the hydration water.

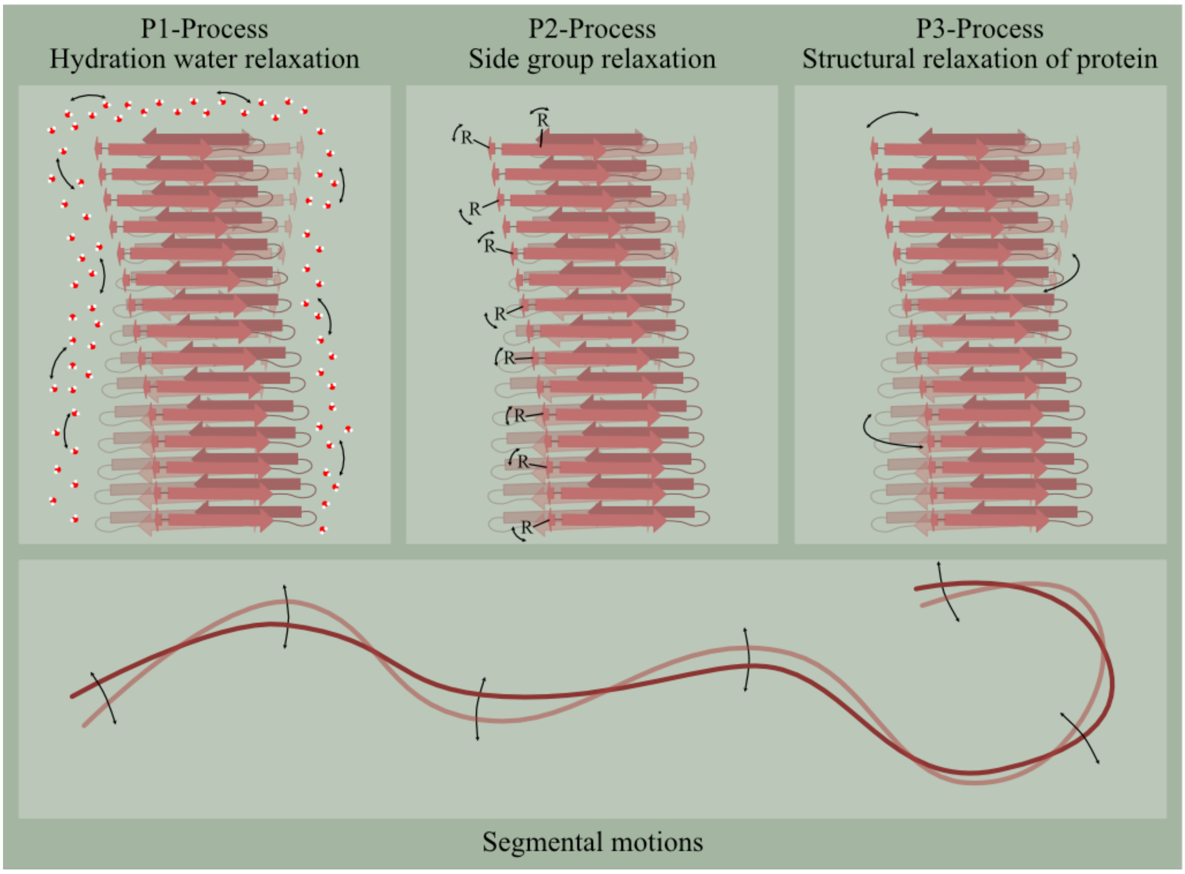

Figure 5.6: Schematic illustration of the dynamics observed for the HEWL amyloid fibrils. The top panel displays processes P1, P2, and P3, while the bottom panel illustrates the segmental motions. Obtained from paper V.

5.6 Paper VI

In paper VI, neutron diffraction was used to investigate the structure of systems containing HEWL with and without the two disaccharides trehalose and sucrose. Similarly as in paper III, the systems were analysed at two different pH values, 2.0 and 3.5.

Analysis of the low-Q region revealed a bimodal size distribution in the sugar-free system at pH 2.0, with one peak at $Q = 0.048$ Å^{-1}, corresponding to a real-space distance of $d = 131$ Å, and another at $Q = 0.104$ Å^{-1}, corresponding to $d = 60.4$ Å. The peak at lower Q reflects correlations between larger structures such as aggregates, whereas the peak at higher Q is due to correlations between smaller entities, such as the monomer-to-monomer separation. A comparison with the corresponding system at pH 3.5 revealed a significant structural difference between the two pH conditions. The system at pH 3.5 exhibited only a single peak at $Q = 0.107$ Å^{-1}, corresponding to $d = 58.7$ Å, which is consistent with the distance between HEWL monomers. Analysis of the systems containing trehalose or sucrose at pH 2.0, showed that some aggregation also occurs in the presence of sugar, but that the concentration of aggregates is considerably higher in the two-component system at pH 2.0. These results indicate that both disaccharides are capable of inhibiting the formation of amyloid fibrils. Comparing the sugar-containing systems at the two different pH vales, the structural difference between the samples is much smaller compared to the two-component systems.

Isotope substitution, in which the sugar was deuterated and the water protonated, enabled selective study of distinct components of the system. The results revealed a peak at $Q \approx 0.9$ Å^{-1}, corresponding to $d = 69.8$ Å in real-space. This peak most likely arises from concentration fluctuations in the spatial distribution of the sugar molecules. If the sugar molecules are largely excluded from the protein surface, they are forced into the relatively narrow regions between hydrated protein monomers and aggregates. As a result of this excluded volume effect, the sugar molecules become concentrated in regions without protein and with a relatively low amount of water. The observed peak is therefore likely to originate from correlations between such sugar-rich regions.

The diffraction data of the systems at pH 3.5 were combined with structural modelling using the Dissolve software. The partial pair correlation function between the oxygens on the surface of HEWL and the oxygens in either water or the sugars are shown in Figure 5.7. Here it can be seen that in the presence of either trehalose or sucrose, HEWL is hydrated by water molecules and the sugar molecules are excluded from the immediate surface. Similarly to the results presented in paper I, the effect is observed to be slightly more pronounced for the trehalose system. Comparing with the sugar-free system the amplitude of the fist peak is higher for the two sugar-containing systems, which is expected since there is more water molecules in the two-component system, thereby weighting the correlation between the protein and its hydration layer less.

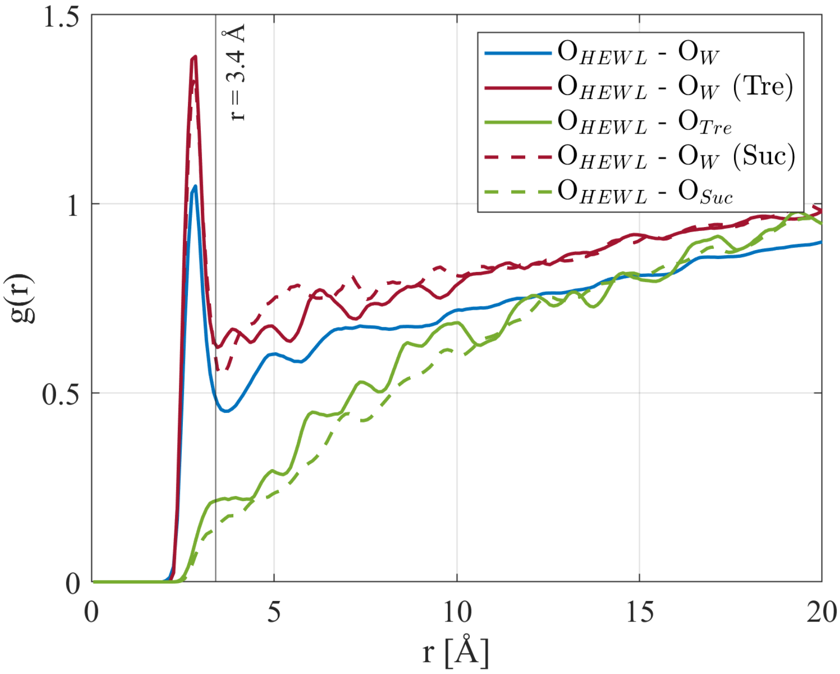

Figure 5.7: Partial pair correlation functions between oxygens on the surface of HEWL monomers (O_{HEWL}) and oxygens in either trehalose/sucrose ($O_{Tre/Suc}$) or water (O_W). The blue solid line shows the O_{HEWL}-O_W correlation in the HEWL:water system. The red solid and dashed lines show the O_{HEWL}-O_W correlation in the HEWL:Tre:water and HEWL:Suc:water systems, respectively. The green solid and dashed lines show the O_{HEWL}-$O_{Tre/Suc}$ correlation in the HEWL:Tre:water and HEWL:Suc:water systems, respectively. Surface oxygens are protein oxygens within 2.5 Å of any solvent atom.

6

Conclusion and Future Perspectives

The stability of proteins and how it is affected by the presence of trehalose and the structurally similar disaccharide sucrose have been investigated using different characterisation techniques to probe different time and length scales. Trehalose has long been considered an extraordinary stabiliser partly due to its high glass transition temperature. However, other glass formers with even higher glass transition temperatures do not possess the same stabilising properties as trehalose, indicating that the glass transition temperature alone cannot explain its effectiveness.

The preferential hydration model, which had previously been proposed, was confirmed throughout the work of this thesis. Additionally, it has been suggested that trehalose forms a sugar shell surrounding the protein, trapping water molecules close to the protein surface. However, this hypothesis was suggested for concentrated protein-sugar-water systems. In paper II, we demonstrated that trehalose does not form a sugar shell outside the water hydration layer in diluted systems. Instead, trehalose remains homogeneously distributed throughout the solution while the protein is preferentially hydrated by water.

Despite the lack of direct interaction with the protein surface, trehalose slows the dynamics of the protein in both concentrated and diluted systems. This effect is due to the dynamic coupling between the protein and trehalose. The disaccharides slow the hydration water, which in turn slows the protein dynamics, since the protein dynamics are governed by those of the surrounding solvent. When comparing trehalose with the structurally similar disaccharide sucrose, it was found that sucrose also exhibits preferential exclusion from the protein surface. Although sucrose interacts slightly more with the protein surface compared to trehalose. In paper I, it was revealed that the rotational motion around the dihedrals between the two glucose rings was slower compared to the corresponding motion of sucrose. Rotational free energy calculations confirmed that sucrose has higher rotational mobility, indicating greater flexibility. Combining this higher rotational mobility with the greater direct interaction with the protein backbone could lead to that sucrose facilitates protein dynamics more than trehalose.

The thermal stability of myoglobin and lysozyme was probed by measuring the denaturation temperature. Here, sucrose was observed to increase the denaturation temperature slightly more compared to trehalose, suggesting that sucrose is a more efficient stabiliser at higher temperatures. This enables the possibility that trehalose and sucrose might be differently efficient at different conditions, where different mechanisms are favoured.

When proteins aggregate into amyloid fibrils, they must first unfold, making the denaturation temperature relevant to fibril formation. The inhibitory effect of the two disaccharides on lysozyme fibril formation was investigated in paper III. To determine whether the inhibition was solely due to the increased denaturation temperature, the incubation temperature was raised proportionally to how much each sugar elevated the denaturation temperature. Although more amyloid fibrils formed upon increasing the incubation temperature, the concentration remained much lower than in the system without either trehalose or sucrose. This indicates that while stabilisation of the native fold clearly contributes to inhibition, it is not the sole mechanism.

In paper V we investigated the dynamics of proteins both as monomers and as amyloid fibrils. This study revealed that amyloid fibrils are more flexible and dynamic than previously been described. Importantly, the internal dynamics of the amyloid fibrils are governed by those of the hydration water, similarly to what has been shown for protein monomers. Combined with the results of the other papers included in this thesis, this finding suggests that regardless of the aggregation state, protein dynamics remain coupled to the surrounding hydration water.

The work presented in this thesis raised a central question: *how do disaccharides interact with proteins during the aggregation process, and can they modify the dynamics of the preformed fibrils?* Paper V was performed without disaccharides. A natural extension would be to investigate how trehalose affects the fibril dynamics and compare these effects with those of sucrose. This could include systems where the disaccharides are added before incubation, to study how protein dynamics are affected by the presence of an aggregation inhibitor, as well as systems where amyloid fibrils are preformed and the sugar is added afterwards. The former approach probes the inhibitory mechanism, while the latter could have relevance for therapeutic intervention after disease onset.

Additionally, future studies could examine the structure and dynamics of proteins during the aggregation process itself, capturing the transition from monomer to fibril. Temperature dependent QENS measurements tracking how the protein-sugar-water coupling evolves could clarify under what conditions each disaccharide is optimal, potentially resolving the apparent paradox that sucrose raises the denaturation temperature more effectively while trehalose is generally considered the superior stabiliser for long-term preservation.

Bibliography

[1] Ahlgren K. Sweet Stability - An Investigation of Disaccharides as Protein Stabilisers and Amyloid Fibril Inhibitors. Gothenburg: Chalmers University of Technology; 2024.

[2] Sipe JD, Cohen AS. Review: History of the Amyloid Fibril. J Struct Biol. 2000 6;130(2-3):88-98.

[3] World Health Organization. Dementia; 2025. Available from: `https://www.who.int/news-room/fact-sheets/detail/dementia`.

[4] Breijyeh Z, Karaman R. Comprehensive Review on Alzheimer's Disease: Causes and Treatment. Molecules. 2020 12;25(24):5789.

[5] Serpell LC. Alzheimer's amyloid fibrils: structure and assembly. Biochimica et Biophysica Acta (BBA) - Molecular Basis of Disease. 2000 7;1502(1):16-30.

[6] Hampel H, Hardy J, Blennow K, Chen C, Perry G, Kim SH, et al. The Amyloid-β Pathway in Alzheimer's Disease. Molecular Psychiatry. 2021 10;26(10):5481-503.

[7] Sunde M, Serpell LC, Bartlam M, Fraser PE, Pepys MB, Blake CC. Common core structure of amyloid fibrils by synchrotron X-ray diffraction. J Mol Biol. 1997 10;273(3):729-39.

[8] Sunde M, Blake CCF. From the globular to the fibrous state: protein structure and structural conversion in amyloid formation. Q Rev Biophys. 1998 2;31(1):1-39.

[9] Jarvis S, Mostaert A, editors. The functional fold: amyloid structures in nature. CRC Press; 2012.

[10] Iadanza MG, Jackson MP, Hewitt EW, Ranson NA, Radford SE. A new era for understanding amyloid structures and disease. Nat Rev Mol Cell Biol. 2018 12;19(12):755-73.

[11] Miller SR, Sekijima Y, Kelly JW. Native state stabilization by NSAIDs inhibits transthyretin amyloidogenesis from the most common familial disease variants. Laboratory Investigation. 2004 5;84(5):545-52.

[12] Soldi G, Plakoutsi G, Taddei N, Chiti F. Stabilization of a Native Protein Mediated by Ligand Binding Inhibits Amyloid Formation Independently of the Aggregation Pathway. Journal of Medicinal Chemistry. 2006 10;49(20):6057-64.

[13] Härd T, Lendel C. Inhibition of Amyloid Formation. J Mol Biol. 2012 8;421(4-5):441-65.

[14] Bakam Tchiakam S, Berger SL, Southall J, Walden H, Gabrielsen M. Stabilising proteins in solution using affordable and readily available small molecules. Biophysical Reviews. 2025 8;17(4):1093-104.

[15] De Virgilio C, Hottiger T, Dominguez J, Boller T, Wiemken A. The role of trehalose synthesis for the acquisition of thermotolerance in yeast. European Journal of Biochemistry. 1994 1;219(1-2):179-86.

[16] Sakurai M, Furuki T, Akao K, Tanaka D, Nakahara Y, Kikawada T, et al. Vitrification is essential for anhydrobiosis in an African chironomid, Polypedilum vanderplanki. Proceedings of the National Academy of Sciences. 2008 4;105(13):5093-8.

[17] Jain NK, Roy I. Effect of trehalose on protein structure. Protein Sci. 2009 1;18(1):24-36.

[18] Tapia H, Koshland D. Trehalose Is a Versatile and Long-Lived Chaperone for Desiccation Tolerance. Current Biology. 2014 12;24(23):2758-66.

[19] Møbjerg N, Halberg KA, Jørgensen A, Persson D, Bjørn M, Ramløv H, et al. Survival in extreme environments – on the current knowledge of adaptations in tardigrades. Acta Physiologica. 2011 7;202(3):409-20.

[20] Schill RO. 250 years of tardigrades: Goeze's discovery of a rare and peculiar creature. Organisms Diversity & Evolution. 2025 3;25(1):1-2.

[21] Guidetti R, Altiero T, Rebecchi L. On dormancy strategies in tardigrades. Journal of Insect Physiology. 2011 5;57(5):567-76.

[22] Ohtake S, Wang YJ. Trehalose: Current Use and Future Applications. Journal of Pharmaceutical Sciences. 2011 6;100(6):2020-53.

[23] Wang W. Instability, stabilization, and formulation of liquid protein pharmaceuticals. International Journal of Pharmaceutics. 1999 8;185(2):129-88.

[24] Chang T, Zhao G. Ice Inhibition for Cryopreservation: Materials, Strategies, and Challenges. Advanced Science. 2021 3;8(6):2002425.

[25] Fonte P, Soares S, Sousa F, Costa A, Seabra V, Reis S, et al. Stability Study Perspective of the Effect of Freeze-Drying Using Cryoprotectants on the Structure of Insulin Loaded into PLGA Nanoparticles. Biomacromolecules. 2014 10;15(10):3753-65.

[26] Connolly BD, Le L, Patapoff TW, Cromwell MEM, Moore JMR, Lam P. Protein Aggregation in Frozen Trehalose Formulations: Effects of Composition, Cooling Rate, and Storage Temperature. Journal of Pharmaceutical Sciences. 2015 12;104(12):4170-84.

[27] Brogna R, Oldenhof H, Sieme H, Figueiredo C, Kerrinnes T, Wolkers WF. Increasing storage stability of freeze-dried plasma using trehalose. PLOS ONE. 2020 6;15(6):e0234502.

[28] Tsegaye AA, Suptela AJ, Marriott I, Trammell SR. Light-assisted drying enables vaccine stabilization and supports cold-chain-independent distribution. Scientific Reports. 2026 2;16(1):11104.

[29] Arakawa T, Timasheff SN. Stabilization of protein structure by sugars. Biochem. 1982 12;21(25):6536-44.

[30] Crowe JH, Crowe LM, Chapman D. Preservation of Membranes in Anhydrobiotic Organisms: The Role of Trehalose. Science. 1984 2;223(4637):701-3.

[31] Green JL, Angell CA. Phase relations and vitrification in saccharide-water solutions and the trehalose anomaly. J Phys Chem. 1989 4;93(8):2880-2.

[32] Magazù S, Migliardo F, Telling MTF. α,α-TrehaloseWater Solutions. VIII. Study of the Diffusive Dynamics of Water by High-Resolution Quasi Elastic Neutron Scattering. The Journal of Physical Chemistry B. 2006 1;110(2):1020-5.

[33] Olsson C, Jansson H, Swenson J. The Role of Trehalose for the Stabilization of Proteins. J Phys Chem B. 2016 5;120(20):4723-31.

[34] Caccamo MT, Magazù S. Experimental Investigation on the Bioprotective Role of Trehalose on Glutamine Solutions by Infrared Spectroscopy. Materials. 2022 6;15(12):4329.

[35] Kaur A, Singh S, Sharma SC. Unlocking Trehalose's versatility: A comprehensive Journey from biosynthesis to therapeutic applications. Experimental Cell Research. 2024 10;442(2):114250.

[36] Ermilova I, Swenson J. Interactions of Sucrose and Trehalose with Lysozyme in Different Media: A Perspective from Atomistic Molecular Dynamics Simulations. Molecular Pharmaceutics. 2025 6;22(6):2997-3009.

[37] Crowe JH, Carpenter JF, Crowe LM. The role of vitrification in anhydrobiosis. Annu Rev Physiol. 1998 10;60(1):73-103.

[38] Liu Y, Bhandari B, Zhou W. Glass Transition and Enthalpy Relaxation of Amorphous Food Saccharides: A Review. Journal of Agricultural and Food Chemistry. 2006 8;54(16):5701-17.

[39] Olgenblum GI, Sapir L, Harries D. Properties of Aqueous Trehalose Mixtures: Glass Transition and Hydrogen Bonding. Journal of Chemical Theory and Computation. 2020 2;16(2):1249-62.

[40] Belton PS, Gil AM. IR and Raman spectroscopic studies of the interaction of trehalose with hen egg white lysozyme. Biopolymers. 1994 7;34(7):957-61.

[41] Cottone G, Ciccotti G, Cordone L. Protein–trehalose–water structures in trehalose coated carboxy-myoglobin. J Chem Phys. 2002 12;117(21):9862-6.

[42] Cottone G, Giuffrida S, Ciccotti G, Cordone L. Molecular dynamics simulation of sucrose- and trehalose-coated carboxy-myoglobin. Proteins: Structure, Function, and Bioinformatics. 2005 5;59(2):291-302.

[43] Cottone G. A Comparative Study of Carboxy Myoglobin in SaccharideWater Systems by Molecular Dynamics Simulation. J Phys Chem B. 2007 4;111(13):3563-9.

[44] Cordone L, Cottone G, Giuffrida S. Role of residual water hydrogen bonding in sugar/water/biomolecule systems: a possible explanation for trehalose peculiarity. Journal of Physics: Condensed Matter. 2007 5;19(20):205110.

[45] Corradini D, Strekalova EG, Stanley HE, Gallo P. Microscopic mechanism of protein cryopreservation in an aqueous solution with trehalose. Scientific Reports. 2013 2;3(1):1218.

[46] Arakawa T, Timasheff SN. The stabilization of proteins by osmolytes. Biophysical Journal. 1985 3;47(3):411-4.

[47] Lin T, Timasheff SN. On the role of surface tension in the stabilization of globular proteins. Protein Sci. 1996 2;5(2):372-81.

[48] Lins RD, Pereira CS, Hünenberger PH. Trehalose–protein interaction in aqueous solution. Proteins: Structure, Function, and Bioinformatics. 2004 4;55(1):177-86.

[49] Shimizu S, Smith DJ. Preferential hydration and the exclusion of cosolvents from protein surfaces. The Journal of Chemical Physics. 2004 7;121(2):1148-54.

[50] James S, McManus JJ. Thermal and Solution Stability of Lysozyme in the Presence of Sucrose, Glucose, and Trehalose. J Phys Chem B. 2012 8;116(34):10182-8.

[51] Ahlgren K, Olsson C, Ermilova I, Swenson J. New insights into the protein stabilizing effects of trehalose by comparing with sucrose. Phys Chem Chem Phys. 2023;25(32):21215-26.

[52] Ahlgren K, Olsson C, Youngs T, Swenson J. The nature of trehalose–protein interactions in aqueous solutions revealed by neutron scattering. Nanoscale. 2026;18:8609-21.

[53] Jonsson O, Lundell A, Rosell J, You S, Ahlgren K, Swenson J. Comparison of Sucrose and Trehalose for Protein Stabilization Using Differential Scanning Calorimetry. The Journal of Physical Chemistry B. 2024 5;128(20):4922-30.

[54] Elliott SR. Preparation. In: Physics of amorphous materials. 2nd ed. John Wiley & Sons; 1990. p. 1-27.

[55] Elliott SR. Glasses. In: Physics of amorphous materials. 2nd ed. John Wiley & Sons; 1990. p. 29-68.

[56] Soper AK. GudrunN and GudrunX: programs for correcting raw neutron and X-ray diffraction data to differential scattering cross section; 2011. Available from: `http://epubs.stfc.ac.uk`.

[57] Soper AK. The Structure of Water and Aqueous Systems. In: Exp. Methods Phys. Sci.. vol. 49. Academic Press; 2017. p. 135-211.

[58] Egelstaff PA. Thermal neutron scattering. London: Academic press; 1965.

[59] Lovesey SW. Theory of neutron scattering from condensed matter. Clarendon Press; 1986.

[60] Borsali R, Pecora R. Soft Matter Characterization. Springer, Dordrecht; 2008.

[61] Van Hove L. Correlations in Space and Time and Born Approximation Scattering in Systems of Interacting Particles. Physical Review. 1954 7;95(1):249-62.

[62] Micoulaut M. Correlation functions and linear response theory;. Available from: `https://www.lehigh.edu/imi/teched/AtModel/Lecture_6_Micoulaut_Atomistics_Glass_Course.pdf`.

[63] Soper AK, Phillips MG. A new determination of the structure of water at 25°C. Chemical Physics. 1986 8;107(1):47-60.

[64] Soper AK, Ricci MA. Structures of High-Density and Low-Density Water. Physical Review Letters. 2000 3;84(13):2881-4.

[65] Swenson J, Teixeira J. The glass transition and relaxation behavior of bulk water and a possible relation to confined water. The Journal of Chemical Physics. 2010 1;132(1).

[66] Nilsson A, Pettersson LGM. Perspective on the structure of liquid water. Chemical Physics. 2011 11;389(1-3):1-34.

[67] Soper AK. Water and ice structure in the range 220 - 365K from radiation total scattering experiments. 2014 11.

[68] Gallo P, Amann-Winkel K, Angell CA, Anisimov MA, Caupin F, Chakravarty C, et al. Water: A Tale of Two Liquids. Chemical Reviews. 2016 7;116(13):7463-500.

[69] Stenesh J. Frameworks of Biochemistry. In: Biochemistry; 1998. p. 3-23.

[70] Stanley HE. Unsolved Mysteries of Water in Its Liquid and Glass States. MRS Bulletin. 1999 5;24(5):22-30.

[71] Ben-Amotz D. Hydration-Shell Vibrational Spectroscopy. JACS. 2019 7;141(27):10569-80.

[72] Zhang Y, Lewis NHC, Mars J, Wan G, Weadock NJ, Takacs CJ, et al. Water-in-Salt LiTFSI Aqueous Electrolytes. 1. Liquid Structure from Combined Molecular Dynamics Simulation and Experimental Studies. J Phys Chem B. 2021 5;125(17):4501-13.

[73] Petkov V, Ren Y, Suchomel M. Molecular arrangement in water: random but not quite. Journal of Physics: Condensed Matter. 2012 4;24(15):155102.

[74] Narten AH, Danford MD, Levy HA. X-ray diffraction study of liquid water in the temperature range 4–200°C. Discuss Faraday Soc. 1967;43(0):97-107.

[75] Bergmann U, Di Cicco A, Wernet P, Principi E, Glatzel P, Nilsson A. Nearest-neighbor oxygen distances in liquid water and ice observed by x-ray Raman based extended x-ray absorption fine structure. J Chem Phys. 2007 11;127(17).

[76] Powar C, Chatwal G. Carbohydrates. In: Biochemistry. Global media; 2007. p. 117-55.

[77] Stenesh J. Carbohydrates. In: Biochemistry; 1998. p. 117-40.

[78] Hibshman JD, Clegg JS, Goldstein B. Mechanisms of Desiccation Tolerance: Themes and Variations in Brine Shrimp, Roundworms, and Tardigrades. Frontiers in Physiology. 2020 10;11.

[79] Hoekstra FA, Golovina EA, Buitink J. Mechanisms of plant desiccation tolerance. Trends Plant Sci. 2001 9;6(9):431-8.

[80] Viner RI, Clegg JS. Influence of trehalose on the molecular chaperone activity of p26, a small heat shock/α-crystallin protein. Cell Stress Chaperones. 2001;6(2):126.

[81] Buitink J, Hemminga MA, Hoekstra FA. Is There a Role for Oligosaccharides in Seed Longevity? An Assessment of Intracellular Glass Stability. Plant Physiol. 2000 4;122(4):1217-24.

[82] Stick RV, Williams SJ. Disaccharides, Oligosaccharides and Polysaccharides. In: Carbohydrates: The Essential Molecules of Life. Elsevier; 2009. p. 321-41.

[83] Thakral S, Sonje J, Munjal B, Suryanarayanan R. Stabilizers and their interaction with formulation components in frozen and freeze-dried protein formulations. Adv Drug Deliv Rev. 2021 6;173:1-19.

[84] Iturriaga G, Suárez R, Nova-Franco B. Trehalose Metabolism: From Osmoprotection to Signaling. Int J Mol Sci. 2009 9;10(9):3793-810.

[85] Chen A, Gibney PA. Dietary Trehalose as a Bioactive Nutrient. Nutrients. 2023 3;15(6):1393.

[86] Branca C, Magazù S, Maisano G, Migliardo P. Anomalous cryoprotective effectiveness of trehalose: Raman scattering evidences. J Chem Phys. 1999 7;111(1):281-7.

[87] Branca C, Magazù S, Migliardo F, Migliardo P. Destructuring effect of trehalose on the tetrahedral network of water: a Raman and neutron diffraction comparison. Phys A: Stat Mech Appl. 2002 2;304(1-2):314-8.

[88] Branca C, Magazù V, Maisano G, Migliardo F, Soper AK. Study on Destructuring effect of trehalose on water by neutron diffraction. Appl Phys A. 2002 12;74(0):s450-1.

[89] Branca C, Maccarrone S, Magazù S, Maisano G, Bennington SM, Taylor J. Tetrahedral order in homologous disaccharide-water mixtures. J Chem Phys. 2005 5;122(17).

[90] Magazù S, Migliardo F, Telling MTF. Structural and dynamical properties of water in sugar mixtures. Food Chemistry. 2008 2;106(4):1460-6.

[91] Stenesh J. Proteins. In: Biochemistry; 1998. p. 47-82.

[92] Gomes CM, Faísca PFN. Protein Structure. In: Protein Folding: An Introduction; 2018. p. 1-10. Available from: `http://www.springer.com/series/11958`.

[93] Vanzi F, Vladimirov S, Knudsen CR, Goldman YE, Cooperman BS. Protein synthesis by single ribosomes. RNA. 2003 10;9(10):1174-9.

[94] Branden C, Tooze J. The building blocks. In: Introduction to protein structure. 2nd ed. New York, NY: Garland Publishing, Inc.; 1999. p. 3-12.

[95] Walsh G. Protein structure and engineering. In: Proteins: Biochemistry and Biotechnology. 2nd ed. John Wiley & Sons; 2014. p. 25-65.

[96] Branden C, Tooze J. Motifs of protein structure. In: Introduction to protein structure; 1999. p. 13-34.

[97] Nick Pace C, Scholtz JM, Grimsley GR. Forces stabilizing proteins. FEBS Letters. 2014 6;588(14):2177-84.

[98] Mathews CK, Van Holde KE, Ahern KG. Biochemistry. Benjamin Cummings; 2000.

[99] Kendrew JC, Bodo G, Dintzis HM, Parrish RG, Wyckoff H, Phillips DC. A Three-Dimensional Model of the Myoglobin Molecule Obtained by X-Ray Analysis. Nature. 1958 3;181(4610):662-6.

[100] Zaia J, Annan RS, Biemann K. The correct molecular weight of myoglobin, a common calibrant for mass spectrometry. Rapid Communications in Mass Spectrometry. 1992 1;6(1):32-6.

[101] Chu K, Vojtchovský J, McMahon BH, Sweet RM, Berendzen J, Schlichting I. Structure of a ligand-binding intermediate in wild-type carbonmonoxy myoglobin. Nature. 2000 2;403(6772):921-3.

[102] Diamond R. Real-space refinement of the structure of hen egg-white lysozyme. J Mol Biol. 1974 1;82(3):371-91.

[103] Tan S, Tatsumura Y. Alexander Fleming (1881–1955): Discoverer of penicillin. Singapore Medical Journal. 2015 7;56(07):366-7.

[104] Jafari M, Mehrnejad F. Molecular Insight into Human Lysozyme and Its Ability to Form Amyloid Fibrils in High Concentrations of Sodium Dodecyl Sulfate: A View from Molecular Dynamics Simulations. PLoS One. 2016 10;11(10):e0165213.

[105] Hankiewicz J, Swierczek E. Lysozyme in human body fluids. Clin Chim Acta. 1974 12;57(3):205-9.

[106] Woods CM, Hooper DN, Ooi EH, Tan LW, Carney AS. Human Lysozyme has Fungicidal Activity against Nasal Fungi. Am J Rhinol Allergy. 2011 7;25(4):236-40.

[107] Pleyer C, Flesche J, Saeed F. Lysozyme amyloidosis – a case report and review of the literature. Clin Nephrol Case Stud. 2015 12.

[108] Granel B, Valleix S, Serratrice J, Chérin P, Texeira A, Disdier P, et al. Lysozyme Amyloidosis. Medicine. 2006 1;85(1):66-73.

[109] Sipe JD, Benson MD, Buxbaum JN, Ikeda Si, Merlini G, Saraiva MJM, et al. Amyloid fibril proteins and amyloidosis: chemical identification and clinical classification International Society of Amyloidosis 2016 Nomenclature Guidelines. Amyloid. 2016 10;23(4):209-13.

[110] Mine S, Ueda T, Hashimoto Y, Imoto T. Analysis of the internal motion of free and ligand-bound human lysozyme by use of 15N NMR relaxation measurement: A comparison with those of hen lysozyme. Protein Science. 2000 1;9(9):1669-84.

[111] Tokunaga Y, Sakakibara Y, Kamada Y, Watanabe Ki, Sugimoto Y. Analysis of Core Region from Egg White Lysozyme Forming Amyloid Fibrils. International Journal of Biological Sciences. 2013;9(2):219-27.

[112] Ow SY, Dunstan DE. The effect of concentration, temperature and stirring on hen egg white lysozyme amyloid formation. Soft Matter. 2013;9(40):9692.

[113] Sasahara K, Yagi H, Naiki H, Goto Y. Heat-induced Conversion of β2-Microglobulin and Hen Egg-white Lysozyme into Amyloid Fibrils. Journal of Molecular Biology. 2007 9;372(4):981-91.

[114] Walsh G. Proteins and proteomics. In: Proteins: Biochemistry and Biotechnology. 2nd ed. John Wiley & Sons; 2014. p. 1-25.

[115] Hirai M, Hagiwara Y, Takeuchi K, Kimura R, Onai T, Kawai-Hirai R, et al. Thermal unfolding and refolding of protein under osmotic pressure clarified by wide-angle X-ray scattering. Thermochim Acta. 2012 3;532:15-21.

[116] Levinthal C. ARE THERE PATHWAYS FOR PROTEIN FOLDING ?; 1968. 1.

[117] Dill KA, Chan HS. From Levinthal to pathways to funnels. Nat Struct Mol Biol. 1997 1;4(1):10-9.

[118] Gomes CM, Faísca PFN. Protein Folding - Why is Structure Acquired? In: Protein Folding: An Introduction; 2018. p. 10-20.

[119] Bryngelson JD, Onuchic JN, Socci ND, Wolynes PG. Funnels, pathways, and the energy landscape of protein folding: A synthesis. Proteins: Structure, Function, and Bioinformatics. 1995 3;21(3):167-95.

[120] Braselmann E, Chaney JL, Clark PL. Folding the proteome. Trends in Biochemical Sciences. 2013 7;38(7):337-44.

[121] Ciarán Ó'Fágáin. Engineering Protein Stability. In: Walls D, Loughran ST, editors. Protein Chromatography: Methods and Protocols. Totowa, NJ: Humana Press; 2011. p. 103-36.

[122] Fersht A. Structure and mechanism in protein science : a guide to enzyme catalysis and protein folding. vol. 9. New Jersey: World Scientific; 2017.

[123] Koo EH, Lansbury PT, Kelly JW. Amyloid diseases: Abnormal protein aggregation in neurodegeneration. PNAS. 1999 8;96(18):9989-90.

[124] Alzheimer's Disease and Related Dementias;. Available from: `https://cdc.gov/aging/aginginfo/alzheimers.htm`.

[125] Who has Parkinson's?;. Available from: `https://www.parkinson.org/understanding-parkinsons/statistics`.

[126] Kuroda Y. Biophysical studies of amorphous protein aggregation and in vivo immunogenicity. Biophys Rev. 2022 12;14(6):1495-501.

[127] Gazit E. The “Correctly Folded” State of Proteins: Is It a Metastable State? Angew Chem Int Ed. 2002 1;41(2):257.

[128] Meersman F, Dobson CM. Probing the pressure–temperature stability of amyloid fibrils provides new insights into their molecular properties. Biochim Biophys Acta, Proteins Proteomics. 2006 3;1764(3):452-60.

[129] Friedreich N, Kekulé A. Zur Amyloidfrage. Archiv für Pathologische Anatomie und Physiologie und für Klinische Medicin. 1859 1;16(1-2):50-65.

[130] Geddes AJ, Parker KD, Atkins EDT, Beighton E. “Cross-β” conformation in proteins. J Mol Biol. 1968 3;32(2):343-58.

[131] Eanes ED, Glenner GG. X-ray diffraction studies on amyloid filaments. J Histochem Cytochem. 1968 11;16(11):673-7.

[132] Linse S. Mechanism of amyloid protein aggregation and the role of inhibitors. Pure Appl Chem. 2019 2;91(2):211-29.

[133] Henzler-Wildman K, Kern D. Dynamic personalities of proteins. Nature. 2007 12;450(7172):964-72.

[134] Frauenfelder H, Sligar SG, Wolynes PG. The Energy Landscapes and Motions of Proteins. Science. 1991 12;254(5038):1598-603.

[135] McCammon JA. Protein dynamics. Reports on Progress in Physics. 1984 1;47(1):1-46.

[136] Garcia Sakai V, Alba-Simionesco C, Chen SH. Dynamics of soft matter : Neutron applications. Springer; 2012.

[137] Giepmans BNG, Adams SR, Ellisman MH, Tsien RY. The Fluorescent Toolbox for Assessing Protein Location and Function. Science. 2006 4;312(5771):217-24.

[138] Khodadadi S, Pawlus S, Sokolov AP. Influence of Hydration on Protein Dynamics: Combining Dielectric and Neutron Scattering Spectroscopy Data. The Journal of Physical Chemistry B. 2008 11;112(45):14273-80.

[139] Jansson H, Kargl F, Fernandez-Alonso F, Swenson J. Dynamics of a protein and its surrounding environment: A quasielastic neutron scattering study of myoglobin in water and glycerol mixtures. J Chem Phys. 2009 5;130(20).

[140] Olsson C, Genheden S, García Sakai V, Swenson J. Mechanism of Trehalose-Induced Protein Stabilization from Neutron Scattering and Modeling. J Phys Chem B. 2019 5;123(17):3679-87.

[141] Jansson H, Bergman R, Swenson J. Relation between Solvent and Protein Dynamics as Studied by Dielectric Spectroscopy. The Journal of Physical Chemistry B. 2005 12;109(50):24134-41.

[142] Swenson J, Jansson H, Bergman R. Relaxation Processes in Supercooled Confined Water and Implications for Protein Dynamics. Physical Review Letters. 2006 6;96(24):247802.

[143] Panagopoulou A, Kyritsis A, Aravantinou AM, Nanopoulos D, i Serra RS, Gómez Ribelles JL, et al. Glass Transition and Dynamics in Lysozyme–Water Mixtures Over Wide Ranges of Composition. Food Biophysics. 2011 6;6(2):199-209.

[144] Jansson H, Bergman R, Swenson J. Role of Solvent for the Dynamics and the Glass Transition of Proteins. The Journal of Physical Chemistry B. 2011 4;115(14):4099-109.

[145] Smith JC. Protein dynamics: comparison of simulations with inelastic neutron scattering experiments. Quarterly Reviews of Biophysics. 1991 8;24(3):227-91.

[146] Zorrilla S, Hink MA, Visser AJWG, Lillo MP. Translational and rotational motions of proteins in a protein crowded environment. Biophysical Chemistry. 2007 2;125(2-3):298-305.

[147] Kumar S, Ma B, Tsai CJ, Wolfson H, Nussinov R. Folding funnels and conformational transitions via hinge-bending motions. Cell Biochemistry and Biophysics. 1999 6;31(2):141-64.

[148] Grimaldo M, Roosen-Runge F, Zhang F, Schreiber F, Seydel T. Dynamics of proteins in solution. Quarterly Reviews of Biophysics. 2019 6;52:e7.

[149] Khodadadi S, Sokolov AP. Protein dynamics: from rattling in a cage to structural relaxation. Soft Matter. 2015;11(25):4984-98.

[150] Richter D, Monkenbusch M, Arbe A, Colmenero J. Neutron Spin Echo in Polymer Systems. Berlin, Heidelberg: Springer Berlin Heidelberg; 2005.

[151] Frauenfelder H, Gratton E. Protein dynamics and hydration. In: Methods in enzymology. vol. 127. Academic Press, Inc.; 1986. p. 207-16.

[152] Nakasako M. Hydration structures of proteins : atomic details. Springer; 2021.

[153] Frauenfelder H, Chen G, Berendzen J, Fenimore PW, Jansson H, McMahon BH, et al. A unified model of protein dynamics. Proc Natl Acad Sci U S A. 2009 3;106(13):5129-34.

[154] Fenimore PW, Frauenfelder H, McMahon BH, Parak FG. Slaving: Solvent fluctuations dominate protein dynamics and functions. Proceedings of the National Academy of Sciences. 2002 12;99(25):16047-51.

[155] Fenimore PW, Frauenfelder H, McMahon BH, Young RD. Bulk-solvent and hydration-shell fluctuations, similar to α- and β-fluctuations in glasses, control protein motions and functions. Proc Natl Acad Sci USA. 2004 10;101(40):14408-13.

[156] Frauenfelder H, Fenimore PW, Chen G, McMahon BH. Protein folding is slaved to solvent motions. Proceedings of the National Academy of Sciences. 2006 10;103(42):15469-72.

[157] Swenson J, Jansson H, Hedström J, Bergman R. Properties of hydration water and its role in protein dynamics. Journal of Physics: Condensed Matter. 2007 5;19(20):205109.

[158] Karplus M, Vitkup D, Ringe D, Petsko GA. Solvent mobility and the protein 'glass' transition. Nature Structural Biology. 2000 1;7(1):34-8.

[159] Olsson C, Zangana R, Swenson J. Stabilization of proteins embedded in sugars and water as studied by dielectric spectroscopy. Phys Chem Chem Phys. 2020;22(37):21197-207.

[160] Deng J, Davies DR, Wisedchaisri G, Wu M, Hol WGJ, Mehlin C. An improved protocol for rapid freezing of protein samples for long-term storage. Acta Crystallographica Section D Biological Crystallography. 2004 1;60(1):203-4.

[161] Miyamoto Y, Ikeuchi M, Noguchi H, Hayashi S. Long-term Cryopreservation of Human and other Mammalian Cells at 80 °C for 8 Years. Cell Medicine. 2018 1;10.

[162] Day JG, Stacey G. Cryopreservation and freeze-drying protocols. Humana Press; 2007.

[163] Castellanos MM, McAuley A, Curtis JE. Investigating Structure and Dynamics of Proteins in Amorphous Phases Using Neutron Scattering. Computational and Structural Biotechnology Journal. 2017;15:117-30.

[164] Sears VF. Neutron scattering lengths and cross sections. Neutron News. 1992 1;3(3):26-37.

[165] Ankner JF, Heller WT, Herwig KW, Meilleur F, Myles DAA. Neutron Scattering Techniques and Applications in Structural Biology. Current Protocols in Protein Science. 2013 4;72(1).

[166] McMaster WH, Del Grande NK, Mallett JH, Hubbell JH. COMPILATION OF X-RAY CROSS SECTIONS. SECTION III. California Univ., Livermore. Lawrence Radiation Lab.; 1968.

[167] Bauwens CM. X-Ray Scattering; 2011.

[168] Fisher Z, Jackson A, Kovalevsky A, Oksanen E, Wacklin H. Biological Structures. In: Exp. Methods Phys. Sci.. vol. 49. Academic Press; 2017. p. 1-75.

[169] D S Sivia. The basics of x-ray and neutron scattering. In: Elementary scattering theory: for x-ray and neutron users. Oxford University Press; 2011. p. 63-92.

[170] Fitter J, Gutberlet T, Katsaras J. Neutron Scattering for Biology. In: Neutron Scattering in Biology: Techniques and Applications; 2006. p. 1-17.

[171] Jülich F, Brückel T, Heger G, Richter D, Zorn R. Neutron Scattering: Lectures of the JCNS Laboratory Course Held at Forschungszentrum Jülich and the Research Reactor FRM II of TU Munich. Forschungszentrum Jülich; 2010.

[172] Bacon GE. Neutron diffraction. 3rd ed. Oxford university press; 1975.

[173] Bowron DT, Soper AK, Jones K, Ansell S, Birch S, Norris J, et al. NIMROD: The Near and InterMediate Range Order Diffractometer of the ISIS second target station. Review of Scientific Instruments. 2010 3;81(3).

[174] Disordered Materials XRD;. Available from: `https://www.isis.stfc.ac.uk/Pages/XRD.aspx`.

[175] Soper AK. Partial structure factors from disordered materials diffraction data: An approach using empirical potential structure refinement. Phys Rev B. 2005 9;72(10):104204.

[176] McGreevy RL, Pusztai L. Reverse Monte Carlo Simulation: A New Technique for the Determination of Disordered Structures. Molecular Simulation. 1988 12;1(6):359-67.

[177] Youngs T. Dissolve: next generation software for the interrogation of total scattering data by empirical potential generation. Mol Phys. 2019 11;117(22):3464-77.

[178] Soper AK. Empirical Potential Structure Refinement A User's Guide; 2017.

[179] Jmol: an open-source Java viewer for chemical structures in 3D.;. Available from: `http://www.jmol.org/`.

[180] Berendsen HJC, Grigera JR, Straatsma TP. The missing term in effective pair potentials. J Phys Chem. 1987 11;91(24):6269-71.

[181] Kony D, Damm W, Stoll S, Van Gunsteren WF. An improved OPLS-AA force field for carbohydrates. J Comput Chem. 2002 11;23(15):1416-29.

[182] Wu Y, Tepper HL, Voth GA. Flexible simple point-charge water model with improved liquid-state properties. The Journal of Chemical Physics. 2006 1;124(2).

[183] Humphrey W, Dalke A, Schulten K. VMD: visual molecular dynamics. J Mol Graph. 1996 2;14(1):33-8.

[184] Bée M. General Aspects of Neutron Scattering. In: Quasielastic Neutron Scattering. Bristol, England: Adam Hilger; 1988. p. 9-71.

[185] Carlile CJ, Adams MA. The design of the IRIS inelastic neutron spectrometer and improvements to its analysers. Phys B. 1992;182:431-40.

[186] Arnold O, Bilheux JC, Borreguero JM, Buts A, Campbell SI, Chapon L, et al. Mantid—Data analysis and visualization package for neutron scattering and μ SR experiments. Nucl Instrum Methods Phys Res A. 2014 11;764:156-66.

[187] Williams G, Watts DC. Non-symmetrical dielectric relaxation behaviour arising from a simple empirical decay function. Trans Faraday Soc. 1970;66:80.

[188] Bée M. Quasielastic Neutron Scattering for Continuous or Random Jump Diffusion of Molecules in Bounded Media. In: Quasielastic Neutron Scattering; 1988. p. 357-98.

[189] Mezei Ferenc, editor. Neutron Spin Echo. vol. 128. 1st ed. Berlin, Heidelberg: Springer Berlin Heidelberg; 1980.

[190] Mezei F, Pappas C, Gutberlet T. Neutron spin echo spectroscopy: basics, trends, and applications. Springer; 2003.

[191] Farago B. Recent neutron spin-echo developments at the ILL (IN11 and IN15). Physica B: Condensed Matter. 1999 6;267-268:270-6.

[192] Kikhney AG, Svergun DI. A practical guide to small angle X-ray scattering (SAXS) of flexible and intrinsically disordered proteins. FEBS Letters. 2015 9;589(19PartA):2570-7.

[193] Alder BJ, Wainwright TE. Phase Transition for a Hard Sphere System. J Chem Phys. 1957 11;27(5):1208-9.

[194] Wang J, Wolf RM, Caldwell JW, Kollman PA, Case DA. Development and testing of a general amber force field. J Comput Chem. 2004 7;25(9):1157-74.

[195] Lim JB, Rogaski B, Klauda JB. Update of the Cholesterol Force Field Parameters in CHARMM. J Phys Chem B. 2012 1;116(1):203-10.

[196] Huang J, MacKerell AD. CHARMM36 all-atom additive protein force field: Validation based on comparison to NMR data. J Comput Chem. 2013 9;34(25):2135-45.

[197] Lin FY, MacKerell AD. Improved Modeling of Halogenated Ligand–Protein Interactions Using the Drude Polarizable and CHARMM Additive Empirical Force Fields. J Chem Inf Model. 2019 1;59(1):215-28.

[198] Bitar M, Offman M. Molecular Dynamics;.

[199] Gill P, Moghadam TT, Ranjbar B. Differential scanning calorimetry techniques: applications in biology and nanoscience. J Biomol Tech. 2010 12;21(4):167-93.

[200] Kremer F, Schönhals A. Broadband dielectric spectroscopy. Springer Science & Business Media; 2002.

[201] Raicu V, Feldman Y. Dielectric relaxation in biological systems: physical principles, methods, and applications. Oxford University Press; 2015.

[202] Cole KS, Cole RH. Dispersion and Absorption in Dielectrics I. Alternating Current Characteristics. The Journal of Chemical Physics. 1941 4;9(4):341-51.

[203] Davidson DW, Cole RH. Dielectric Relaxation in Glycerol, Propylene Glycol, and n-Propanol. The Journal of Chemical Physics. 1951 12;19(12):1484-90.

[204] Havriliak S, Negami S. A complex plane representation of dielectric and mechanical relaxation processes in some polymers. Polymer. 1967 1;8:161-210.

[205] Haugstad G. Overview of AFM. In: Atomic Force Microscopy: Understanding Basic Modes and Advanced Applications. 1st ed. John Wiley & Sons; 2012. p. 1-33.

[206] Nečas D, Klapetek P. Gwyddion: An open-source software for SPM data analysis; 2012.

[207] Ahlgren K, Havemeister F, Andersson J, Esbjörner EK, Swenson J. The inhibition of fibril formation of lysozyme by sucrose and trehalose. RSC Advances. 2024;14(17):11921-31.